PHYSICAL REVIEW C **101**, 024001 (2020)

Editors' Suggestion

Covariant spectator theory of *np* scattering: Deuteron form factors

Franz Gross[*]
Thomas Jefferson National Accelerator Facility, Newport News, Virginia 23606, USA
and College of William and Mary, Williamsburg, Virginia 23185, USA

(Received 23 August 2019; revised manuscript received 18 October 2019; accepted 9 December 2019; published 3 February 2020)

The deuteron form factors are calculated using two model wave functions obtained from the 2007 covariant spectator theory high-precision fits to *np* scattering data. Included in the calculation is a new class of isoscalar *np* interaction currents which are automatically generated by the nuclear force model used in these fits. If the nuclear model WJC2 is used, a precision fit (χ^2/datum ≈ 1) to the Sick global analysis (GA) of all *ed* elastic scattering data can be obtained by adjusting the unknown off-shell nucleon form factors $F_3(Q^2)$ (discussed before) and $F_4(Q^2)$ (introduced in this paper) and predicting the high-Q^2 behavior of the neutron charge form factor $G_{En}(Q^2)$ well beyond the region where it has been measured directly. Relativistic corrections, isoscalar interaction currents, and off-shell effects are defined and discussed, and their sizes are displayed. A rationale for extending *ed* elastic scattering measurements to higher Q^2 is presented.

DOI: 10.1103/PhysRevC.101.024001

I. INTRODUCTION

A. Background

This work is the last in a series of papers [1–3] (referred to as Refs. I, II, and III; with errata to Ref. II given in Ref. [4]) that present the fourth-generation calculation of the deuteron form factors using the covariant spectator theory (CST) [5–7]. The third generation, done by Van Orden and collaborators in 1995 [8], calculated the form factors from a variation of model IIB (originally obtained from a 1991 fit to the *np* database [9], with an improved fit giving χ^2/datum $\simeq 2.5$ [8]) and provided an excellent description of the deuteron form factors. The current calculation is needed only because a better CST fit to the *np* database was found in 2007. This fit, with a χ^2/datum $\approx$1, included momentum-dependent terms in the kernel and requires a completely new treatment. For a brief review of the previous CST history of calculations of the form factors, see the introduction to Ref. [1]. For a more comprehensive survey of this field, see several recent reviews [10–12].

The CST, in common with other treatments based on the assumption that *NN* scattering can be explained by the ladders and crossed ladders arising from the exchange of mesons between nucleons [7,13], treats nucleons and mesons as the elementary degrees of freedom, with the internal structure of the nucleons and mesons treated phenomenologically. This means that, in particular, the electromagnetic form factors of the nucleons that are bound into a deuteron are not calculated but must be obtained from direct measurements of electron-nucleon scattering. If the form factors cannot be measured directly, they can be treated as undetermined functions that can be fixed by fitting the theory to electron-deuteron (*ed*) scattering data.

Like the 1991 fit that lead to model IIB, the new fit to the 2007 *np* data base [14,15] was obtained using the CST two-body equation (sometimes called the Gross equation) with a one-boson exchange (OBE) kernel. However, we found that a high-precision fit (with χ^2/datum $\sim$1) could be obtained only if the $NN\sigma_0$ vertices associated with the exchange of a scalar-isoscalar meson, denoted σ_0, included momentum-dependent terms in the form

$$\Lambda^{\sigma_0}(p,p') = g_{\sigma_0}\mathbf{1} - \nu_{\sigma_0}[\Theta(p)+\Theta(p')], \tag{1.1}$$

where ν_{σ_0} is a parameter fixed by fitting the *NN* scattering data, p and p' are the four-momenta of the outgoing and incoming nucleons, respectively, and the Θ are projection operators

$$\Theta(p) = \frac{m-\not{p}}{2m}, \tag{1.2}$$

which are nonzero for off-shell particles, and hence are a feature of both the Bethe-Salpeter and CST equations.

Two high-precision models were found with somewhat different properties. Model WJC1 (originally designated WJC-1), designed to give the best fit possible, has 27 parameters, χ^2/datum $\simeq 1.06$, and a large $\nu_{\sigma_0} = -15.2$. Model WJC2 (originally designated WJC-2), designed to give an excellent fit with as few parameters as possible, has only 15 parameters, χ^2/datum $\simeq 1.12$, and a smaller $\nu_{\sigma_0} = -2.6$. Both models also predict the correct triton binding energy (see Figs. 12 and 13 of Refs. [14] and [16]). The deuteron wave functions predicted by both of these models [15] have small *P*-state components of relativistic origin, and the normalization of the wave functions includes a term coming from the energy dependence of the kernel, which contributes −5.5% for WJC1 and −2.3% for WJC2.

This momentum dependence of the kernel implies the existence of a new class of *np* isoscalar interaction

---

[*] gross@jlab.org

currents that will contribute to the electromagnetic interaction of the deuteron, leading to the need for this fourth-generation calculation. These currents were fixed in Ref. I and used to predict the deuteron magnetic moment (Ref. II) and the quadrupole moment (Ref. III). This paper completes this series of papers by calculating the dependence of the form factors on the momentum transfer of the scattered electron, Q^2.

In the process of fitting the *ed* data, one is able to determine two off-shell nucleon form factors and predict the high-momentum behavior of the neutron electric form factor, $G_{En}(Q^2)$, beyond the region where it has been measured. These and other major conclusions of this paper are discussed in detail in Sec. VI below.

B. Organization of the paper

This paper is organized into six sections, with most of the theoretical details moved to the Appendixes. The rest of this section describes the ingredients of the calculation as simply as possible, with emphasis on the important off-shell nucleon current. A more complete discussion can be found in the Appendixes and in Refs. I–III. The major results are described in Sec. II, which gives predictions that are extracted from the *ed* measurements. Section III shows how the individual deuteron form factors are built up from the different theoretical contributions, and Sec. IV discusses the size and importance of relativistic effects. The results for the deuteron static moments are reviewed in Sec. V, and finally I draw major conclusions in Sec. VI. The reader eager to get to the conclusions may jump to Sec. VI and backtrack as needed to fill in the many missing details.

Seven Appendixes summarize many details needed for a precise understanding of this paper. Appendix A reviews the theoretical definitions of the deuteron form factors, deuteron current, and deuteron wave and vertex functions and examines how the arguments of the amplitudes are shifted by the relativistic boosts that enter into the calculation of the form factors. Appendix B derives the form of the nonrelativistic deuteron charge form factor, G_C, in momentum space. Appendixes C and D discuss some details of the extraction of the nucleon form factors from the theory, and Appendixes E and F describe some theoretical transformations that facilitate the calculations. Finally, Appendix G discusses some errors (Ref. [4]) that were found in Ref. II.

C. Diagrammatic form of the deuteron current

In CST, when a OBE kernel is used to describe the *NN* interaction, the two-body current is given initially by the four diagrams shown in Fig. 1. Here, by convention, it is assumed that particle 1 is on shell (I could have chosen particle 2 to be on shell with corresponding changes in the diagrams), and the necessary (anti)symmetry between the two particles is contained in the kernel, which is explicitly (anti)symmetrized. Note that, if the photon interacts with particle 1, energy and momentum conservation will not allow both the incoming and outgoing nucleons to be on shell at the same time, and this gives rise to two diagrams 1($\mathrm{B}_\pm$). (These are individually singular, but when both are included their singularities cancel.) In all of the diagrams, the deuteron structure is represented by a vertex function, Γ, in which particle 1 is on shell and particle 2 off shell, or a vertex function $\Gamma_{\rm BS}$ in which *both* particles are off shell. The vertex function Γ is calculated directly from the deuteron bound-state equation and $\Gamma_{\rm BS}$ can be calculated from Γ.

I showed in Ref. I how the interaction current operator shown in Fig. 1(C) can be re-expressed in terms of products of the nucleon current and two truncated kernels $\overline{V}^{(i)}_{+}$ (and their Dirac conjugates $\overline{V}^{(i)}_{-}$), defined to be the coefficients of the factors $\gamma_i \cdot P_\pm$ (where $i = \{1, 2\}$ and γ_i^μ operates in the

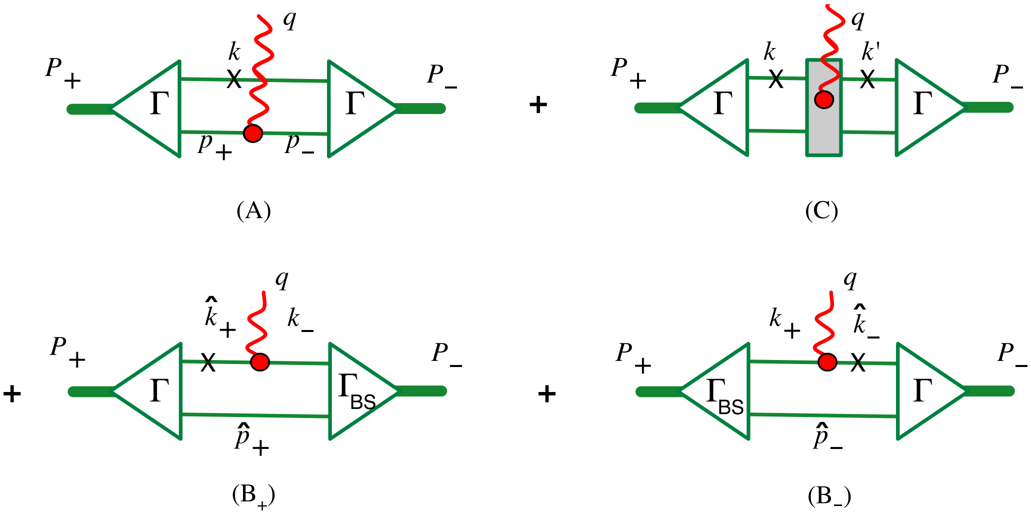

(A) (C)

(B_+) (B_-)

FIG. 1. Diagrammatic representation of the current operator of the covariant spectator theory with particle 1 on shell (the on-shell particle is labeled with a ×). Diagrams (A), (B_+), and (B_-) are the complete impulse approximation (CIA), while (C) is the interaction current term. Note that both particles are off-shell in the initial state in diagram (B_+) and in the final state in diagram (B_-). (In all diagrams, the Γ or $\Gamma_{\rm BS}$ in the *outgoing* state is to be read as the Dirac conjugate $\overline{\Gamma} = \gamma_0\Gamma^\dagger\gamma_0$ or $\overline{\Gamma}_{\rm BS} = \gamma_0\Gamma^\dagger_{\rm BS}\gamma_0$.)

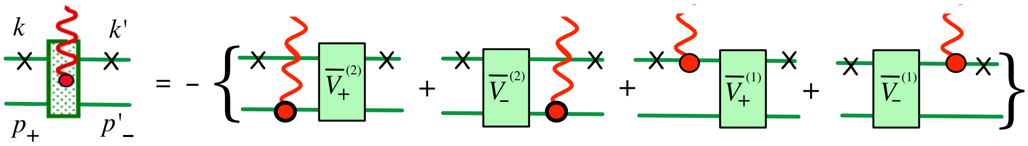

FIG. 2. Diagrammatic representation of the form of the interaction current derived in Ref. I and discussed in the text.

space of particle i) that appear in the full kernel. This result is shown diagrammatically in Fig. 2. I emphasize that minimal substitution for the $P^\mu_\pm$ at each *different* meson vertex leads to a replacement by the *same* current operator, and that this current operator is the known *nucleon* current. This remarkable result is due to the principle of *picture independence*, as discussed in Ref. I. Then, using the bound-state wave equation to absorb the truncated kernels leads to two new effective vertex functions $\Gamma^{(i)}$ (and their Dirac conjugates), leading to the final result shown in Fig. 3. Figure 3(A$^{(2)}$) $\equiv$ 3(A$_+^{(2)}$)+3(A$_-^{(2)}$) is the contributions from $\Gamma^{(2)}_\pm$ (which is reduced to a single diagram using symmetry). Similarly, Fig. 3(B) $\equiv$ 3(B$_+$)+3(B$_-$), with the subtracted vertex function $\widehat{\Gamma}_{\rm BS}=\Gamma_{\rm BS}-\Gamma^{(1)}$, includes the combined contributions from Figs. 1(B$_\pm$) and the $\overline{V}^{(1)}_\pm$ contributions from the interaction current. The diagrams of Fig. 3 are completely equivalent to the five diagrams shown in Fig. 2 of Ref. II (but the labeling of the momenta in those diagrams differs from the choice here).

Figures 3(A) and 3(A$^{(2)}$) describe the interaction of the photon with particle 2, allowing particle 1 to be on shell in both the initial and final state. The internal momenta are

$$k=\{E_k,\mathbf{k}\}\equiv\widehat{k},\qquad p_\pm=P_\pm-k, \tag{1.3}$$

where P_+ (P_-) are the four-momenta of the outgoing (incoming) deuterons, and the hat symbol over a four-vector means that the four-vector is on shell. Figure 3(B) describes all the interactions of the photon with particle 1, so that both particles must be off shell in either the initial or in the final state. Here the internal momenta are

$$\widetilde{k}=\{k_0,\mathbf{k}\},\qquad \widetilde{p}=P_\pm-\left(\widetilde{k}\pm\tfrac{1}{2}q\right). \tag{1.4}$$

The final (initial) nucleon is on shell when $k_0=E_+$ (E_-), with

$$E_\pm=\sqrt{m^2+\left(\mathbf{k}\pm\frac{\mathbf{q}}{2}\right)^2}. \tag{1.5}$$

D. Strong form factor h and the bound nucleon current

In this section, I describe two central features of the CST calculation of the deuteron observables and form factors from the diagrams in Fig. 3. These are (i) the presence of a strong nucleon form factor, h, and (ii) the structure of the bound nucleon current, which depends on *four* form factors: not only the usual Dirac and Pauli form factors F_1 and F_2, but also two off-shell form factors F_3 and F_4. The first of these, F_3, has been discussed extensively in previous work, but F_4 has never been introduced before and is a major new feature of this paper.

1. *The strong nucleon form factor* $h(p)$

In all strong, nonperturbative theories of hadronic structure, there is a need to include form factors that cut off high-momentum contributions and provide convergent results. In the CST-OBE models studied so far, the form factors at the meson-NN vertices are assumed to be *products* of strong form factors for each particle entering or leaving the vertex. This means that for each nucleon with momentum p entering or leaving a vertex, there is a universal *strong* nucleon form factor $h(p)$ (a function of p^2 only) present at that vertex. This

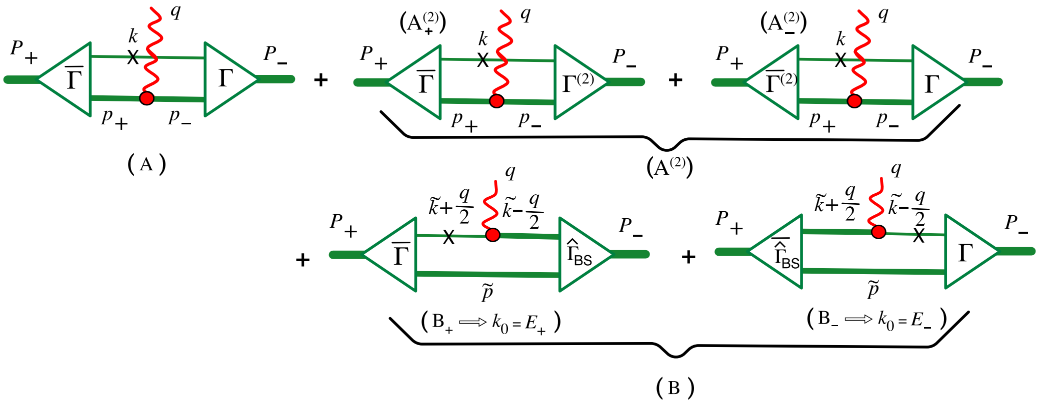

FIG. 3. Using the consequences of current conservation (as represented in Fig. 2), the diagrams in Fig. 1 can be transformed into the diagrams shown above. Diagram (A) is unchanged. The two diagrams (A$_\pm^{(2)}$) arise from the interaction current contributions $\overline{V}^{(2)}_\pm$; their sum will be referred to collectively as diagram (A$^{(2)}$). The diagrams (B$_\pm$) are the sum of the diagrams (B$_\pm$) of Fig. 1 plus the interaction current contributions $\overline{V}^{(1)}_\pm$. The sum of these two diagrams, expressed in terms of the off-shell momentum $\widetilde{k}$, is referred to as diagram (B). Off-shell nucleon lines are thicker than on-shell lines.

form factor is normalized so that when $p = \hat{p}$ (so that p is on shell), $h(\hat{p}) = 1$.

Because it is universal, the strong form factor associated with each external nucleon line can be factored out from the NN scattering kernel, giving

$$\overline{V}(k, k'; P) = h(k)h(p)\widetilde{V}(k, k'; P)h(k')h(p'), \qquad (1.6)$$

where k (k') are the four-momentum of the outgoing (incoming) particle 1, $\widetilde{V}$ is the *reduced* kernel and, for both primed and unprimed variables, $p = P - k$. Note that the expression for the kernel is written allowing for the possibility that any (or all four) of the particles could be off shell. Similarly, removing the strong form factors from the vertex function gives a *reduced* vertex function $\widetilde{\Gamma}_{BS}$, where

$$\widehat{\Gamma}_{BS}(k, P) = h(k)h(p)\widetilde{\Gamma}_{BS}(k, P). \qquad (1.7)$$

Since $h(p)$ is included in the kernel, and $h(\hat{k}) = 1$ when particle 1 is on shell, the dependence of the results on variations of $h(p)$ when particle 1 is on shell has already been studied in the fits to the NN scattering and presents nothing new. However, when electromagnetic current conservation is imposed, the presence of $h(p)$ leads to a modification of the nucleon current. This h dependence is a new feature of the relativistic theory that is interesting to study. In addition, when particle 1 is off shell, so that $k \neq \hat{k}$, the dependence of the calculation on $h(p)$ for $k_0 - E_\pm \neq 0$ is another feature of the relativistic theory that is new.

I will report on some of these effects later in Sec. III; for now I only want to highlight existence of the strong form factor h, because its presence drives the discussion of the bound nucleon current.

2. *Structure of the bound nucleon current*

Using interactions that depend only on Δ, the momentum transfer by the interacting particles, Feynman showed a long time ago that current conservation could be proved if the off-shell bound nucleon current satisfied the Ward-Takahashi (WT) identity

$$q_\mu\, j_0^\mu(p', p) \;= e_0[S^{-1}(p) - S^{-1}(p')], \qquad (1.8)$$

where $S(p)$ is the propagator of a bare nucleon, which in my notation (with the i's removed) is

$$S(p) = \frac{1}{m - \not{p} - i\epsilon}. \qquad (1.9)$$

When a strong nucleon form factor is present, the interactions in a one-boson exchange (OBE) model will be of the form $h(p)V(\Delta)h(p')$ and can be made to depend only on Δ if the strong nucleon form factors coming from the initial and final interactions that connect each propagator are moved from the interactions to the propagators connecting them. Since each propagator connects two interactions, the new (dressed) nucleon propagator then has the form

$$S_d(p) = h^2(p)S(p). \qquad (1.10)$$

Now a similar proof of current conservation is possible [17] provided a *reduced* current $j_R^\mu(p', p)$ is constructed,

$$j^\mu(p', p) = h(p')h(p)j_R^\mu(p', p), \qquad (1.11)$$

and required to satisfy a generalized WT identity

$$q_\mu\, j_R^\mu(p', p) = e_0\big[S_d^{-1}(p) - S_d^{-1}(p')\big]. \qquad (1.12)$$

There are many solutions to (1.12). The one I use in this paper is

$$\begin{aligned} j^\mu(p', p) = {}& e_0\, f_0(p', p)\left[\mathcal{F}_1^\mu + F_2(Q^2)\frac{i\sigma^{\mu\nu}q_\nu}{2m}\right] \\ & + e_0\, g_0(p', p)\Theta(p')\left[\mathcal{F}_3^\mu + F_4(Q^2)\frac{i\sigma^{\mu\nu}q_\nu}{2m}\right]\Theta(p), \end{aligned} \qquad (1.13)$$

where f_0, g_0 are (uniquely determined) off-shell functions discussed below, $e_0 = \frac{1}{2}$ is the isoscalar charge, the off-shell projection operator Θ was defined in (1.2),

$$\begin{aligned} \mathcal{F}_i^\mu &= [F_i(Q^2) - 1]\widetilde{\gamma}^\mu + \gamma^\mu \\ &= F_i(Q^2)\widetilde{\gamma}^\mu + \frac{\not{q}q^\mu}{q^2}, \end{aligned} \qquad (1.14)$$

and the transverse γ matrix is

$$\widetilde{\gamma}^\mu = \gamma^\mu - \frac{\not{q}q^\mu}{q^2}, \qquad (1.15)$$

with $q = p' - p$. Except for the addition of the new form factor F_4, this is precisely the current that has been used in all previous work.

3. *Uniqueness of the bound nucleon current and the principle of balance*

The longitudinal parts of the current (1.13) are largely determined by the generalized WT identity (1.12). Still, as (1.14) displays, the important physics contained in the form factors F_1 and F_3 is purely *transverse*, and the longitudinal part that is constrained by the WT identities will *not contribute to any observable* since it is proportional to q^μ which vanishes when contracted into any conserved current or any of the three polarization vectors of an off-shell photon. The form factors themselves are completely unconstrained by current conservation, except for the requirement that $F_1(0) = F_3(0) = 1$ (with the real normalization set by e_0). This is as it should be; the structure of the nucleon should not be fixed by the general requirement of current conservation.

Similarly, the transverse Pauli-like terms F_2 and F_4 are completely unconstrained, and there are may other off-shell terms that one could add to the current. What principal is to constrain these?

In Ref. I, I introduced the principles of *simplicity* and *picture independence* in an attempt to limit possible contributions. I found that, using current conservation and these principles, all contributions from the structure of the meson-nucleon vertices could be expressed in terms of the nucleon structure F_1 alone; no new interactions, such as the famous $\rho\pi\gamma$ interaction current, needed to be added. However, these arguments placed no constraint on the F_2 term. Clearly it must be included because the free nucleon cannot be described without it, but the choice of whether or not to multiply the F_2 term by f_0 is not dictated by these principles. Similarly, I emphasize that the introduction of F_4 is *not required by the* *principles of simplicity or picture independence*. To justify the introduction of F_4 and to explain the use of the same f_0 for both F_1 and F_2, and the same g_0 terms for F_3 and F_4, a new principle is needed.

The new principle will be referred to as the principle of *balance* between Dirac and Pauli interactions. The principle states that whenever a Dirac-like charge term (F_1 and F_3 in this case) is required, a similar Pauli-like term (F_2 and F_4) will be included. This ensures that the off-shell current, expressed in terms of the F_3 and F_4 form factors, could also be expressed in terms of off-shell charge ($G_E^{\rm off}$) and magnetic ($G_M^{\rm off}$) form factors, without a constraint on the structure of either (except for the previously discussed constraint $F_3(0) = 1$).

4. Properties of f_0 and g_0

The simplest solution to (1.12) is

$$\begin{aligned} f_0(p', p) &= \frac{h'}{h}\left[\frac{m^2 - p^2}{p'^2 - p^2}\right] + \frac{h}{h'}\left[\frac{m^2 - p'^2}{p^2 - p'^2}\right], \\ g_0(p', p) &= \frac{4m^2}{p'^2 - p^2}\left[\frac{h}{h'} - \frac{h'}{h}\right], \end{aligned} \tag{1.16}$$

where I use the the shorthand notation $h = h(p)$ and $h' = h(p')$. Both f_0 and g_0 are symmetric in p', p, and important limits are

$$\begin{aligned} f_{00}(p^2) &= \lim_{p'^2\to p^2} f_0(p', p) = 1 + 2a(p^2)(m^2 - p^2), \\ f_{01}(p^2) &= \lim_{p'^2\to m^2} f_0(p', p) = \lim_{p'^2\to m^2} f_0(p, p') = \frac{1}{h}, \\ g_{00}(p^2) &= \lim_{p'^2\to p^2} g_0(p', p) = -8m^2 a(p^2), \end{aligned} \tag{1.17}$$

where

$$a(p^2) = \frac{1}{h}\frac{dh}{dp^2}. \tag{1.18}$$

E. Definitions of deuteron observables

Precise definitions of the deuteron form factors will be reviewed in Appendix A. For an understanding of the results to be presented in Sec. II, it is only important to review that electron-deuteron scattering is described by three independent deuteron form factors [10,11]: G_C (charge), G_M (magnetic), and G_Q (quadrupole). Denoted generically by G_X (with $X = \{C, M, Q\}$). These form factors are a sum of products of *isoscalar* nucleon form factors, $F_i(Q^2)$ (where the subscript s labeling these as isoscalar will be omitted throughout this paper for simplicity), and *body* form factors, $D_{X,i}(Q^2)$, so that

$$G_X(Q^2) = \sum_{i=1}^{4} F_i(Q^2) D_{X,i}(Q^2). \tag{1.19}$$

It is important to realize that the theory presented in this paper calculates the body form factors only; the nucleon form factors must be obtained from another source.

The deuteron form factors can be measured by the analysis of three independent experiments. Two of these can be obtained from the unpolarized elastic scattering of electrons from the deuteron. In one-photon exchange approximation, this elastic scattering is given by

$$\frac{d\sigma}{d\Omega} = \frac{d\sigma}{d\Omega}\bigg|_{NS}[A(Q^2) + B(Q^2)\tan^2(\theta/2)], \tag{1.20}$$

where

$$\frac{d\sigma}{d\Omega}\bigg|_{NS} = \frac{\alpha^2 E' \cos^2(\theta/2)}{4E^3\sin^4(\theta/2)} = \sigma_M\frac{E'}{E} = \frac{\sigma_M}{1 + \frac{2E}{m_d}\sin^2\frac{1}{2}\theta} \tag{1.21}$$

is the cross section for scattering from a particle without internal structure (σ_M is the Mott cross section), and $\theta, E,\ E'$, and $d\Omega$ are the electron scattering angle, the incident and final electron energies, and the solid angle of the scattered electron, all in the laboratory system. The structure functions A and B, which can be separated by comparing unpolarized measurements in the forward and backward directions, depend on the three electromagnetic form factors

$$\begin{aligned} A(Q^2) &= A(G_C) + A(G_M) + A(G_Q) \\ &= G_C^2(Q^2) + \tfrac{8}{9}\eta^2 G_Q^2(Q^2) + \tfrac{2}{3}\eta G_M^2(Q^2), \\ B(Q^2) &= \tfrac{4}{3}\eta(1+\eta)G_M^2(Q^2), \end{aligned} \tag{1.22}$$

where

$$\eta = \frac{Q^2}{4M_d^2}. \tag{1.23}$$

To further separate G_C and G_Q, the polarization of the outgoing deuteron can be measured in a separate, analyzing scattering. The quantity most extensively measured is

$$\widetilde{T}_{20} = -\sqrt{2}\,\frac{y(2+y)}{1+2y^2}, \tag{1.24}$$

where

$$y = \frac{2\eta G_Q}{3G_C}. \tag{1.25}$$

Note that the structure function B depends only on G_M, and T_{20} depends on y, both of which are *linear* in the the nucleon form factors. However, the structure function A is quadratic in the nucleon form factors.

II. FITS TO THE DEUTERON OBSERVABLES

A. Introduction

All results for the deuteron form factors depend on the off-shell nucleon form factors $F_3(Q^2)$ and $F_4(Q^2)$. However, except for the sole requirement that $F_3(0) = 1$, these form factors are completely unknown, and it is appropriate to use the deuteron form factor data to determine them. The first step, determining F_3 and F_4, is done in Sec. II B below.

I have found that the most efficient way to do this is to use the data from G_M (determined directly from B) and $\widetilde{T}_{20}$ [actually y from Eq. (1.25)]. Both G_M and y are linear in F_3 and F_4, so a solution is straightforward and it is easy to determine the errors in F_3 and F_4 from the errors in G_M and y. Details are given in Appendix C.

The data are scattered, and to do this efficiently it would first be necessary to find a smooth fit to all the data.

TABLE I. Summary of theoretical models discussed in this paper. All models listed in the table have *no* $\rho\pi\gamma$ exchange current, except for model VODG. The model GK05 is discussed in Ref. [19] and shown in Fig. 12.

Name	Deuteron	G_{En}	F_3	F_4	Color	Line
VODG[a]	IIB	GK05	Dipole	0	Black	Long-dash
VODG0	IIB	GK05	Dipole	0	Black	2 dash–2 dot
1A	WJC1	GK05	Dipole	0	Blue	Short-dash
2A	WJC2	GK05	Dipole	0	Red	Short-dash
1B	WJC1	GK05	$F_3(1)$	$F_4(1)$	Blue	2 dash–2 dot
2B	WJC2	GK05	$F_3(2)$	$F_4(2)$	Red	2 dash–2 dot
2C	WJC2	CST2	$F_3(2)$	$F_4(2)$	Red	Long dash-dot
2D	WJC2	CST1	$F_3(2)$	$F_4(2)$	Red	Thick solid

[a] Model VODG includes a $\rho\pi\gamma$ exchange current calculated using the Rome 2 $\rho\pi\gamma$ form factor [20].

Fortunately, Sick has produced a global analysis (GA) [12,18], where he reanalyzed all of the data starting from the detailed records. I will use his GA for a representation of the data. Once F_3 and F_4 have been determined, the data (that is, the Sick GA) for B and $\widetilde{T}_{20}$ are exactly reproduced, as shown in Sec. II C.

Note that $\widetilde{T}_{20}$ determines only the *ratio* of the independent form factors G_C and G_Q, not their size. The third observable, A, can vary even when B and $\widetilde{T}_{20}$ are fixed. This is studied in Sec. II D, where it is shown that G_{En} can be adjusted to give the correct A (fortunately, B and $\widetilde{T}_{20}$ are very insensitive to G_{En}, so that this determination of G_{En} does not alter the fits to B and $\widetilde{T}_{20}$). The predictions for G_{En} made by each model is discussed in Sec. II D, where it is shown that model WJC1 fails at this point, but model WJC2 works very well. Finally, using the predicted F_3 and F_4 and various models of G_{En}, Sec. II E presents the deuteron form factors and compares them to Sick's GA.

In order to keep the number of figures to a minimum, the reader is warned that some of the early figures will show results for models that will not be introduced until later in the discussion. To help with this, all of the models that will be used are summarized in Table I. Models 1A and 2A are a starting point; their input is the same as the successful VODG calculation (except I never have any $\rho\pi\gamma$ interaction current). Model VODG used the GK05 prediction of G_{En}, and in the absence of any previous knowledge, assumed a standard dipole for F_3 and $F_4 = 0$. Then, models 1B and 2B replace F_3 and F_4 by the solutions found in Sec. II B, giving precise fits to B and $\widetilde{T}_{20}$. Finally, models 2C and 2D show the results of using models for G_{En} based on the predictions given in Sec. II D and cannot be understood until that section is studied.

B. Predictions for the off-shell nucleon form factors

As mentioned in the introduction, the off-shell form factors can be found by simultaneously fitting them to the GA data points for G_M and T_{20} (which is independent of G_M). Each GA point has its own error that I use to estimate the errors in the fitted values of the form factors. The results obtained from models WJC1 and WJC2 are shown in Figs. 4 and 5. Each red and blue point in the figure is the (simultaneous) solution for F_3 and F_4 at each GA point, which extend out to $Q = 7\,(\mathrm{fm})^{-1} = 1.379\,(\mathrm{GeV})$ (limited by the measurements of T_{20}).

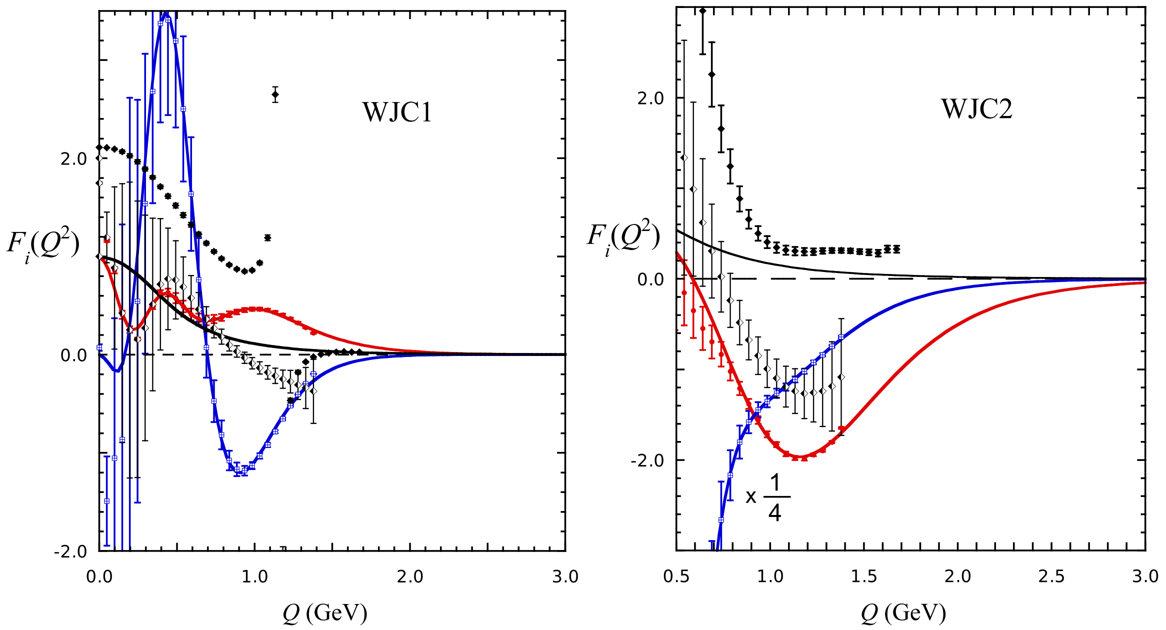

FIG. 4. Results for model WJC1 (left panel) and model WJC2 (right panel). Both panels show $F_3(Q^2)$ (small red circles) and $F_4(Q^2)$ (small blue squares) obtained by simultaneously fitting to Sick's GA for G_M and T_{20}. Only the error bars obtained from the errors in Sick's G_M are shown, reflecting the fact that the requirements to fit G_M are far more stringent than those necessary to fit T_{20}. (Note that F_4 for model WJC2 is four times larger than shown in the figure.) The panels also show the results for F_3 fitted to G_M (solid black diamonds) or to T_{20} (half filled black diamonds) when $F_4 = 0$. The smooth black curve is the dipole model and the red and blue curves are the fits discussed in the text.

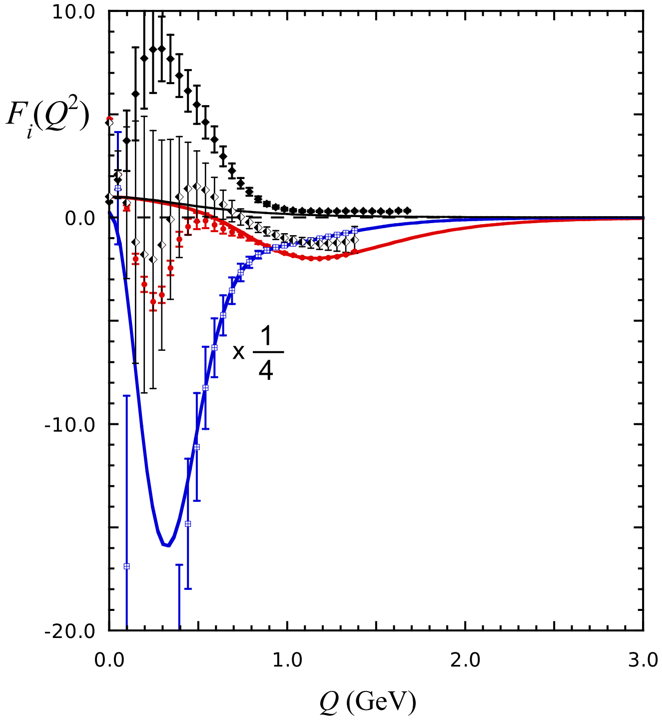

FIG. 5. Same results as shown in the right panel of Fig. 4, but on a bigger scale, which allows a fuller picture of the form factors at smaller Q. (Note that F_4 is four times larger than shown in the figure.)

In the same figures, I also show the values obtained by fitting F_3 separately to G_M (solid black diamonds) or T_{20} (half filled black diamonds) *under the assumption* that $F_4 = 0$. The fact that these fits differer substantially shows that it is not possible to obtain a good fit to the GA data without including a nonzero F_4.

Note that the form factors are largely undetermined at $Q \gtrsim 1.4$ GeV, and also at small Q where the errors in the fitted form factors are large. In order to have results for all Q, and especially beyond the range where data for T_{20} exists, I chose smooth curves that fit the points in the range $0.5 \gtrsim Q \gtrsim 1.3$ GeV, where they are well constrained. The generic models used for F_3 and F_4 are

$$
\begin{aligned}
F_3(Q^2) &= \frac{1 + aQ^2 + bQ^4 + cQ^6 + dQ^8}{(1 + eQ^2)^n},\\
F_4(Q^2) &= \frac{aQ^2 + bQ^4 + cQ^6 + dQ^8}{(1 + eQ^2)^9},
\end{aligned}
\tag{2.1}
$$

where $n = 7$ for WJC1, $n = 9$ for WJC2, and the other parameters are given in Table II. The asymptotic limits of these form factors are

$$
\begin{aligned}
\lim_{Q^2\to\infty} F_3 &= \frac{\text{const}}{Q^{2n-8}} \sim \begin{cases} Q^{-6} & \text{WJC1} \\ Q^{-10} & \text{WJC2} \end{cases},\\
\lim_{Q^2\to\infty} F_4 &= \frac{\text{const}}{Q^{10}},
\end{aligned}
\tag{2.2}
$$

and note that I have constrained

$$
\lim_{Q\to 0} F_4 = aQ^2. \tag{2.3}
$$

TABLE II. Parameters for the fits to F_3 and F_4 with Q in GeV. Here $F_i(\mathrm{X}) \equiv F_i(\mathrm{WJCX})$.

	$F_3(1)$	$F_3(2)$	$F_4(1)$	$F_4(2)$
a	−30.905	1.3508	−29.467	−1747.8
b	457.66	4.0568	1141.0	2395.0
c	−1401.7	0	−2422.0	0
d	1618.9	−137.69	404.21	−3370.4
e	1.2323	0.6131	1.1115	1.0004

Finally, I point out that the models for these form factors are real analytic functions with cuts in the complex q^2 plane along the positive real axis. For the model WJC2, these cuts start at

$$
q^2 = -Q^2 = 1/e = \begin{cases} 1.63\ \text{GeV}^2 & F_3(2) \\ 1.00\ \text{GeV}^2 & F_4(2). \end{cases} \tag{2.4}
$$

Both cuts start near or above the the $7m_\pi$ threshold, confirming that they are short-range effects. Similar results hold for $F_i(1)$. I have not investigated the dispersion relations that these functions satisfy.

C. Fits to $B(Q^2)$ and $T_{20}(Q^2)$

With the off-shell form factors determined, I now confirm that the fits to $B(Q^2)$ and $T_{20}(Q^2)$ do indeed agree with the Sick GA. (The fits to G_M, related to B, will be shown later when the other form factors are discussed.) This is also an opportunity to compare the results for models WJC1 and WJC2 with the previous successful calculation of Van Orden *et al.* [8], which is refered to as VODG. The various models under discussion in this and the following sections are defined in Table I and will be referred to by the simple names given in the table.

I begin by showing the data for $B(Q^2)$ in Fig. 6. The rapid variation of B with Q makes it difficult to see how the theory compares with data, so I have scaled everything by the simple fit function

$$
\begin{aligned}
\text{fit}B = {} & 0.4 \exp(-2.2\,Q/0.197)\\
& + 0.7 \times 10^{-6} \exp(-0.35\,Q/0.197),
\end{aligned}
\tag{2.5}
$$

where Q is measured in GeV, and the tail was adjusted to be near an expected secondary maximum in B. The results of dividing both data and predictions by this function are shown in Fig. 7. This figure also shows how the various theoretical models shown in Table I compare with the experimental data and the Sick GA. Figure 8 shows how the models and Sick GA compare with the experimental data for T_{20}.

Study of the curves in Figs. 7 and 8 show that models 1A and 2A, with the same assumptions as VODG (standard dipole for F_3, $F_4 = 0$, and GK05 nucleon form factors) are both successful at low $Q \lesssim 1$ GeV, but 1A seriously overshoots B at higher Q and 2A undershoots B already at about $Q \simeq 0.5$. Model VODG overshoots B a little near $Q \sim 1$ GeV (this will be more clearly displayed when I show G_M below), but the discrepancy is smaller than either models 1A or 2A. VODG gives a better explanation than either models 1A and 2A.

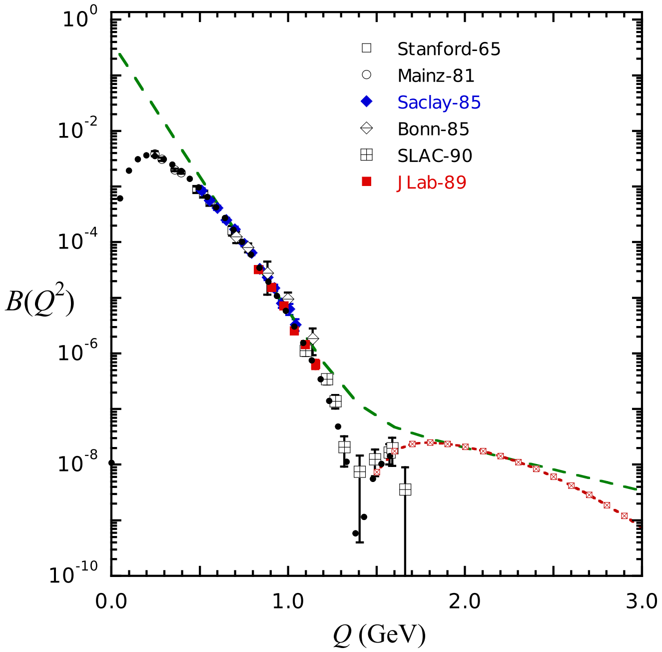

FIG. 6. Data for the magnetic structure function $B(Q^2)$ compared to Sick's GA (small solid black circles). The function fit$B$ (dashed green line) is shown for comparison. The data are Stanford-65 [21], Mainz-81 [22], Saclay-85 [23], Bonn-85 [24], SLAC-90 [25,26], and JLab-89 [27,28]. The high-Q tail of model 2B (cf. Table I), used to construct the high-Q tail of fit$B$, is the red dashed line connected to red squares.

As expected, models 1B and 2B, that use the appropriate F_3 and F_4 for each model, do indeed give excellent agreement with the $B(Q^2)$ structure function and $T_{20}(Q^2)$ over the entire region where the GA exists. Note that the size of the $\rho\pi\gamma$ exchange current used by VODG can be inferred from the differences between VODG0 and VODG and is smaller than the effects arising from F_3 and F_4, particularly for model WJC2.

Finally, the figures show the important result that the best models, 2C and 2D that have not yet been introduced, are practically indistinguishable from 2B in the region of the GA fit. Their significance will be discussed in the next section.

D. Predictions for $A(Q^2)$ and $G_{En}(Q^2)$

To complete the picture, Fig. 9 shows the data and predictions for $A(Q^2)$ similar to those shown for $B(Q^2)$ in Fig. 6. This figure shows nicely how $A(Q^2)$ falls as an exponential over many decades. As was the case for B, comparing theory to data on such a curve obscures all but huge differences. To see differences of a factor of 2 or 3, the A structure function is scaled by the simple function

$$\text{fit}A = 0.2\exp(-1.5\,Q/0.197) \tag{2.6}$$

(where Q is measured in GeV), and Figs. 10 and 11 show these scaled results, which play a role in my discussion of A similar to that played by Fig. 7 in my discussion of B. To emphasize the differences at large Q, Fig. 11 is the same as Fig. 10, but with the scales expanded.

Figures 10 and 11 show that all theoretical models give an excellent description of A at $Q \lesssim 0.7$ GeV. However (excluding models 2C and 2D for now) none of the models do very well describing the GA significantly above $Q \sim 0.7$ GeV. VODG does the best (with the $\rho\pi\gamma$ exchange current playing a decisive role), model 2B is not far off, but models 1A

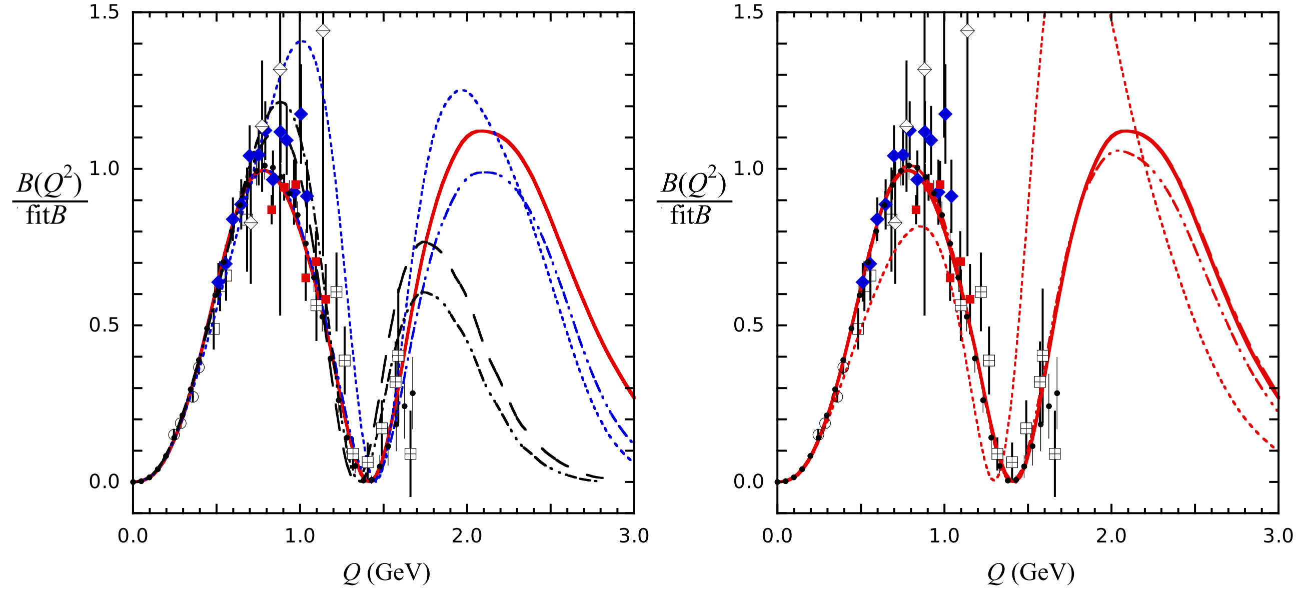

FIG. 7. The same data for the magnetic structure function $B(Q^2)$ shown in Fig. 6, Sick's GA, and various theoretical predictions all scaled by the function fit B, Eq. (2.5). Both panels show the data, the GA, and model 2D (thick red solid line). The left panel also shows models 1A (blue short-dashed line), 1B (blue double-dash-dotted line), VODG (black long-dashed line), and VODG0 (black double-dash-dotted line). The right panel shows models 2A (red short-dashed line), 2B (red double-dash-dotted line), and 2C (red long-dash-dotted line). Note that models 2C and 2D are nearly indistinguishable.

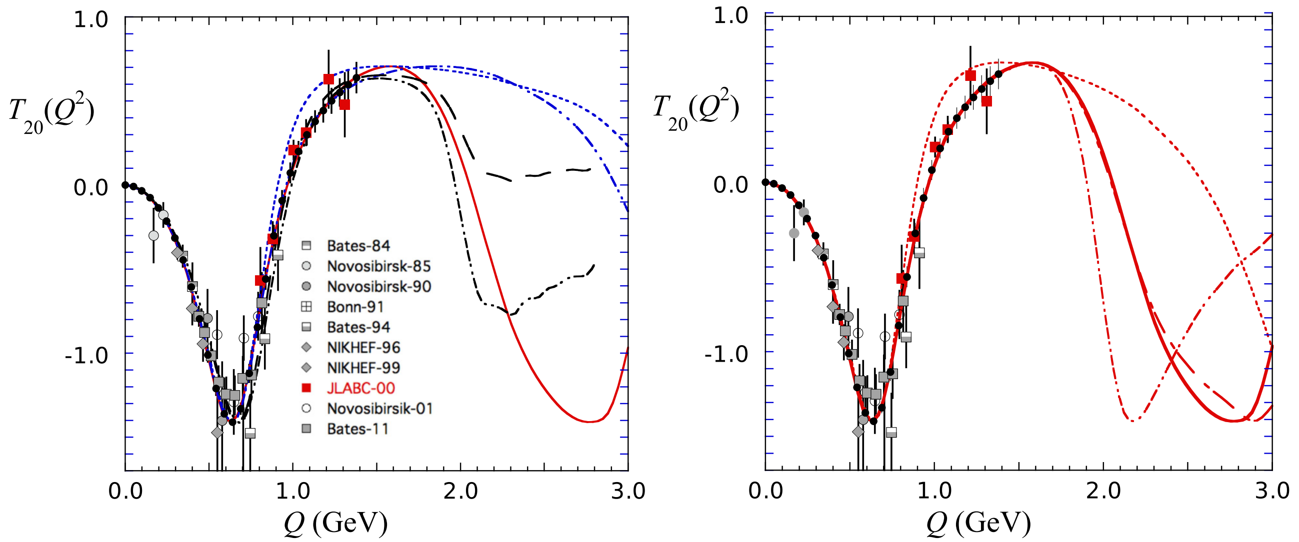

FIG. 8. The data for T_{20} compared to Sick's GA (black dots) and the same theoretical models labeled as they were in Fig. 7 and Table I. The data are Bates-84 [29], Novosibirisk-85 [30,31], Novosibirisk-90 [32], Bonn-91 [33], Bates-94 [34,35], NIKHEF-96 [36], NIKHEF-99 [37], JLabC-00 [38], Novosibirisk-01 [39], and Bates-11 [40].

and 1B, and 2A all depart substantially from the GA and are clearly unacceptable. This means that even when the two unknown off-shell form factors F_3 and F_4 are adjusted to fit B and T_{20}, model WJC1 disagrees with the data for A by such a large amount that it cannot be repaired, as discussed in the next section.

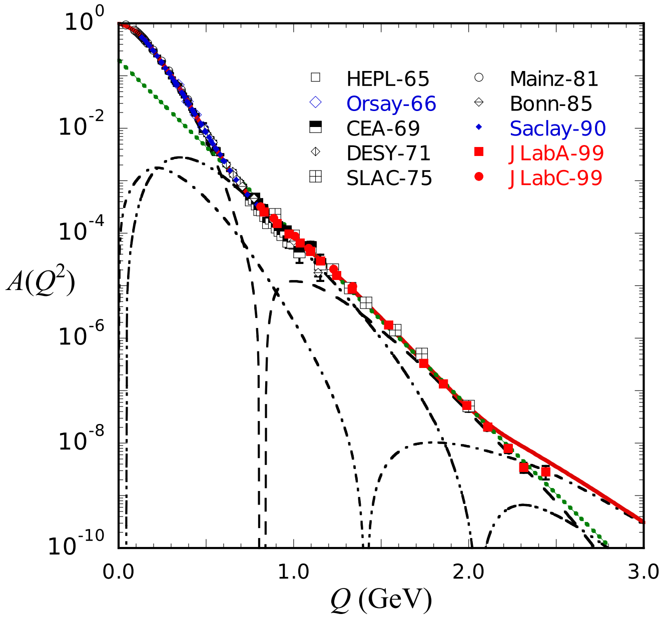

FIG. 9. Data for the structure function $A(Q^2)$. The function fit$A$ (linear green dotted line) is shown for comparison. The theoretical curves are model 2D (red line and three black lines) and are discussed in the text. The data are HEPL-65 [21], Orsay-66 [41], CEA-69 [42], DESY-71 [43], SLAC-75 [44], Mainz-81 [22], Bonn-85 [24], Saclay-90 [45], JLabA-99 [46], and JLabC-99 [47].

Note that model 2B does well out to $Q \sim 1.4$ GeV, but dips below the data in the region from $1.5 \lesssim Q \lesssim 2.2$ GeV. This is a region where the nucleon charge form factor, G_{En}, is unknown, and hence this calculation can be used to *predict* G_{En} in this region.

Models 2C and 2D will be discussed below, and the failure of any of the models to describe A at the highest values of Q will be discussed in the conclusions section.

The values of G_{En} required to bring each model into agreement with the GA points for $A(Q^2)$ are shown in Fig. 12. The GA fits to $A(Q^2)$, shown Figs. 10 and 11, extend out to $Q \gtrsim 1.576\ (\text{GeV}) = 8\ (\text{fm})^{-1}$, well beyond the region where $B(Q^2)$ is known. However, since A is quadratic in G_{En} (but only one root is acceptable; see the discussion in Appendix D), there is no guarantee that a real solution can be found at each point. It is remarkable that real solutions do exist except at the highest values of Q. I found that there were *no solutions* for model WJC1 at the three highest GA points ($Q \geqslant 2.319$ GeV) and for WJC2 at the five highest GA points ($Q \geqslant 2.216$ GeV). The errors shown are determined by the GA errors in A only; at high Q the theory depends on the *extrapolations* obtained from the fits $F_3(i)$ and $F_4(i)$ (where $i = 1, 2$), and hence are subject to additional errors I have not tried to estimate.

Here one has a very different situation from my previous study of F_3 and F_4. Measurements of G_{En} from *free* neutrons using recoil polarization [48–53] are completely independent of any theory of the deuteron, and those from a polarized deuteron target [54–56] are almost as clean. All of these measurements are shown in Fig. 12, and I chose to focus only on them because they are insensitive to deuteron theory. For a recent review of the experimental data, see Ref. [57]; many other measurements exist.

Figure 12 shows that the solution for G_{En} for model WJC1 is in serious disagreement with the form factor measurements from free neutrons. There seems to be no way to repair model

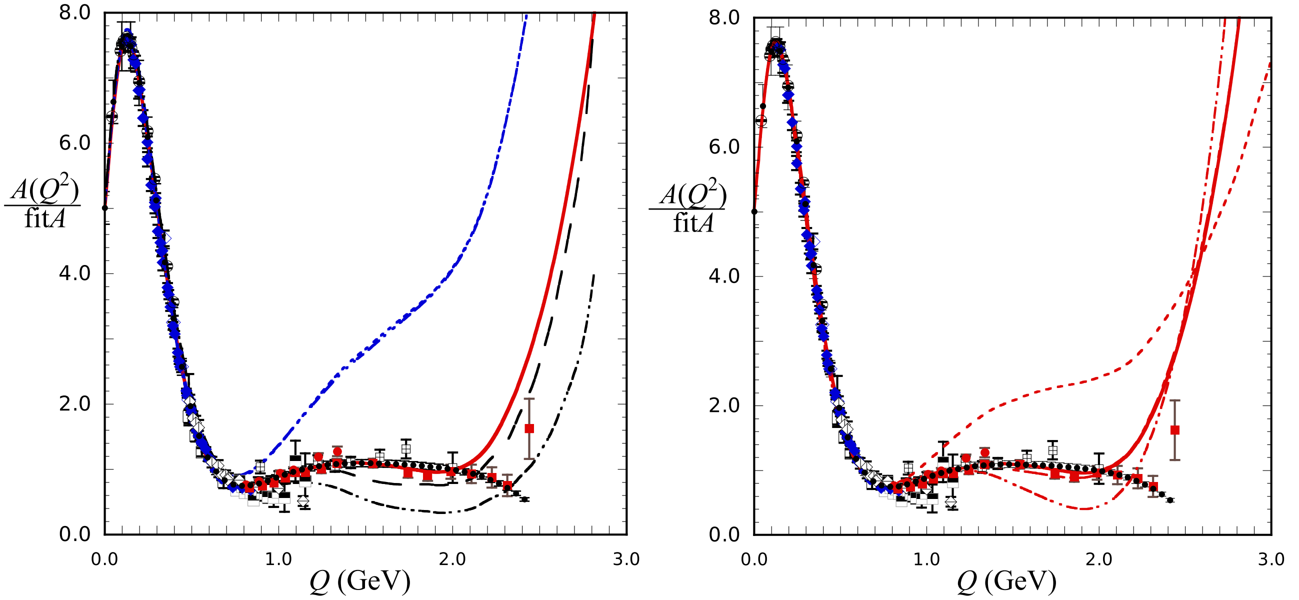

FIG. 10. The same data for the structure function $A(Q^2)$ shown in Fig. 9, Sick's GA (small black solid circles), and various theoretical predictions all scaled by the function fit A, Eq. (2.6) (and all drawn with the same line style used in Figs. 7 and 8 and Table I). Both panels show model 2D. The left panel shows models 1A and 1B, almost indistinguishable from each other, and VODG and VODG0. The right panel shows models 2A, 2B, and 2C.

WJC1; for this reason, I did not study the predictions for model WJC1 further.

In contrast, the solution for G_{En} from model WJC2 is in good agreement with the free data. To study various possibilities, I decided to represent G_{En} by the general functional form

$$G_{En}^{\text{model}}(Q^2) = \frac{aQ^2(1+bQ^2+cQ^4+dQ^6)}{(1+eQ^2)^6}, \tag{2.7}$$

which goes like Q^{-4} at large Q and has cuts only for positive q^2, required if it is to be represented by a dispersion relation. This functional form is so flexible that it can describe GK05 and two additional models of potential interest. The parameters used for these three models of G_{En} are given in Table III.

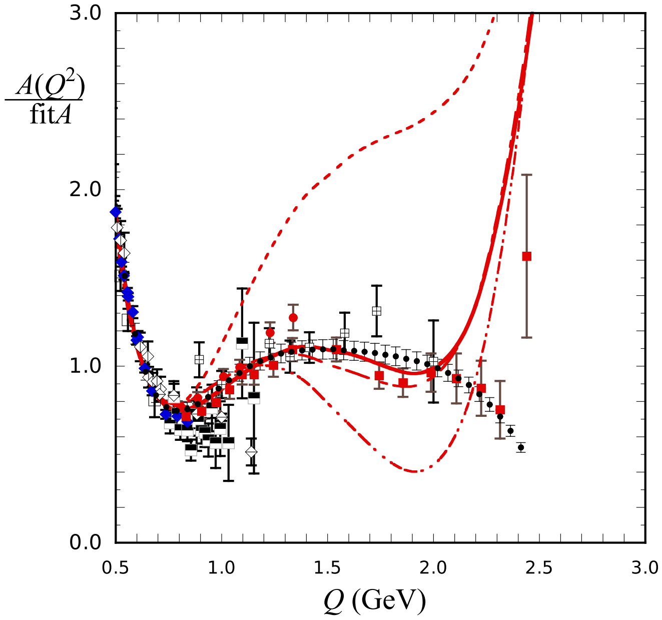

FIG. 11. The right panel of Fig. 10 with expanded scales.

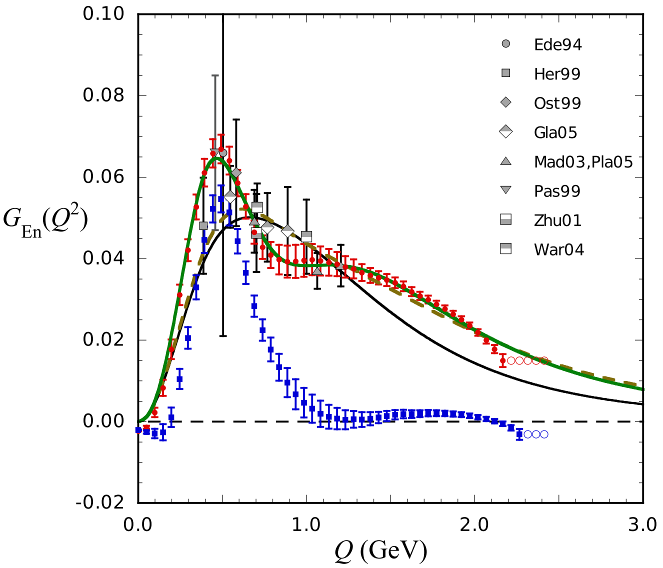

FIG. 12. Experimental data for G_{En} and "data," with errors, for G_{En} determined by fitting to Sick's GA points for A. The errors were obtained from the errors in A quoted by Sick. Solutions WJC1 are the blue points with smaller values of G_{En}; those for WJC2 are the red points. The small open circles at the highest momenta are points at which there is *no* solution for G_{En}. The models shown are GK05 (solid black line), CST1 (solid green line with the bump at at small Q), and CST2 (brown dashed line following GK05 at small Q and CST1 at larger Q). The experimental data are from Ede94 [48], Her99 [49], Ost99 [50], Gla05 [51], Mad03 [52], Pla05 [53], Pas99 [54], Zhu01 [55], and War04 [56].

TABLE III. Parameters for the G_{En} models using Eq. (2.7), with Q in GeV.

	GK05	CST1	CST2
a	0.4779	0.4930	0.4930
b	0.5798	16.254	0.5532
c	1.8452	−27.849	0.6805
d	0.4045	33.710	0.6861
e	0.8628	1.5836	0.7904

TABLE IV. Parameters for the scaling functions given in Eq. (2.8), with Q^2 in fm^{-2}.

	$G_C(n=1)$	$G_M(n=2)$	$G_Q(n=3)$
$a_1(n)$	0.6743	0.5149	0.4980
$a_2(n)$	0.0693	0.2912	0.0559
$a_3(n)$	0.0084	0.0013	0.00008
$b_0(n)$	1.8478	1.8422	1.2732
$b_1(n)$	0.4185	0.5252	0.2956
$b_2(n)$	0.1557	0.1749	0.0963
$b_3(n)$	0.0321	0.0204	0.0194

Model CST1 is a very good representation of the solution obtained from A, while model CST2 follows GK05 up to the highest Q^2 points [52,53] and then tracks CST1 at higher Q^2. All three of these models are shown in Fig. 12.

It turns out that both B and T_{20} are very insensitive to G_{En}, so my choice of a new G_{En} different from GK05 will not disturb my previous fits to B and T_{20} (this can be confirmed by noting that the left panels of Figs. 7 and 8 show almost no differences between models 2B, 2C, and 2D in the regions where they were used to obtain F_3 and F_4). Hence, the only effect of choosing a new G_{En} is an improvement in A, and as Fig. 11 shows, model 2D (with G_{En} represented by model CST1) provides an excellent fit to the data (except at the highest points, as discussed in the conclusions section), while model 2C (with G_{En} represented by model CST2) is almost as good, and this G_{En} tracks GK05 in the region where G_{En} has been measured. Final conclusions will be drawn in Sec. VI.

Predictions for the three form factors G_C, G_M, and G_Q are shown in the next subsection.

E. Predictions for the deuteron form factors

I now can complete the discussion by presenting the three deuteron form factors and comparing them to Sick's GA, which has been determined in the region $Q \lesssim 1.4$ GeV.

In order to better see the details, all form factors are normalized to unity at $Q = 0$, and divided by scaling functions with the same functional form as used in Ref. [12]:

$$\text{ScaleG}_n\ \ (Q^2) = \sum_{i=0}^{3} a_i(n)\exp[-b_i(n)Q^2], \tag{2.8}$$

where

$$a_0(n) = 1 - a_1(n) - a_2(n) - a_3(n), \tag{2.9}$$

ensuring that $\text{ScaleG}_n(0) = 1$. In order to scale the large-Q behavior of the form factors, I found it necessary to refit the coefficients, and the values I use in this paper are given in Table IV.

The scaled deuteron form factors are shown in Figs. 13 and 14. In the figures, I display the cases studied in the previous sections, even though the models 2C and 2D are the only ones that are in quantitative agreement with the Sick GA.

Note that model VODG predicts all of the form factors within 1–2 standard deviations over the entire range. Model 2B, designed to agree precisely with B and T_{20}, gives an exact description of G_M over the entire range (as expected) but fails to provide a precise explanation of G_C and G_Q. In the region $1 \lesssim Q \lesssim 1.4$, both $-G_C$ and G_Q are too large, so that their ratio, measured in T_{20}, is correct. Only models 2C and 2D give a precise explanation of all form factors.

I call attention to the contributions of the F_3 and F_4 form factors which are easy to see on these plots. Since F_3 cannot be zero (because of the constraint $F_3(0) = 1$), the best way to isolate the size of these contributions is to compare models 1A

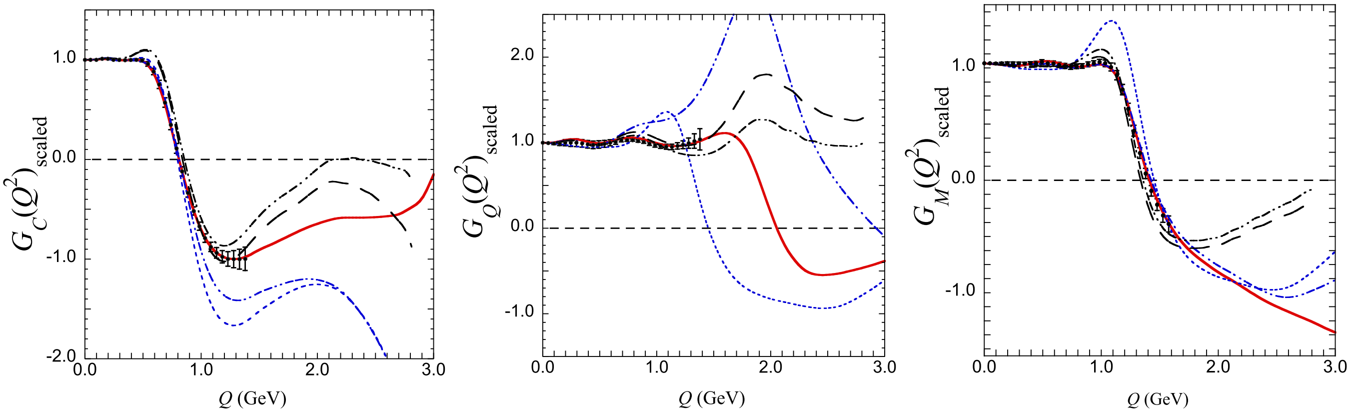

FIG. 13. Predictions for the three deuteron form factors for models VODG, VODG0, 1A, 1B, and 2D (with lines as in the previous figures) compared to the GA.

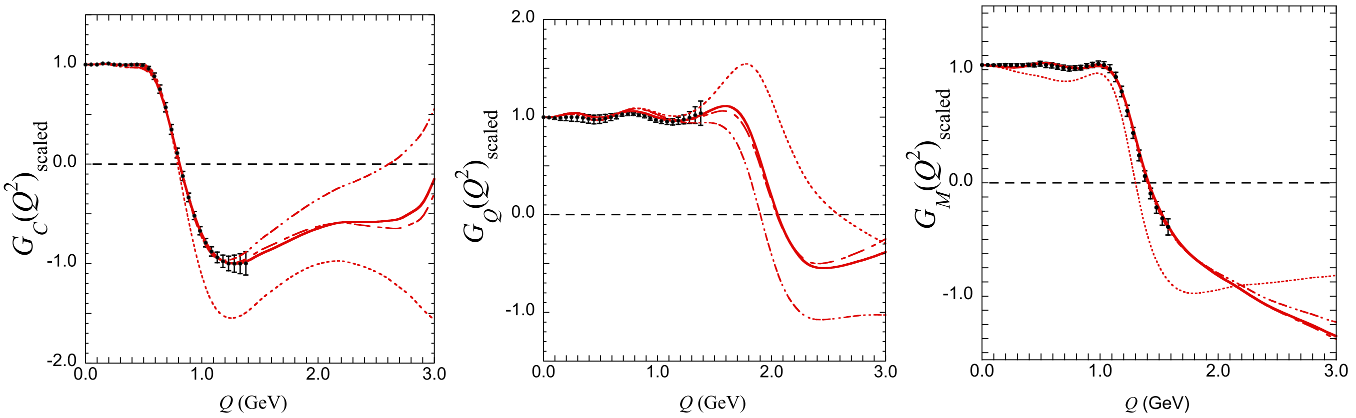

FIG. 14. Predictions for the three deuteron form factors for models 2A–2D (with lines as in the previous figures) compared to the GA.

and 1B, or models 2A and 2B, shown respectively by the short dashed and double dash-dotted lines (blue for WJC1 and red for WJC2). The figures show that that there is little difference at $Q \lesssim 0.6$ GeV, except that model 2A fails to describe G_M even at quite small Q.

Table V shows how closely models 2C and 2D predict Sick's GA (using Sick's error bars). Except for a few points in A at the highest Q (the tail), the fits are excellent, of comparable quality except for G_C, G_Q, and A, where model 2D provides a more accurate prediction than 2C.

Table VI shows the χ^2/datum for the published data compared to model 2D. Note that the CST prediction is in reasonable agreement with the data for B and T_{20}, but that there are large discrepancies with the data for $A(Q^2)$, even for $Q \leqslant 0.6$ GeV and that the measurements at the three largest Q points (JLabA) are in significant disagreement with the prediction (but the disagreement is not as large as with the Sick GA). I will discuss this further in the conclusions section.

III. PHYSICAL INSIGHTS

In this section, I study the size of various partial contributions to the form factors. The study is limited to model 2D, which gives the best fit to the Sick GA. Before discussing the individual contributions, it is helpful to briefly identify the ingredients of the theory.

TABLE V. The χ^2/datum for the predictions of models 2C and 2D compared to Sick's GA. The first point at $Q = 0.001$ fm^{-1} has been excluded.

	Number of points	2C	2D
G_C	28	3.613	0.116
G_M	32	0.713	0.763
G_Q	28	1.920	0.446
A	44	6.440	0.774
Atail	5	125.1	116.5
B	34	1.130	1.131
T_{20}	28	0.127	0.131

A. Physical quantities of the theory

The physical quantities that I will focus in in this section are summarized in Table VII. They are (i) vertex functions Γ and $\Gamma^{(2)}$ when one particle is on shell, (ii) the subtracted vertex function $\widehat{\Gamma}_{\rm BS}$ for *both* nucleons off shell, and (iii) the new off-shell nucleon form factors F_3 and F_4 already discussed extensively above. To make the presentation simple, I postpone all precise definitions until Appendix A.

B. Study of the isoscalar interaction currents

The isoscalar interaction currents (IC) produce the interaction current vertex function $\Gamma^{(2)}$ generated by $V^{(2)}$ and giving rise to Fig. 3(A$^{(2)}$), and the subtraction terms $\Gamma^{(1)}$ generated by $V^{(1)}$ and discussed in Ref. I. The behavior of these terms is shown in Fig. 15.

TABLE VI. The χ^2/datum for the prediction of model 2D compared to the published data for A, B, and $\widetilde{T}_{20}$.

$A(Q^2)$	Number	χ^2/d	$T_{20}(Q^2)$	Number	χ^2/d
HEPL-65	5	2.53	Bates-84	2	0.13
Orsay-66	4	1.63	Nuovo-85	2	0.78
CEA-69	18	3.01	Nuovo-90	2	0.83
DESY-71	10	0.71	Bonn-91	1	0.55
SLAC-75	8	1.61	Bates-94	3	2.50
Mainz-81	18	7.36	NIK-96	1	1.02
Bonn-85	5	20.18	NIK-99	3	0.70
Saclay-90	43	2.77	JLabC-00	6	0.86
JLab-A	16	4.59	Nuovo-01	5	3.14
JLab-C	6	2.87	Bates-11	9	0.94
All	131	3.98	All	34	1.29
$A(Q^2)$ ranges			$B(Q^2)$		
$Q \leqslant 0.6$ GeV	64	3.82	Stan-65	4	1.08
$Q > 0.6$ GeV	67	4.14	Mainz-81	4	2.87
3 largest	3	21.83	Saclay-85	13	0.75
			Bonn-85	5	1.07
			JLab-89	6	2.06
			SLAC-90	9	2.28
			All	41	1.56

TABLE VII. Physical quantities that enter into a calculation of the deuteron form factors.

$\Gamma = S^{-1}\Psi$	Relativistic vertex function (with particle 1 on shell); contributes to all diagrams shown in Fig. 3; solution of a two-nucleon CST equation using the OBE kernel
$\Gamma^{(2)} = S^{-1}\Psi^{(2)}$	Relativistic vertex function (with particle 1 on shell); generated by interaction currents of type $V^{(2)}$ which arise from the momentum dependence of the boson couplings to particle 2; calculated by iterating the CST equation once using the kernel $V^{(2)}$; Fig. 3(A$^{(2)}$)
$\widehat{\Gamma}_{\rm BS} = \Gamma_{\rm BS} - \Gamma^{(1)}$	Subtracted vertex function (with *both* particles off shell); the $\Gamma^{(1)}$ subtraction arises from interaction currents $V^{(1)}$ coming from the momentum dependence of the boson couplings to particle 1; calculated by iterating the CST equation once using the subtracted kernel $V - V^{(1)}$ with *both* particles off-shell in the final state; Fig. 3(B)
F_3 and F_4	Form factors describing the off-shell nucleon current; Fig. 3(A)

Figure 15 shows that both IC's make significant contributions to G_C, even at low Q. For the other form factors, G_M and G_Q, their contributions are quite small at low Q, but are still important for $Q \gtrsim 0.5$ GeV (for G_M) and $Q \gtrsim 1$ GeV (for G_Q). These interaction currents are a significant part to the overall theoretical picture.

C. Off-shell effects

What are off-shell effects? This discussion must be approached carefully or serous misunderstandings may emerge. For example, in the CST one nucleon is always off shell in intermediate states; this is the way, the CST creates virtual intermediate states and, at the same time, preserves four-momentum conservation. In conventional quantum mechanics, the particles are always on shell, but the virtual intermediate states do not conserve the total energy of the particles. It can be shown that these two approaches are largely equivalent, with the CST having the advantage that it is relativistically covariant, and the disadvantage that it must learn how to describe off-shell particles (with their accompanying antiparticle components). In the context of the discussion of *NN* scattering, for example, the role of the virtual antiparticles is an interesting off-shell effect. However, in the context of *ed* scattering, I will look only at new effects that did not already arise in *NN* scattering.

The unique off-shell effects that are studied here are the contributions that arise when *both* nucleons are off shell. These are the contributions from the vertex functions $\widehat{\Gamma}_{\rm BS}$, which take us outside the usual boundaries of the CST. The need to discuss the physics of two nucleons off shell does not arise in the discussion of three-nucleon scattering [16,58–60] but does arise in the discussion of *ed* scattering and electron-triton scattering [61,62]. How should these effects be defined so that they give us useful insight into the physics of this theory?

Only Fig. 3(B) requires particle 1 to be driven off shell. In the Breit frame, $P_\pm = \{D_0, \pm\frac{1}{2}q_z\}$, with $q_z = Q$. When the incoming (outgoing) particle 1 is on shell, the outgoing (incoming) particle 1 will have four-momentum

$$\tilde{k}_\pm = \left\{\tilde{E}_\mp, \tilde{\mathbf{k}} \pm \tfrac{1}{2}q_z\right\}, \tag{3.1}$$

where

$$\tilde{E}_\pm = \sqrt{m^2 + \left(\tilde{\mathbf{k}} \pm \tfrac{1}{2}q_z\right)^2}. \tag{3.2}$$

This particle is off shell with an energy $\tilde{k}_0^\pm = \tilde{E}_\mp \neq \tilde{E}_\pm$. I find it convenient to describe this extra degree of freedom by the parameter x_{10}, which is defined as the ratio of the off-shell

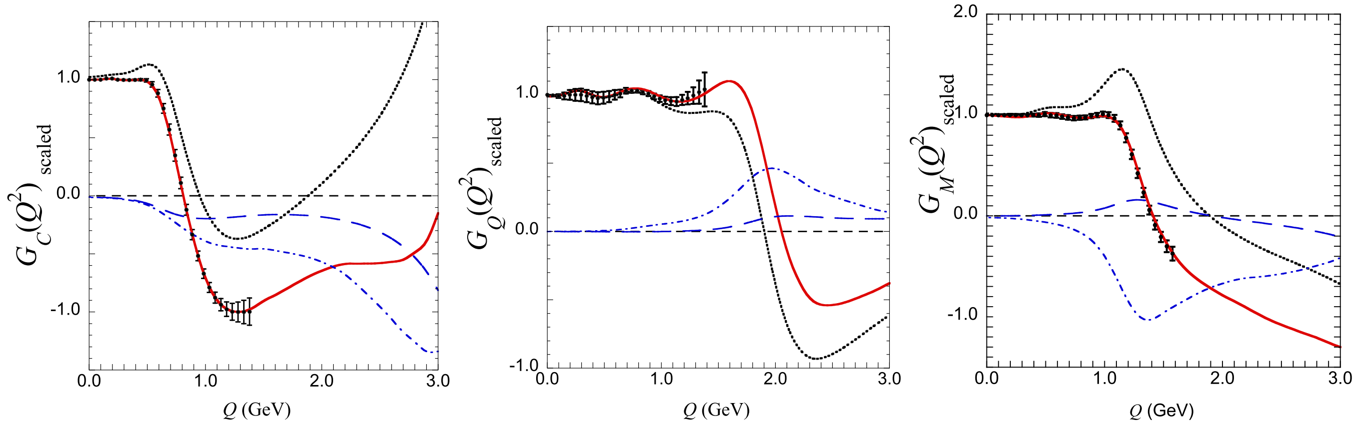

FIG. 15. Study of the two interaction currents, $V^{(2)}$ (blue dot-dashed line) and $V^{(1)}$ (blue long-dashed line). Setting both to zero gives model 2D with no IC (thick black dotted line), while restoring both gives the full model 2D (thick red line) shown in previous figures.

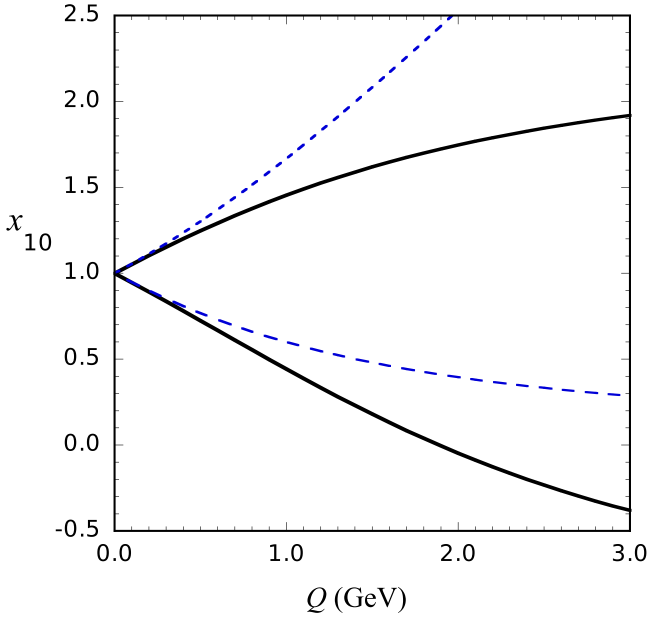

FIG. 16. Plot of the maximum and minimum of x_{10} as a function of Q. The black solid lines show the maximum and minimum, including boost effects, as obtained from Eq. (A31); the blue dashed lines are the maximum and minimum without boost effects as obtained from Eq. (3.4).

energy to the on-shell energy. In this case, the ratio is

$$x_{10}^{\pm} = \frac{\tilde{k}_0^{\pm}}{\tilde{E}_{\pm}} \to \frac{\tilde{E}_{\mp}}{\tilde{E}_{\pm}} = \sqrt{\frac{E_{\tilde{k}}^2 \mp \tilde{k}_z Q + \frac{1}{4}Q^2}{E_{\tilde{k}}^2 \pm \tilde{k}_z Q + \frac{1}{4}Q^2}} \equiv \zeta^{\pm}, \tag{3.3}$$

which is always positive. The maximum of x_{10}^- (x_{10}^+) occurs when $\tilde{k}_z = \tilde{k}$ (or $-\tilde{k}$), $\tilde{k} = k_{\rm max}$, and solving for $k_{\rm max}$ gives

$$\begin{aligned} x_{10}^{\rm max} &= \sqrt{\frac{m^2 + \left(k_{\rm max} + \frac{1}{2}Q\right)^2}{m^2 + \left(k_{\rm max} - \frac{1}{2}Q\right)^2}} \\ &\to \frac{1}{2m}\left(\sqrt{4m^2 + Q^2} + Q\right), \end{aligned} \tag{3.4}$$

and the minimum is $1/x_{10}^{\rm max}$. This shows that as Q increases, the particle 1 (either incoming or outgoing) is forced further and further off shell.

While this gives some insight, what one really wants is the result in the *rest* system of the deuteron, so (3.4) must be transformed to the rest system. This is discussed in detail in Appendix A 3. The results for both (3.4) and the relativistically correct result $X_{10}^{\pm{\rm max}}$, given in Eq. (A31), are shown in Fig. 16. Note that the boost effects are significant.

The invariants that describe $\widehat{\Gamma}_{\rm BS}$ depend on the two variables k and x_{10} (with $x_{10} = 1$ when particle 1 is on shell). As shown in Fig. 16, for studies of the form factor below $Q \simeq 3$, it is sufficient to know the off-shell dependence of the invariants that describe $\widehat{\Gamma}_{\rm BS}$ in the range $1.9 \gtrsim x_{10} \gtrsim -0.3$. This behavior is shown in Fig. 17, with u_v and w_v related to the largest deuteron wave functions u and w by

$$\begin{aligned} u_v(k, x_{10}) &= [(1 + x_{10})E_k - m_d]u(k, x_{10}), \\ w_v(k, x_{10}) &= [(1 - x_{10})E_k - m_d]w(k, x_{10}). \end{aligned} \tag{3.5}$$

The other wave functions are much smaller.

To obtain the off-shell behavior, the wave functions are iterated once using the fully off-shell kernel, as shown in Eq. (A12b). I found that the resulting wave functions were much smother at low momentum if the small one-photon

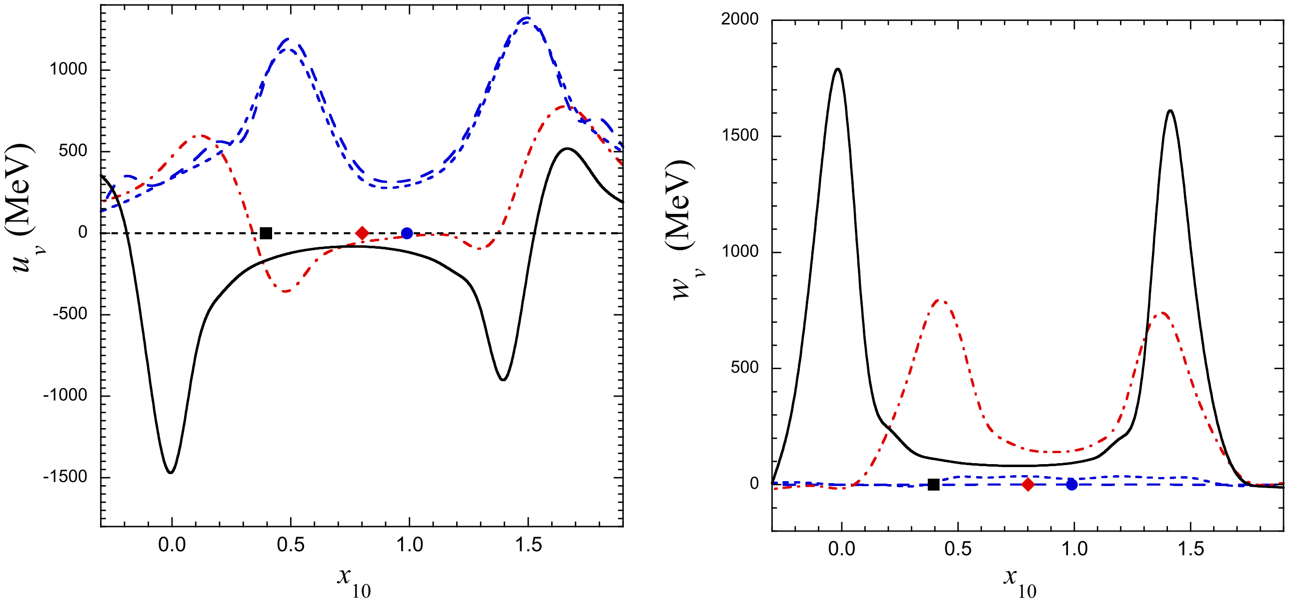

FIG. 17. The invariants u_v and w_v defined in Eq. (3.5) for the favored model WJC2, shown as a function of x_{10} for four fixed momenta: $k = k(1) \simeq 0.527$ MeV (blue long-dashed lines), $k = k(10) \simeq 84.0$ MeV (blue short-dashed lines), $k = k(23) \simeq 450.3$ MeV (red dot-dashed line), and $k = k(32) \simeq 960.8$ MeV (black solid line), where $k(n)$ is the nth Gauss point in the mapped grid of 60 points. The values of x_{10} when particle 2 is on shell are shown for $k(10)$ (solid blue circle), $k(23)$ (solid red diamond), and $k(32)$ (solid black square).

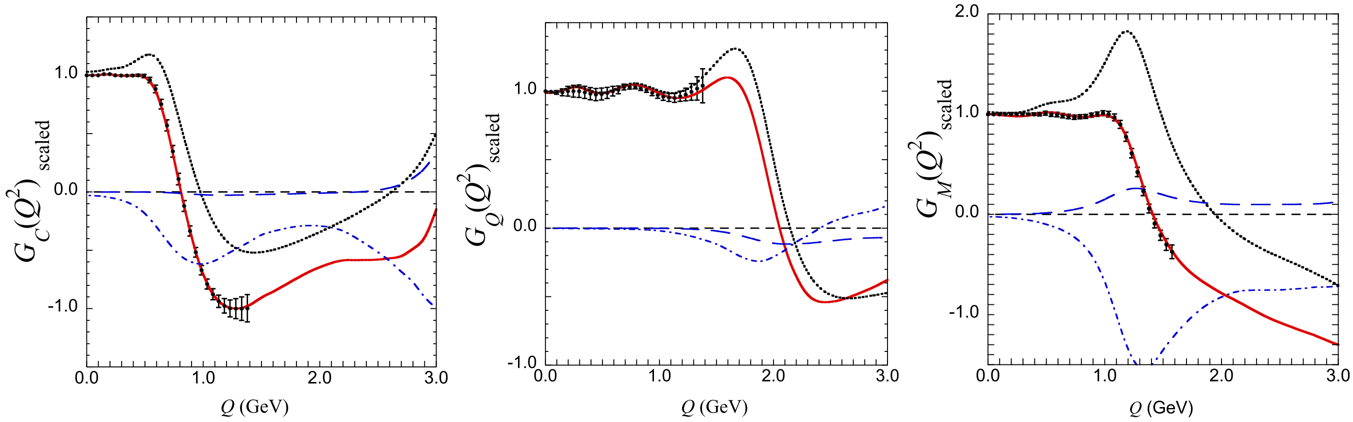

FIG. 18. Study of the off-shell effects defined in the text.

exchange term was removed from the iterating kernel, and all of the results presented in this paper were calculated in this way. This is partly justified by the observation that keeping the "last" one-photon exchange could be regarded as including one higher order effect in α_γ, while ignoring others, and may not even be consistent. In any case, it introduces a small inconsistency: When the on-shell wave functions are iterated without the last one-photon exchange, the normalization is changed slightly. To obtain the original normalization, the results for WJC1 are multiplied by 0.9962 and those for WJC2 by 0.9954.

The point on the curves where particle 2 is on shell is given by

$$x_{10}^{\rm ex}(k)=\frac{m_d-E_k}{E_k}, \tag{3.6}$$

which depends on k. This point is marked by the small solid black squares (for $k = 960.8$ MeV), red diamonds ($k = 450.3$ MeV), and blue circles ($k = 84$ MeV) along the x axis in the panels of Fig. 17. These points are interesting because the two-body *NN* bound state equation depends on vertex functions defined only at $x_{10} = 1$ and $x_{10} = x_{10}^{\rm ex}(k)$; values of the vertex functions at all other values of x_{10} have not played *any* role in previous fits to the *NN* data. The off-shell dependence of elastic *ed* scattering depends on values of the vertex functions determined theoretically, but *never tested experimentally*.

The size of these effects is shown in Fig. 18. In each panel, the black dotted line is a calculation using the parameters of model 2D with $x_{10} = 1$ in the (B) diagrams, and the thick red solid line is the full model 2D with x_{10} free to vary as the kinematics dictates (as shown previously). The contribution from Fig. 3(B) decomposes into a contribution multiplied by the projector $\Theta(-k)$ that vanishes when particle 1 is on shell (referred to as the C contribution) and a remainder (referred to as the B contribution, distinguished from the total (B) contribution by the absence of the parentheses):

$$\underbrace{\widehat{\Gamma}_{\rm BS}(k,P)}_{\rm (B)}=\underbrace{\Gamma(k,P)}_{\rm B}-\underbrace{\Gamma_{\rm off}(k,P)\,2\Theta(-k)}_{\rm C}, \tag{3.7}$$

The C contribution (labeled by the blue long-dashed lines in the figure) is quite small but still of great interest because it depends on invariants that do not exist when one of the particles is on shell. The largest off-shell contributions come from the B terms (dash-dotted blue lines), which make a significant contribution to all the form factors, especially G_C and G_M.

The calculations are sensitive to off-shell effects at all values of Q.

D. Size of the F_3 and F_4 contributions

The size of the F_3 and F_4 contributions was addressed in Fig. 14; Fig. 19 shows these effects in more detail. Both F_3 and F_4 make comparable contributions. It is interesting to note that the F_4 contribution plays a very important role in correcting the failure of model 2A at low Q. In this case, the F_3 and F_4 contributions are individually quite large and tend to cancel each other.

E. Accuracy of the RIA

In the absence of isoscalar interaction currents, the relativistic impulse approximation (RIA) was originally defined to be twice the contribution from Fig. 3(A). The interest in this approximation arose from the idea that symmetry (the CST equations are explicitly symmetrized to ensure that *NN* scattering satisfies the generalized Pauli principle exactly) should allow one to get the full result from the electromagnetic scattering from only one of the nucleons (multiplied by a factor of 2). If this were true, after adding interaction currents the results from Figs. 3(A)+ 3(A$^{(2)}$) should equal the results from Fig. 3(B), so that the full result would come from either of these alone, or their average, which emerges if one takes 1/2 the sum of the contributions from the lower and upper half plane.

The contributions from Figs. 3(A)+ 3(A$^{(2)}$) and 3(B) are compared in Fig. 20. The contributions from Fig. 3(B) is given in two parts: the B and C contributions discussed in Eq. (3.7). The figure shows the total (B) contribution (labeled with the blue long dashed line) and the B part of this contribution (labeled with the blue dot-dashed line); the C part can be inferred from the difference of these two. The average of the two long dashed lines (black and blue) is the total result for model 2D.

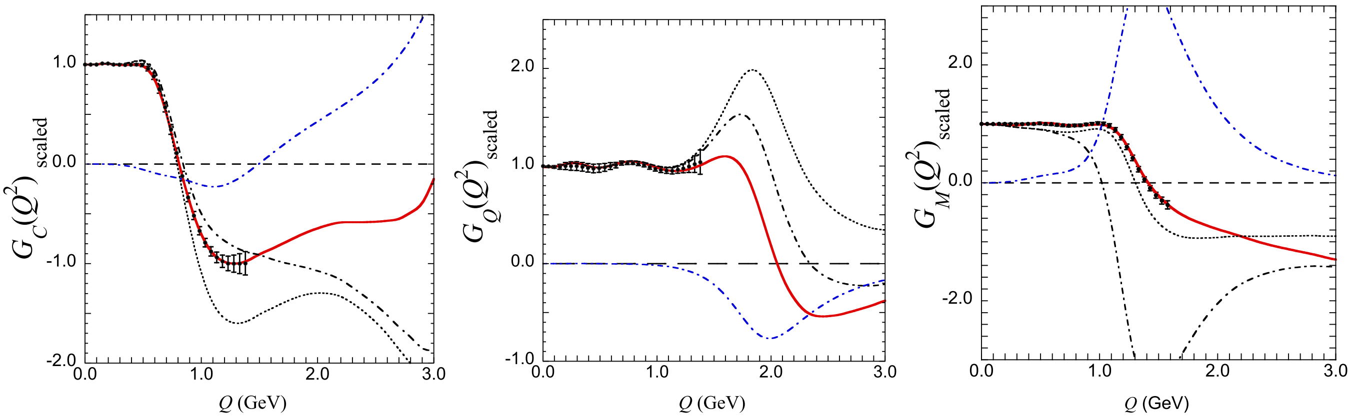

FIG. 19. Study of the sensitivity of the form factors F_3 and F_4. *All* curves use the predicted CST1 for G_{En}. Both black curves set $F_4 = 0$ and $F_3 \neq 0$: The black dotted curves use a dipole form for F_3 while the black dot-dashed lines uses model $F_3(2)$. The heavy red line is the result of adding the contributions from $F_4(2)$ to the black dot-dashed lines and gives the best model 2D. The blue dot-dashed lines, which show the size of the $F_4(2)$ contributions by themselves, are given for reference.

I conclude from this figure that the RIA disagrees with the magnetic form factor even at low Q, but that it works reasonably well at low momentum transfer for the two charge form factors. In any case, it is not good enough to be a replacement for the full theory, as was hoped at one time.

IV. RELATIVISTIC EFFECTS

Some in the electron scattering community still believe that relativistic effects are small in electron deuteron scattering and that it is possible to use deuteron wave functions calculated from the Schrödinger equation to study *ed* elastic scattering. Casper and I argued more than 50 years ago [63] that relativistic corrections were important when using deuteron scattering data to draw precise conclusions, and in this section I will review this issue in detail.

I focus only on the observables G_C and A at small Q^2, where it might be assumed that a nonrelativistic calculation would be reliable. The nonrelativistic theory for G_C gives

$$\begin{aligned} G_C^{\rm NR}(Q^2) &= \int_0^\infty dr[u^2(r)+w^2(r)]j_0(\tau_0) \\ &= \frac{1}{2}\int_0^\infty k^2dk\int_{-1}^{1} dz[u(k_+)u(k_-) \\ &\quad + P_2(\hat{\mathbf{k}}_+\cdot\hat{\mathbf{k}}_-)w(k_+)w(k_-)], \end{aligned} \tag{4.1}$$

where $\tau_0 = \frac{1}{2}rQ$, u and w are the S and D state wave functions, and

$$\begin{aligned} \mathbf{k}_\pm &= \mathbf{k} \pm \frac{1}{4}\mathbf{q}, \quad k_\pm^2 = k^2 \pm \frac{1}{2}z\,kQ + \frac{Q^2}{16}, \\ \hat{\mathbf{k}}_+\cdot\hat{\mathbf{k}}_- &= \frac{16k^2-Q^2}{16k_+k_-}. \end{aligned} \tag{4.2}$$

[Beware that the $\mathbf{k}_\pm$ defined above differs significantly from the $\tilde{\mathbf{k}}_\pm$ defined in Eq. (3.1).] This momentum space nonrelativistic result emerges naturally from the nonrelativistic limit of the CIT. I emphasize that the emergence of the nonrelativistic limit is a *very general* feature of this theory and

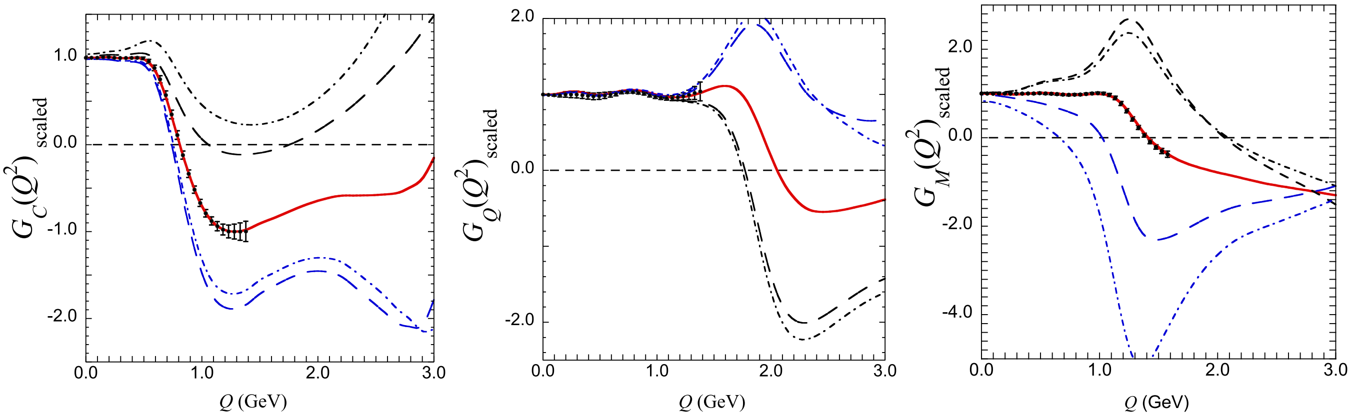

FIG. 20. Study of the validity of the RIA. Contributions from Fig. 3(A) (black dot-dashed line) and 3(A) + 3(A^2) (black long dashed line) are compared to the contributions from 3(B) (blue long dashed line). The difference between the two blue lines is the C contribution to $\Gamma_{\rm BS}$, defined in Eq. (3.7). The heavy solid red line is model 2D as shown in previous figures.

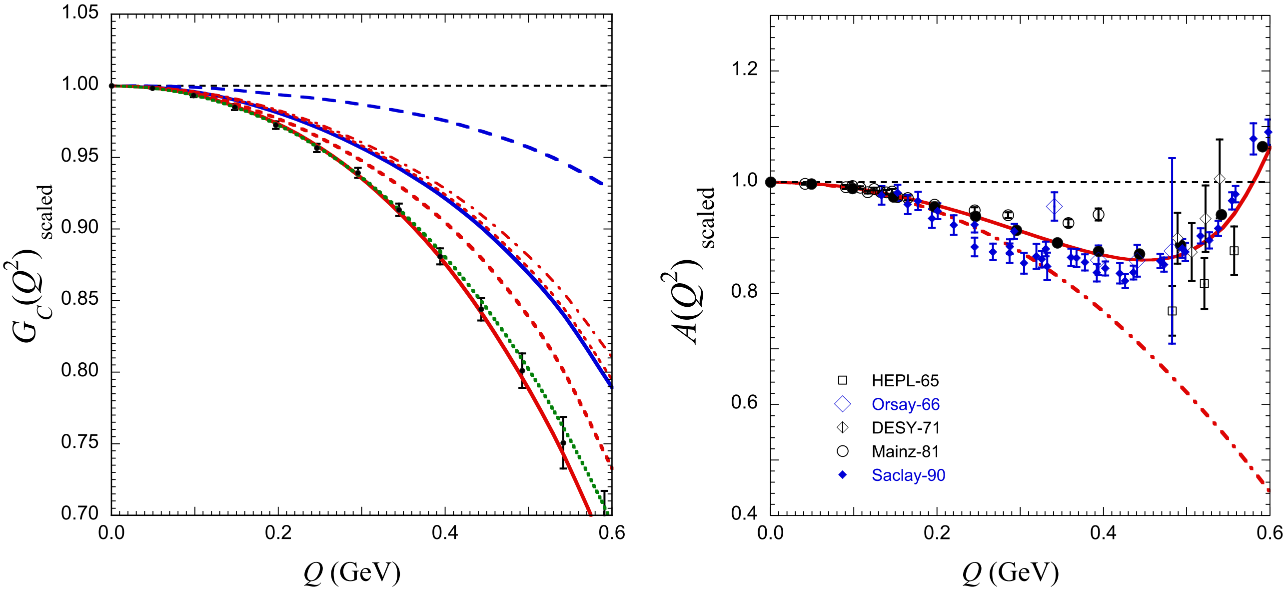

FIG. 21. Study of relativistic effects. The left panel is scaled by $G_C^{\rm NR}$ given in Eq. (4.1); the right panel is scaled by $(G_C^{\rm NR})^2$. In both panels, the small black dots are the Sick GA (with error bars) and the thick sold red lines are the predictions for model 2D. The other curves are discussed in the text.

provides an excellent starting point for the study of relativistic effects. To get the right limits, one must be very careful to use the correct nonrelativistic transformations: argument shift (A13c) for the (A) diagram and A21 for the (B) diagram. Both the (A) and (B) diagrams give exactly the same nonrelativistic limit, a limit where the RIA is accurate.

The size of various contributions, *scaled* by the nonrelativistic expression (4.1), is shown in the left panel of Fig. 21. The blue dashed line replaces the nonrelativistic argument shifts that appear in (4.1), and were derived in (A13c), with the fully relativistic ones (A13b). Note that this effect alone accounts for about a 4% correction at $Q \simeq 0.4$ GeV, about eight times the size of the error in the Sick GA. The blue solid line shows the result obtained from the full calculation of G_C if only u and w wave functions are included. At $Q \simeq 0.4$, this produces a discrepancy of almost 10% with the nonrelativistic calculation. All changes after this begin to go beyond relativistic kinematics. Adding the v_t and v_s terms moves the result to the red dot-dashed line, and adding the C contributions from the (B) diagram moves the total to the red short-dashed line, both small effects. A bigger change occurs when I add the A(2) diagram and all contributions from the F_2 nucleon form factor, which brings the result to the red longer-dashed line. Finally adding the contributions from the off-shell form factors F_3 and F_4 brings one to the final result for model 2D, the heavy solid red line. The green short-dashed line is the function

$$G_C^{\rm fit} = 1 - \frac{Q^2}{1.5} - \frac{Q^4}{2}, \tag{4.3}$$

which gives a rough estimate of the size of all of the effects.

The size of the relativistic argument shift alone is about four times smaller than the total shift, or about $Q^2/6$, comparable to the result $Q^2/8$ that Casper and I found more than 50 years ago. For comparison, the recoil effect of the deuteron itself is very much smaller

$$\frac{1}{D_0} = 1 - \frac{Q^2}{8m_d^2} \simeq 1 - \frac{Q^2}{32}. \tag{4.4}$$

Because the kinematics and the relativistic shifts in the arguments of the wave functions (that add up to the solid blue line in Fig. 21) can explain only about 1/2 of the total shift, it is clear that an accurate theoretical interpretation of the data requires the use of a relativistic theory, even at the smallest values of Q^2.

The right panel of Fig. 21 shows theory and data for the structure function A, all scaled by $(G_C^{\rm NR})^2$. The red dot-dashed line is G_C^2 of model 2D while the thick solid line is the full calculation of A using all form factors from model 2D. The panel shows that the other contributions to A coming from G_M^2 and G_Q^2 begin to become important at $Q \gtrsim 0.2$ GeV.

V. THE STATIC MOMENTS

The form factors at $Q^2 = 0$ give the charge, magnetic, and quadrupole moments in units reported in Eq. (A4). Using the exact equations, there is no need to expand the analytic results around $Q^2 = 0$ as I did in Refs. II and III. However, comparison of the two different calculations uncovered some errors in Ref. II, and I now find that the new value for the magnetic moment predicted by model WJC2 is in precise agreement with the measured result. In addition, the new, more accurate values of the quadrupole moment differ from the experimental values by more than 1%, with no significant difference between the predictions of the two models, in disagreement with the conclusions of Ref. III.

Various contributions to the static moments are defined in Table VIII. Here, in order to provide details that may be of use to future investigators, I also report some contributions that I did not study in the previous references. Tables IX–XI

TABLE VIII. Separate contributions to the deuteron static moments from the diagrams shown in Fig. 3.

A	Total from diagram (A) with full f_{00}, g_{00} given in Eq. (1.16)
A_0	Diagram (A) with $f_{00} = 1$, $g_{00} = 0$
$\mathrm{A} - \mathrm{A}_0$	Total h dependence from diagram (A)
A_2	Diagram ($\mathrm{A}^{(2)}$), calculated using Eq. (A12a) with the interaction $V^{(2)}$
B, C	The two parts of diagram (B) [the B and C terms in the decomposition (3.7)] with $\widehat{\Gamma}_{BS}$ calculated using Eq. (A12b)
B_0, C_0	The two parts of diagram (B) with k_0 fixed at E_k in $\widehat{\Gamma}_{BS}$, but not in $h(p)$
B_h, C_h	The dependence of $h(p)$ on $k_0 - E_k$ in the two parts of diagram (B)
$\mathrm{B}_0 - \mathrm{B}_h$, $\mathrm{C}_0 - \mathrm{C}_h$	Removes the dependence of $h(p)$ on $k_0 - E_k$ from B_0 and C_0, leaving $k_0 = E_k$ everywhere (on shell)
On shell	$\mathrm{A}_0 + \mathrm{B}_0 - \mathrm{B}_h + \mathrm{C}_0 - \mathrm{C}_h$; z_ℓ^2 terms of Ref. [2], or 0.286 $(1+Q_{\rm NR}^{\Delta} + Q_{\rm Rc} + Q_P + Q_\chi)$ of Ref. [3]
h	$\mathrm{A} - \mathrm{A}_0 + \mathrm{B}_h + \mathrm{C}_h$; $a_\ell z_\ell^2$ terms of Ref. [2], or 0.286 $Q_{h'}$ of Ref. [3]
$V^{(2)}$	A_2; $z_\ell z_\ell^{(2)}$ terms of Ref. [2], or 0.286 Q_{V_2} of Ref. [3]
Off shell	$\mathrm{B} - \mathrm{B}_0 + \mathrm{C} - \mathrm{C}_0$; $z_\ell \widehat{z}_\ell$ terms of Ref. [2], or 0.286 $(Q_{V_1} + Q_{\rm int})$ of Ref. [3] (includes the $V^{(1)}$ current)
Total	$\mathrm{A}+\mathrm{A}^{(2)}+\mathrm{B}+\mathrm{C}$

compare the results obtained from the exact form factors with the results obtained from the approximate expansions reported in Refs. II and III (and for the magnetic moment, in Appendix G).

A. Charge and magnetic moment

In Ref. II, I conjectured that the errors in the expansions should be about 0.002. As shown in Table IX, the calculations of the charge agree to better than this, but the magnetic moment presents a more complicated picture. I originally found such large disagreements with the expansions for the magnetic moment reported in Ref. II that I redid them and found the corrected results given in Appendix G. Table X shows that the new expansion disagrees with the exact results by about 0.002 for several terms but there are discrepancies as large as 0.007 (0.7%) with others. I believe that the major source of this discrepancy is the expansion of the nucleon kinetic energy

$$\frac{E_k}{m} \simeq 1 + \frac{k^2}{2m^2} - \frac{k^4}{8m^4} + \cdots . \tag{5.1}$$

Since k^4 terms were dropped, the discrepancy could be as large as 0.007 if the terms conspire to make the coefficient of the k^4 term of the order of unity (and not 1/8) and the mean momentum of the nucleon is about 300 MeV. In any case, the expansions are not as reliable as I expected. The remarkable new result is that the magnetic moment for model WJC2 is in very good agreement with experiment, differing by only 0.07%.

TABLE IX. The contributions to the deuteron charge (or normalization). Since $\mathrm{C}_h = 0$, it is not shown.

	WJC1		WJC2	
Quantity	1B	Ref. [2]	2D	Ref. [2]
On shell ($k_0 = E_k$)	1.0547	1.055	1.0231	1.023
h dependence	0.0245	0.025	0.0176	0.018
$V^{(2)}$ current	−0.0228	−0.023	−0.0111	−0.011
Off shell ($k_0 \neq E_k$)	−0.0562	−0.057	−0.0297	−0.030
Total	1.0002	1.000	1.0000	1.000
2 × A_0	1.0547	1.055	1.0231	1.023
2× $(\mathrm{A} - \mathrm{A}_0)$	0.0245	0.025	0.0176	0.018
2× B	0.9693		0.9835	
2× C	−0.0025		−0.0021	
2 × B_0	1.0816		1.0428	
2 × C_0	−0.0025		−0.0021	
2 × B_h	0.0245	0.025	0.0176	0.018

B. Quadrupole moment

The comparison of the quadrupole moment with the expansions reported in Ref. III does not fare much better. Here I originally estimated the error to be about 0.2% or a δQ of 0.0006, and a comparison with Table XI shows that this seems to be accurate for the small terms but fails for the largest terms

TABLE X. The contributions to the deuteron magnetic moment, $\mu_d = mG_M(0)/m_d$ (in nuclear magnetons). The experimental value is 0.8574.

	WJC1		WJC2	
Quantity	1B	App G	2D	App G
On shell ($k_0 = E_k$)	0.8985	0.8812	0.8643	0.8630
h dependence	0.0123	0.0145	0.0112	0.0092
$V^{(2)}$ current	−0.0156	−0.0167	0.0004	0.0000
Off shell ($k_0 \neq E_k$)	−0.0289	−0.0170	−0.0180	−0.0129
Total	0.8663	0.8620	0.8580	0.8594
Error	0.0089	0.0046	0.0006	0.0020
Error (%)	1.04%	0.48%	0.07%	0.23%
2 × A_0	0.9155		0.8646	
2× $(\mathrm{A} - \mathrm{A}_0)$	0.0141		0.0158	
2× B	0.7193		0.7163	
2× C	0.1150		−0.1183	
2 × B_0	0.7904		0.7553	
2 × C_0	0.1017		0.1154	
2 × B_h	0.0145		0.0093	
2 × C_h	−0.0039		−0.0026	

TABLE XI. The contributions to the deuteron quadrupole moment $Q_d = m_d^2 G_Q(0)$ (in fm^{-2}). The experimental value is 0.2859(6).

	WJC1		WJC2	
Quantity	1B	Ref. [3]	2D	Ref. [3]
On shell ($k_0 = E_k$)	0.2831	0.285	0.2815	0.284
h dependence	0.0011	0.000	0.0007	0.000
$V^{(2)}$ current	−0.0009	−0.001	−0.0002	0.000
Off shell $k_0 \neq E_k$	−0.0014	−0.005	−0.0003	0.000
Total	0.2820	0.279	0.2817	0.284
Error	−0.0039	−0.007	−0.0042	−0.0019
Error (%)	− 1.38%	−2.4%	−1.49%	−0.7%
2 × A$_0$	0.2825		0.2815	
2× (A − A$_0$)	0.0014		0.0008	
2× B	0.2835		0.2829	
2× C	−0.0017		−0.0016	
2 × B$_0$	0.2863		0.2836	
2 × C$_0$	−0.0017		−0.0016	
2 × B$_h$	0.0009		0.0006	
2 × C$_h$	−0.0001		−0.0000	

with an error of about 0.002, or about 1% (similar to that found for the magnetic moment). However, since all terms seem to have similar signs and magnitudes, there is no reason to expect an error in the expansion as I did for the magnetic moment, and I did not recalculate the expansions given in Ref. III. The new conclusion here is that the two models have similar quadrupole moments, differing by about 1.5% from the experimental result.

C. Rms radius

The rms radius of the deuteron is, by definition,

$$R_{\rm rms}^2 = -6\frac{d}{dQ^2}G_C(Q^2). \tag{5.2}$$

The values of $R_{\rm rms}^2$ (in GeV^{-2}) and $R_{\rm rms}$ (in fm) are shown in Table XII. Note that the corrections from the relativistic effects discussed in Sec. IV are very small.

Perhaps it is interesting to see how a linear fit to the Q^2 dependence of the form factor might affect how the radius would be extracted from experimental data. Figure 22 shows four fits, with parameters listed in Table XIII, to a set of theoretical points calculated using model 2D. The large variation in the derivative, c_2, shows how difficult it is to get the slope at $Q^2 = 0$ from the fits. Using the 10 points seems to be less reliable than the four lowest points, and it is a surprise to me that the quadratic fit to the lowest points, which is completely unreliable at higher Q^2, gives a c_2 closest to the derivative.

TABLE XII. Contributions to the deuteron radius for model 2D. The experimental value of 2.130(10) fm is taken from Ref. [64]. The last row of the table is model 2D with $dG_C/dQ^2 = -19.36$ (GeV)$^{-2}$.

Approximation	$R_{\rm rms}^2$ (GeV)$^{-2}$	$R_{\rm rms}$ fm
NR	116.1	2.122
NR with (A) shift	117.0	2.131
All u, w	116.6	2.128
Add v_t, v_s	116.7	2.128
Add C terms	116.7	2.128
Add A$^{(2)}$ and F_2	116.3	2.124
Add F_3 and F_4	116.2	2.123

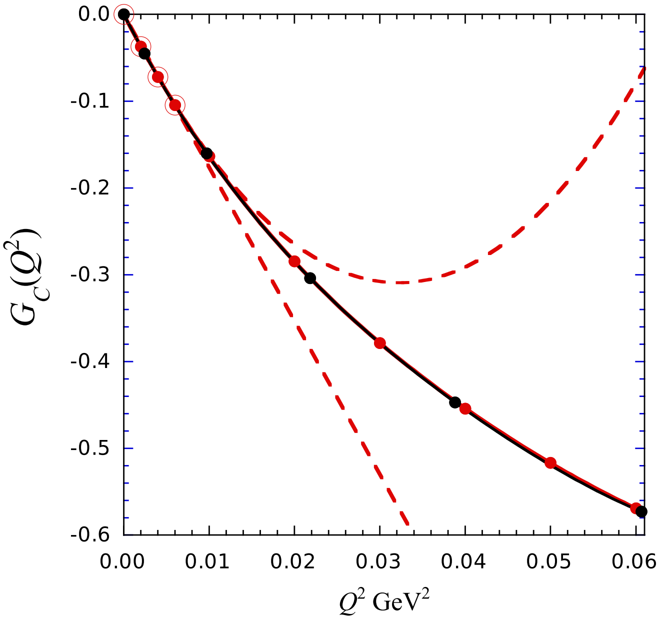

FIG. 22. Study of the dependence of the deuteron charge form factor on Q^2 at very small Q^2. The two red dashed lines are linear and quadratic fits to the lowest four points represented by red dots surrounded by a red circle, all at $Q^2 < 0.01$. The solid black lines are (indistinguishable) quadratic and cubic fits to all the red dots, including 6 beyond beyond $Q^2 = 0.01$. The black dots are the Sick GA.

VI. CONCLUSIONS AND DISCUSSION

A. Major new results

This is the first time the deuteron form factors have been calculated using models WJC1 and WJC2, which give precision fits to the np data base with χ^2/datum ≈1. These models use a kernel with a dependence on the momentum of the off-shell particle and therefore require isoscalar interaction currents in order to conserve the two-body np current. At first, it seems that the existence of these currents would make it impossible to make any unique predictions for the form factors, but I showed in Ref. I that using principles of

TABLE XIII. Fitting parameters for the four curves of the form $f(Q^2) = \sum_{n=1}^{n=3} c_{2n}Q^{2n}$ shown in Fig. 22. Recall that direct calculation of the derivative gave $c_2 = -19.36$.

	4 points	4 points	10 points	10 points
c_2	−17.667	−19.202	−15.701	−18.318
c_4	0	293.13	106.05	229.76
c_6	0	0	0	−1372.6

simplicity and *picture independence* it is possible to all but uniquely fix these currents in terms of the already determined parameters of the *np* models. These results fixed the currents at $Q^2 = 0$, and I show here that the exact calculations of the static moments of the deuteron, calculated without adjustable parameters (assuming $F_4(0) = 0$), give very good predictions. [If $F_4(0) \neq 0$, its effect on the magnetic moment is much larger than the quadrupole moment, justifying the choice $F_4(0) = 0$.]

In addition, I believe that this is the first time anyone has obtained a *precision* fit to all of the deuteron elastic scattering data (where precision in this case also means χ^2/datum $\approx$1). I immediately qualify this remark: Such a fit would be *impossible* without using the global analysis of Ingo Sick. To obtain this global analysis, Sick reanalyzed all for the data for the invariant functions $A(Q^2)$, $B(Q^2)$, and the polarization transfer function $T_{20}(Q^2)$. My fit is actually to the Sick GA; as I have discussed briefly above, direct fits to the published data cannot give such a low χ^2 because the published data are not consistent to this level (recall Table VI). These issues deserved to be reviewed by other scientists.

A third major new result is a *prediction* for the neutron charge form factor, $G_{En}(Q^2)$, in the region $Q^2 \gtrsim 2$ (GeV)^2, where it has not been measured experimentally (see Fig. 12 and model CST1 in Table III).

The last new result I want to highlight is the determination of two new off-shell nucleon form factors $F_3(Q^2)$ and $F_4(Q^2)$, defined in Eqs. (1.13) and (1.14). These new form factors can contribute only when *both* the incoming and the outgoing nucleon is off shell, and thus contribute only to Fig. 3(A), the only one where this is possible. The form factor F_3, known for a long time, cannot be zero because current conservation *requires* $F_3(0) = 1$. Form factor F_4 (new to this paper) is purely transverse and hence cannot be constrained by current conservation in any way. However, *balance* between the on-shell form factors $F_1(Q^2)$ and $F_2(Q^2)$ provides an *ab initio* argument for including F_4 (and excluding others that appear in the most general expansion of the off-shell nucleon current): Since F_3 is required to complement F_1, it is not a stretch to argue that F_4 should be included to complement F_2, even though neither F_2 nor F_4 can be constrained by current conservation. The data will determine these form factors; as it turns out F_2 can be directly measured by electron nucleon scattering, while F_4 can only be measured by electron scattering from a composite nucleus, the deuteron being the simplest.

In this paper, model WJC2 uses the Sick GA at intermediate Q^2 to predict the form factors F_3 and F_4. The data are insensitive to precise values of F_4 at low Q^2 (I assumed $F_4(0) = 0$, a value that would likely emerge from a comparison of the static moments, but not investigated here) and there is insufficient data at $Q^2 \gtrsim 2$ (GeV)^2 for a prediction, so I adjusted fits so that the large Q^2 behavior of these form factors would be small. These introduce small uncertainties which I cannot estimate. The reason for not using the model WJC1 to extract F_3 and F_4 was discussed in Sec. II D.

Table XIV gives numerical values for the 12 model 2D body form factors $D_{X,i}(Q^2)$ introduced in Eq. (1.19). The reader may use these to extract her own nucleon form factors from the data.

B. Assessment

For this assessment, I return to an issue I raised in Ref. I: Can the CST make predictions? Stated more forcefully, if I obtain a precision fit to the *three* independent sets of deuteron data for A, B, and T_{20} by adjusting another set of *three* independent functions F_3, F_4, and G_{En}, in what sense does this provide any understanding? I will discuss this issue in four parts:

(i) First, the independent functions are multiplied by a body form factor and hence are constrained by the values of the body form factor itself, which depends on the *np* dynamics of the WJC models. If the body form factors are small or have the “wrong” sequence of signs for G_C, G_M, G_Q, this will prevent the independent functions from giving a desirable fit to all three form factors.

(ii) Next, the predictions for the static deuteron moments are absolute; they are free of any parameters (because $G_{En}(0)$ and $F_3(0)$ are known, and I constrain $F_4(0) = 0$). The low-Q^2 behavior of A, B, and T_{20} (Figs. 10, 7, and 8, respectively) all show a complete insensitivity to the independent functions for $Q \lesssim 0.5$ GeV. This shows that the CST gives precise predictions for all low Q^2 observables, largely independent of the choice of the independent functions.

(iii) Determination of the three independent functions using model WJC1 gives values of G_{En} that disagree with the data for G_{En} over the entire range of Q^2, as shown in Fig. 12. In this sense, model WJC1 fails, allowing me to conclude that the prediction obtained from model WJC2, which is consistent with the data for G_{En} out to the highest Q point measured ($Q \simeq 1.4$ GeV), is not an accident, but a real success (the body form factors for WJC2 have the correct properties). An experimental confirmation of the prediction for G_{En} at higher Q would be a further success of model WJC2.

(iv) Finally, note that no choice of G_{En} can fit the GA for A at the highest Q^2 points (recall the small circles in Fig. 12). This is either an indication that model WJC2 fails at the highest Q^2, or might be an indication that the GA is inaccurate at the highest points, a possibility suggested by the largest Jefferson Laboratory Hall A measurement for A at $Q^2 \simeq 6$ GeV^2. Further measurements at high Q^2 would clarify this.

C. Alternative interpretation

The central role played by the off-shell form factors F_3 and F_4 leads to the following question: Will the physics described by these form factors disappear in a formalism where the nucleons are always on shell? The answer is “no.” The way the same physics is described in alternative formalisms is shown in Fig. 23, where for shorthand I used $\Phi^\mu = i\sigma^{\mu\nu}q_\nu/(2m)$. The left panel shows, as an example, the case where the one-pion exchange mechanism is the “last” interaction to be factored out of the *NN* iteration kernel, and the right panel shoes how the the projection operators Θ cancel the

TABLE XIV. Body form factors for the model 2D, defined in Table I.

Q	D_{C1}	D_{C2}	D_{C3}	D_{C4}	D_{M1}	D_{M2}	D_{M3}	D_{M4}	D_{Q1}	D_{Q2}	D_{Q3}	D_{Q4}
0.001	1.003	-2.611×10^{-7}	-3.334×10^{-3}	5.43×10^{-10}	1.924	1.793	4.994×10^{-3}	-2.247×10^{-4}	2.548×10^{1}	-4.196×10^{-1}	-2.725×10^{-4}	-1.861×10^{-4}
0.101	8.576×10^{-1}	-2.251×10^{-3}	-3.308×10^{-3}	5.494×10^{-6}	1.654	1.527	4.969×10^{-3}	-2.402×10^{-4}	2.189×10^{1}	-4.555×10^{-1}	-1.918×10^{-4}	-1.809×10^{-4}
0.201	5.988×10^{-1}	-6.042×10^{-3}	-3.232×10^{-3}	2.091×10^{-5}	1.181	1.064	4.869×10^{-3}	-2.844×10^{-4}	1.540×10^{1}	-5.064×10^{-1}	-1.728×10^{-4}	-1.133×10^{-4}
0.301	3.847×10^{-1}	-8.315×10^{-3}	-3.109×10^{-3}	4.496×10^{-5}	7.963×10^{-1}	6.922×10^{-1}	4.727×10^{-3}	-3.554×10^{-4}	1.017×10^{1}	-5.250×10^{-1}	-1.888×10^{-4}	-7.917×10^{-5}
0.401	2.354×10^{-1}	-8.443×10^{-3}	-2.945×10^{-3}	7.496×10^{-5}	5.297×10^{-1}	4.401×10^{-1}	4.537×10^{-3}	-4.483×10^{-4}	6.642	-5.094×10^{-1}	-1.921×10^{-4}	-3.139×10^{-5}
0.501	1.356×10^{-1}	-6.803×10^{-3}	-2.745×10^{-3}	1.078×10^{-4}	3.511×10^{-1}	2.759×10^{-1}	4.299×10^{-3}	-5.575×10^{-4}	4.369	-4.710×10^{-1}	-1.559×10^{-4}	2.607×10^{-5}
0.601	6.999×10^{-2}	-4.005×10^{-3}	-2.517×10^{-3}	1.399×10^{-4}	2.314×10^{-1}	1.696×10^{-1}	4.026×10^{-3}	-6.759×10^{-4}	2.905	-4.214×10^{-1}	-1.329×10^{-4}	9.206×10^{-5}
0.701	2.753×10^{-2}	-6.161×10^{-4}	-2.271×10^{-3}	1.677×10^{-4}	1.509×10^{-1}	1.010×10^{-1}	3.723×10^{-3}	-7.969×10^{-4}	1.954	-3.686×10^{-1}	-9.700×10^{-5}	1.655×10^{-4}
0.801	4.582×10^{-4}	2.934×10^{-3}	-2.014×10^{-3}	1.878×10^{-4}	9.615×10^{-2}	5.674×10^{-2}	3.401×10^{-3}	-9.133×10^{-4}	1.330	-3.179×10^{-1}	-5.520×10^{-5}	2.439×10^{-4}
0.901	-1.602×10^{-2}	6.331×10^{-3}	-1.755×10^{-3}	1.975×10^{-4}	5.867×10^{-2}	2.803×10^{-2}	3.068×10^{-3}	-1.018×10^{-3}	9.156×10^{-1}	-2.720×10^{-1}	-2.272×10^{-6}	3.232×10^{-4}
1.001	-2.542×10^{-2}	9.380×10^{-3}	-1.503×10^{-3}	1.946×10^{-4}	3.276×10^{-2}	9.419×10^{-3}	2.735×10^{-3}	-1.105×10^{-3}	6.341×10^{-1}	-2.314×10^{-1}	5.797×10^{-5}	4.029×10^{-4}
1.101	-2.979×10^{-2}	1.191×10^{-2}	-1.264×10^{-3}	1.783×10^{-4}	1.502×10^{-2}	-2.510×10^{-3}	2.410×10^{-3}	-1.171×10^{-3}	4.398×10^{-1}	-1.962×10^{-1}	1.235×10^{-4}	4.774×10^{-4}
1.201	-3.084×10^{-2}	1.384×10^{-2}	-1.043×10^{-3}	1.485×10^{-4}	3.259×10^{-3}	-9.659×10^{-3}	2.100×10^{-3}	-1.213×10^{-3}	3.051×10^{-1}	-1.657×10^{-1}	1.914×10^{-4}	5.447×10^{-4}
1.301	-2.998×10^{-2}	1.518×10^{-2}	-8.456×10^{-4}	1.066×10^{-4}	-4.328×10^{-3}	-1.347×10^{-2}	1.812×10^{-3}	-1.229×10^{-3}	2.110×10^{-1}	-1.393×10^{-1}	2.594×10^{-4}	6.032×10^{-4}
1.401	-2.780×10^{-2}	1.591×10^{-2}	-6.730×10^{-4}	5.441×10^{-5}	-8.879×10^{-3}	-1.509×10^{-2}	1.550×10^{-3}	-1.220×10^{-3}	1.457×10^{-1}	-1.169×10^{-1}	3.250×10^{-4}	6.477×10^{-4}
1.501	-2.479×10^{-2}	1.610×10^{-2}	-5.266×10^{-4}	-5.290×10^{-6}	-1.119×10^{-2}	-1.529×10^{-2}	1.317×10^{-3}	-1.189×10^{-3}	1.004×10^{-1}	-9.791×10^{-2}	3.850×10^{-4}	6.793×10^{-4}
1.601	-2.191×10^{-2}	1.591×10^{-2}	-4.047×10^{-4}	-6.941×10^{-5}	-1.229×10^{-2}	-1.462×10^{-2}	1.114×10^{-3}	-1.136×10^{-3}	6.860×10^{-2}	-8.194×10^{-2}	4.353×10^{-4}	6.964×10^{-4}
1.701	-1.899×10^{-2}	1.538×10^{-2}	-3.066×10^{-4}	-1.348×10^{-4}	-1.255×10^{-2}	-1.351×10^{-2}	9.400×10^{-4}	-1.068×10^{-3}	4.652×10^{-2}	-6.873×10^{-2}	4.755×10^{-4}	6.988×10^{-4}
1.801	-1.622×10^{-2}	1.457×10^{-2}	-2.300×10^{-4}	-1.984×10^{-4}	-1.219×10^{-2}	-1.215×10^{-2}	7.941×10^{-4}	-9.879×10^{-4}	3.138×10^{-2}	-5.790×10^{-2}	5.046×10^{-4}	6.879×10^{-4}
1.901	-1.371×10^{-2}	1.360×10^{-2}	-1.723×10^{-4}	-2.574×10^{-4}	-1.149×10^{-2}	-1.070×10^{-2}	6.739×10^{-4}	-8.993×10^{-4}	2.088×10^{-2}	-4.894×10^{-2}	5.229×10^{-4}	6.649×10^{-4}
2.001	-1.154×10^{-2}	1.254×10^{-2}	-1.296×10^{-4}	-3.099×10^{-4}	-1.066×10^{-2}	-9.310×10^{-3}	5.756×10^{-4}	-8.059×10^{-4}	1.375×10^{-2}	-4.175×10^{-2}	5.296×10^{-4}	6.320×10^{-4}
2.101	-9.675×10^{-3}	1.141×10^{-2}	-9.989×10^{-5}	-3.541×10^{-4}	-9.740×10^{-3}	-7.972×10^{-3}	4.970×10^{-4}	-7.120×10^{-4}	8.848×10^{-3}	-3.585×10^{-2}	5.265×10^{-4}	5.907×10^{-4}
2.201	-8.117×10^{-3}	1.028×10^{-2}	-7.934×10^{-5}	-3.892×10^{-4}	-8.886×10^{-3}	-6.797×10^{-3}	4.337×10^{-4}	-6.199×10^{-4}	5.557×10^{-3}	-3.123×10^{-2}	5.139×10^{-4}	5.441×10^{-4}
2.301	-6.862×10^{-3}	9.182×10^{-3}	-6.584×10^{-5}	-4.148×10^{-4}	-8.079×10^{-3}	-5.735×10^{-3}	3.834×10^{-4}	-5.318×10^{-4}	3.260×10^{-3}	-2.744×10^{-2}	4.938×10^{-4}	4.942×10^{-4}
2.401	-5.746×10^{-3}	8.061×10^{-3}	-5.774×10^{-5}	-4.311×10^{-4}	-7.264×10^{-3}	-4.790×10^{-3}	3.437×10^{-4}	-4.494×10^{-4}	1.817×10^{-3}	-2.447×10^{-2}	4.681×10^{-4}	4.419×10^{-4}
2.501	-4.754×10^{-3}	6.925×10^{-3}	-5.210×10^{-5}	-4.390×10^{-4}	-6.440×10^{-3}	-3.932×10^{-3}	3.107×10^{-4}	-3.733×10^{-4}	8.937×10^{-4}	-2.206×10^{-2}	4.370×10^{-4}	3.912×10^{-4}
2.601	-3.896×10^{-3}	5.777×10^{-3}	-4.913×10^{-5}	-4.392×10^{-4}	-5.633×10^{-3}	-3.152×10^{-3}	2.847×10^{-4}	-3.060×10^{-4}	2.644×10^{-4}	-2.001×10^{-2}	4.041×10^{-4}	3.410×10^{-4}
2.701	-3.160×10^{-3}	4.668×10^{-3}	-4.683×10^{-5}	-4.331×10^{-4}	-4.874×10^{-3}	-2.440×10^{-3}	2.629×10^{-4}	-2.460×10^{-4}	-1.439×10^{-4}	-1.823×10^{-2}	3.694×10^{-4}	2.940×10^{-4}
2.801	-2.499×10^{-3}	3.589×10^{-3}	-4.483×10^{-5}	-4.211×10^{-4}	-4.160×10^{-3}	-1.814×10^{-3}	2.444×10^{-4}	-1.929×10^{-4}	-4.162×10^{-4}	-1.662×10^{-2}	3.338×10^{-4}	2.501×10^{-4}
2.901	-1.957×10^{-3}	2.602×10^{-3}	-4.285×10^{-5}	-4.056×10^{-4}	-3.538×10^{-3}	-1.287×10^{-3}	2.281×10^{-4}	-1.482×10^{-4}	-5.767×10^{-4}	-1.522×10^{-2}	2.996×10^{-4}	2.102×10^{-4}
3.001	-1.456×10^{-3}	1.665×10^{-3}	-4.031×10^{-5}	-3.870×10^{-4}	-2.955×10^{-3}	-8.248×10^{-4}	2.132×10^{-4}	-1.097×10^{-4}	-6.466×10^{-4}	-1.393×10^{-2}	2.660×10^{-4}	1.753×10^{-4}
3.101	-1.087×10^{-3}	8.782×10^{-4}	-3.741×10^{-5}	-3.671×10^{-4}	-2.502×10^{-3}	-4.903×10^{-4}	1.995×10^{-4}	-7.772×10^{-5}	-6.775×10^{-4}	-1.282×10^{-2}	2.346×10^{-4}	1.433×10^{-4}
3.201	-8.082×10^{-4}	2.024×10^{-4}	-3.415×10^{-5}	-3.459×10^{-4}	-2.130×10^{-3}	-2.430×10^{-4}	1.872×10^{-4}	-5.123×10^{-5}	-6.945×10^{-4}	-1.179×10^{-2}	2.051×10^{-4}	1.163×10^{-4}
3.301	-5.949×10^{-4}	-3.586×10^{-4}	-3.030×10^{-5}	-3.245×10^{-4}	-1.841×10^{-3}	-6.112×10^{-5}	1.748×10^{-4}	-2.929×10^{-5}	-6.672×10^{-4}	-1.095×10^{-2}	1.781×10^{-4}	9.261×10^{-5}
3.401	-4.416×10^{-4}	-8.563×10^{-4}	-2.668×10^{-5}	-3.036×10^{-4}	-1.615×10^{-3}	5.790×10^{-5}	1.635×10^{-4}	-1.184×10^{-5}	-6.497×10^{-4}	-1.019×10^{-2}	1.541×10^{-4}	7.254×10^{-5}
3.501	-3.380×10^{-4}	-1.229×10^{-3}	-2.288×10^{-5}	-2.838×10^{-4}	-1.446×10^{-3}	1.078×10^{-4}	1.529×10^{-4}	1.821×10^{-6}	-6.073×10^{-4}	-9.538×10^{-3}	1.323×10^{-4}	5.553×10^{-5}
3.601	-2.548×10^{-4}	-1.590×10^{-3}	-1.884×10^{-5}	-2.653×10^{-4}	-1.305×10^{-3}	1.403×10^{-4}	1.426×10^{-4}	1.276×10^{-5}	-5.735×10^{-4}	-8.950×10^{-3}	1.127×10^{-4}	4.119×10^{-5}
3.701	-3.003×10^{-4}	-1.760×10^{-3}	-1.476×10^{-5}	-2.474×10^{-4}	-1.289×10^{-3}	7.839×10^{-5}	1.324×10^{-4}	2.140×10^{-5}	-5.790×10^{-4}	-8.425×10^{-3}	9.546×10^{-5}	2.966×10^{-5}
3.801	-2.796×10^{-4}	-1.976×10^{-3}	-1.119×10^{-5}	-2.318×10^{-4}	-1.231×10^{-3}	5.794×10^{-5}	1.235×10^{-4}	2.756×10^{-5}	-5.466×10^{-4}	-8.003×10^{-3}	8.061×10^{-5}	1.973×10^{-5}
3.901	-2.138×10^{-4}	-2.269×10^{-3}	-7.747×10^{-6}	-2.179×10^{-4}	-1.131×10^{-3}	6.653×10^{-5}	1.146×10^{-4}	3.219×10^{-5}	-5.126×10^{-4}	-7.516×10^{-3}	6.789×10^{-5}	1.093×10^{-5}
4.001	-1.926×10^{-4}	-2.433×10^{-3}	-4.371×10^{-6}	-2.045×10^{-4}	-1.045×10^{-3}	3.904×10^{-5}	1.063×10^{-4}	3.530×10^{-5}	-4.771×10^{-4}	-7.074×10^{-3}	5.643×10^{-5}	4.836×10^{-6}

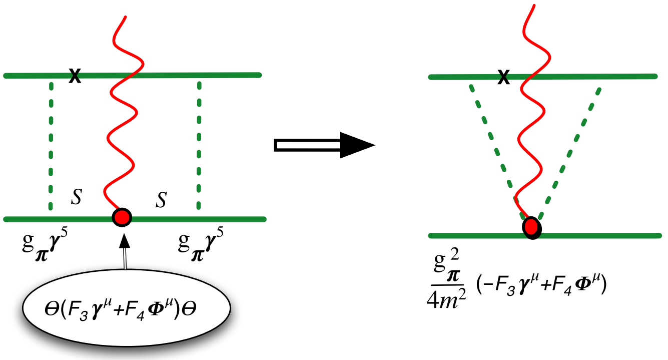

FIG. 23. Figure showing how the use of off-shell form factors (left panel) can generate IC diagrams (right panel). In this case, the removal of a one-pion exchange interaction from the CST kernel with off-shell form factors is equivalent to another calculation with a two-pion interaction current and no off-shell form factors.

propagators S, leaving a two-pion exchange term with an effective interaction at the $2\pi NN$ vertex.

This correspondence mirrors that shown in Fig. 8 of Ref. I. In that case, the off-shell sigma coupling canceled the nucleon propagators. Here the details are very different, but the way in which off-shell projectors cancel propagators, reducing the effective interaction of the off shell particle to a point interaction (modified by F_3 or F_4), is the same. It is another example of the theorem I proposed in Ref. I: A theory with *off-shell couplings* is equivalent to another theory with *no off-shell couplings plus an infinite number of very complex interaction currents*.

This comparison provides two further insights. First, I showed in Ref. [1] that the momentum-dependent couplings in the kernel did not generate any two-pion exchange currents, while, as the example in Fig. 23 shows, the off-shell form factors do. Second, since the comparison suggests the physical role for F_4 is to generate two-pion exchange currents (as well as exchange currents involving other pairs of mesons) perhaps a more natural scale for the Φ^μ factor multiplying F_4 is $1/m_\pi$ (instead of $1/m$ which is merely a carryover from the factors multiplying F_2). If this were the case, the F_4 form factor would be $m/m_\pi \approx 7$ times smaller that the curves shown in Figs. 4 and 5. The new F_4 would be more comparable in size to F_3.

D. Outlook

I remind the reader that model VODG provides a very good explanation of the data for A, B, and T_{20}. However, the revised model IIB, which is the basis of the VODG calculation, does not give a high-precision fit to the *np* data. The newer high-precision fits provided by models WJC1 and WJC2, with their momentum-dependent couplings and accompanying exchange currents, required a completely new calculation.

The fits to the off-shell form factors and the prediction of a new high-Q^2 behavior of G_{En} completely fixes model WJC2 and allows for a precise prediction, without any free parameters, for the rescattering term in deuteron electrodisintegration at modest energy using the CST [65]. In addition to being important in its own right, comparing this prediction to electrodisintegration data would be a decisive test of the CST.

Finally, extending the measurements of A and particularly B or T_{20} to higher Q^2 would yield new information about the off-shell deuteron form factors, and perhaps (in the absence of direct measurements) the neutron charge form factor G_{En}. This paper provides the predictions with which to compare experimental results. Note in particular the CST prediction that B will flatten out and reach a secondary maximum [recall Fig. 6]. The large size of B in this region may make measurements less difficult than previously anticipated, and it is important to confirm this expected behavior.

ACKNOWLEDGMENTS

This work was partially supported by Jefferson Science Associates, LLC, under U.S. DOE, Office of Science, Office of Nuclear Physics Contract No. DE-AC05-06OR23177. I especially want to thank Ingo Sick for sharing his global analysis (GA), without which it would have been more difficult to complete this work. It is also a pleasure to thank my colleagues for their support and collaboration over the years. In particular, I thank J. W. Van Orden, Alfred Stadler, and Carl Carlson for their significant contributions to the development of the CST as applied to *NN* scattering and to previous calculations of the deuteron form factors.

APPENDIX A: SHORT REVIEW OF THE THEORY

This Appendix reviews some details of the calculations of the deuteron form factors discussed in several previous papers, but also includes some new analysis useful for a detailed understanding of this paper.

1. Form factors and helicity amplitudes

The most general form of the covariant deuteron electromagnetic vector current illustrated in Figs. 1 and 3 can be expressed in terms of three deuteron form factors,

$$\begin{aligned}\langle P_+\,\lambda|J^\mu|P_-\,\lambda'\rangle\\ &= -2D^\mu\left\{G_1\,\xi^*_\lambda\cdot\xi'_{\lambda'} - G_3\frac{(\xi^*_\lambda\cdot q)(\xi'_{\lambda'}\cdot q)}{2m_d^2}\right\}\\ &\quad - G_M\left[\xi'^\mu_{\lambda'}(\xi^*_\lambda\cdot q) - \xi^{*\mu}_\lambda(\xi'_{\lambda'}\cdot q)\right],\end{aligned} \tag{A1}$$

where the form factors G_1, G_3, and $G_M = G_2$ are all functions of the square of the momentum transfer $q = P_+ - P_-$, with $Q^2 = -q^2$, $D^\mu = \frac{1}{2}(P_+ + P_-)^\mu$, and $\xi'_{\lambda'}$ (ξ_λ) are the four-vector polarizations of the incoming (outgoing) deuterons with helicities λ' (λ). The polarization vectors satisfy the well-known constraints

$$\begin{aligned}&P_+\cdot\xi_\lambda = P_-\cdot\xi'_{\lambda'} = 0, \quad \xi^*_\lambda\cdot\xi_\rho = -\delta_{\lambda\rho},\\ &\xi'^*_{\lambda'}\cdot\xi'_{\rho'} = -\delta_{\lambda'\rho'}.\end{aligned} \tag{A2}$$

This notation agrees with that used in Ref. [11], except that now λ denotes the helicity of the *outgoing* deuteron and λ' the helicity of the *incoming* deuteron.

The form factors G_1 and G_3 are usually replaced by the charge and quadrupole form factors, defined by

$$G_C = G_1 + \tfrac{2}{3}\eta G_Q, \quad G_Q = G_1 + (1+\eta)G_3 - G_M, \tag{A3}$$

with η defined in Eq. (1.23). At $Q^2 = 0$, the three form factors G_C, G_Q, and G_M give the charge, quadrupole moment, and magnetic moment of the deuteron:

$$\begin{aligned} G_C(0) &= \;1\; = G_1(0) && \text{(units of } e), \\ G_M(0) &= \mu_d = G_2(0) && \text{(units of } e/2m_d), \\ G_Q(0) &= Q_d = G_3(0) + 1 - \mu_d && \big(\text{units of } e/m_d^2\big). \end{aligned} \tag{A4}$$

Contracting the vector current (A1) with the photon helicity vectors

$$\epsilon_0^\mu = \{0, 0, 0, 1\}, \quad \epsilon_\pm^\mu = \{0, \mp 1, -i, 0\}/\sqrt{2} \tag{A5}$$

gives the helicity amplitudes, denoted by

$$G^{\lambda_\gamma}_{\lambda\lambda'} \equiv \langle P_+\,\lambda|J_\mu|P_-\,\lambda'\rangle\epsilon^\mu_{\lambda_\gamma}. \tag{A6}$$

The properties of the helicity amplitudes are discussed in Sec. III of Ref. II, where it was shown that only three of the possible 27 amplitudes are independent, so the form factors can be expressed in terms of the three combinations

$$\begin{aligned} \mathcal{J}_1 &\equiv G^0_{00} = 2D_0\left(G_C + \frac{4}{3}\eta\, G_Q\right), \\ \mathcal{J}_2 &\equiv G^0_{+-} = 2D_0\left(G_C - \frac{2}{3}\eta\, G_Q\right), \\ \mathcal{J}_3 &\equiv \frac{1}{2}(G^+_{+0} + G^-_{0-}) = Q\frac{D_0}{M_d}\, G_M, \end{aligned} \tag{A7}$$

where the symmetrized sum in the definition of $\mathcal{J}_3$ is used for convenience. To calculate the deuteron form factors, it therefore sufficient to calculate the $\mathcal{J}_n$ (with $n = 1, 2, 3$).

The experimental observables A, B, and $\widetilde{T}_{20}$ were defined in terms of the form factors in Eqs. (1.22) and (1.24).

2. Mathematical form of the current

The helicity amplitudes of the current, $\mathcal{J}_n(q)$, are the sum of the three types of contributions shown in Fig. 3:

$$\mathcal{J}_n(q) = \mathcal{J}_n^A(q) + \mathcal{J}_n^{(2)}(q) + \mathcal{J}_n^B(q). \tag{A8}$$

The $\mathcal{J}_n^A$ and $\mathcal{J}_n^{(2)}$ contributions were combined in Eq. (3.28) of Ref. II; here I find it convenient to write them as two separate terms. Including the (B) diagrams from Eq. (3.36) of Ref. II, all three contributions can be written in a compact form:

$$\begin{aligned} \mathcal{J}_n^A(q) = e_0 \int_k \bigg\{ & f_0(p_+, p_-) \sum_{i=1}^{2} [F_i(Q^2)\mathcal{A}_{n,i}(\Psi_+\Psi_-)] \\ & + \frac{g_0(p_+, p_-)}{4m^2} \sum_{i=3}^{4} [F_i(Q^2)\mathcal{A}_{n,i}(\Gamma_+\Gamma_-)]\bigg\}, \end{aligned} \tag{A9a}$$

$$\begin{aligned} \mathcal{J}_n^{(2)}(q) = -e_0 \int_k \sum_{i=1}^{2} F_i(Q^2) \bigg[& \frac{h_+}{h_-}\mathcal{A}_{n,i}(\Psi_+\Psi_-^{(2)}) \\ & + \frac{h_-}{h_+}\mathcal{A}_{n,i}(\Psi_+^{(2)}\Psi_-)\bigg], \end{aligned} \tag{A9b}$$

$$\begin{aligned} \mathcal{J}_n^B(q) = e_0 \int_k \Bigg\{ & \left[\frac{mE_k}{k_z Q}\right] \sum_{i=1}^{2} F_i(Q^2) \left(\frac{\mathcal{B}_{n,i}(k_0)}{k_0}\bigg|_- - \frac{\mathcal{B}_{n,i}(k_0)}{k_0}\bigg|_+ \right) \\ & - \frac{1}{m}\mathcal{O}_n \sum_{i=1}^{2} F_i(Q^2)\mathcal{C}_{n,i}(\Gamma\, \widehat{\Gamma}_{\text{off}})\Bigg\}, \end{aligned} \tag{A9c}$$

where the integral is

$$\int_k = \int \frac{d^3k}{(2\pi)^3}\frac{m}{E_k}, \tag{A10}$$

the operator $\mathcal{O}_n X(q) = X(q) + \epsilon_{n3}X(-q)$, with the phase $\epsilon_{n3} = (1 - 2\delta_{n3})$, and $|_\pm \to |_{k_0 = E_\pm}$, where $E_\pm$ was defined in Eq. (1.5). The coefficient of the g_0 term in Eq. (A9a) differs from that reported in Ref. II; it includes a sum over *two* off-shell nucleon form factors, F_3 and F_4, defined in Eq. (1.13). The quantities $\mathcal{A}$, $\mathcal{B}$, and $\mathcal{C}$ are traces over products of pairs of covariant wave functions (or vertex functions), summarized in Table VII, one for the initial and one for the final deuteron, and are multiplied by one of the four form factors describing the interaction of the virtual photon with the off-shell nucleon. The detailed formulas for these traces are given in Ref. II: Eqs. (B1) and (B2) for $\mathcal{A}$, Eqs. (B6) and (B7) for $\mathcal{B}$, and Eqs. (B9) and (B10) for $\mathcal{C}$. I found corrections to these formulas that are reported in Appendix G.

The three types of wave functions or vertex functions that enter into the traces (A9a)–(A9c) are Ψ, $\Psi^{(2)}$, and $\widehat{\Gamma}_{\text{BS}}$. The equation for the bound state wave function with particle 1 on shell is

$$S^{-1}(p)\;\; \Psi(\hat{k}, P) = -\int_{k'} \overline{V}(\hat{k}, \hat{k}'; P)\Psi(\hat{k}', P), \tag{A11}$$

where $\overline{V}$ is the symmetrized one-boson exchange (OBE) kernel (introduced in Ref. [14] and discussed in detail in Ref. I) and the volume integral was defined in (A10). The wave function $\Psi^{(2)}(\hat{k}, P)$ and the subtracted vertex function $\widehat{\Gamma}_{\text{BS}}(\widetilde{k}, P)$ (where $\widetilde{k} = \{k_0, \mathbf{k}\}$ can be off shell) are obtained from an iteration of the basic equation (A11) using the kernels $\overline{V}^{(2)}$ and $\overline{V} - \overline{V}^{(1)}$

$$S^{-1}(p)\Psi^{(2)}(\hat{k}, P) = -\int_{k'} \overline{V}_+^{(2)}(\hat{k}, \hat{k}'; P)\Psi(\hat{k}', P), \tag{A12a}$$

$$\widehat{\Gamma}_{\text{BS}}(\widetilde{k}, P) = -\int_{k'} [\overline{V} - \overline{V}_+^{(1)}](\widetilde{k}, \hat{k}'; P)\Psi(\hat{k}', P), \tag{A12b}$$

where $\overline{V}_+^{(1)}$ and $\overline{V}_+^{(2)}$ are kernels constructed from the momentum dependence of the meson-NN vertex couplings to particles 1 and 2 as described in Ref. I and used in the diagrams shown in Fig. 2. The computation of the wave functions $\overline{\Psi}^{(2)}$ and $\overline{\widehat{\Gamma}}_{\text{BS}}$ requires the transformed kernels $\overline{V}_-^{(1)}$ and $\overline{V}_-^{(2)}$.

The off-shell subtracted vertex function $\widehat{\Gamma}_{\text{BS}}$ is composed of two parts with a different matrix structure. These were previously defined in Eq. (3.7). The B part of the vertex function appears in the $\mathcal{B}$ traces and the C part in the $\mathcal{C}$ traces. [The reader is warned not to confuse the B term in Eq. (3.7) with the total contribution to the (B) diagrams.] Note that each of the $\mathcal{B}$ trace terms is singular when $Q \to 0$, and only through the cancellation of the two terms at $k_0 = E_\pm$ is this singularity removed. This cancellation is required by the physical behavior of this contribution, as discussed in detail in Sec. II F of Ref. I. The C term vanishes when particle 1 is on shell and is interesting because it is a measure of contributions from off-shell terms that do not contribute to the on-shell two-body CST equation used to fix the parameters of the kernel.

3. Relativistic effects due to shifts in the arguments of the wave functions

The wave functions and vertex functions (referred to collectively as wave functions in the following discussion) that enter into the relativistic formulas have arguments shifted by the relativistic kinematics. It is of considerable interest in itself to study the size of these affects, and this is the focus of this subsection.

a. Arguments for the A diagrams

As discussed in Sec. II C of Ref. II, when one particle is on shell, the wave functions depend on only one variable, which I have chosen to be $\mathbf{k}^2$ (the square of the three-momentum of the on-shell particle 1). When boosted to the rest frame, this variable is denoted by R^2, which is then either the momentum of particle 1 or the relative momentum of both particles (identical in the rest frame). The quantity R is a function of $\mathbf{k}^2$, k_z (the component of $\mathbf{k}$ in the direction of $\mathbf{q}$), and Q.

For the A diagrams, with the momenta labeled as in Fig. 1(A), the exact expression for this argument is [using R_A^2 for rest frame values from diagram (A)]

$$(R_A^\pm)^2 = \frac{(P_\pm\cdot\hat{k})^2}{m_d^2} - m^2 \tag{A13a}$$

$$= \mathbf{k}^2 \mp k_z\, Q\frac{D_0E_k}{m_d^2} + \eta\big(E_k^2 + k_z^2\big) \tag{A13b}$$

$$\to \left(\mathbf{k} \mp \frac{1}{4}\mathbf{q}\right)^2 \qquad m, m_d \to \infty, \tag{A13c}$$

where $(R_A^-)^2$ $[(R_A^+)^2]$ is the rest frame value of R_A^2 obtained from a moving incoming (outgoing) deuteron in the Breit frame.

The last expression, Eq. (A13c), is the value of the rest frame momentum $(R_A^\pm)^2$ in the infinite mass (nonrelativistic) limit, and shows that, nonrelativistically, these momenta must be interpreted as the *relative* momenta, $\boldsymbol{\rho} = \frac{1}{2}(\mathbf{k}_1 - \mathbf{k}_2)$, because before and after the collision with the photon, the assignment of momenta that correctly describes this process is

$$\text{before}\quad \begin{cases} \mathbf{k}_1 = \mathbf{k} \\ \mathbf{k}_2 = -\mathbf{k} - \frac{1}{2}\mathbf{q}, \\ \boldsymbol{\rho} = \mathbf{k} + \frac{1}{4}\mathbf{q} \end{cases}$$

$$\text{after}\quad \begin{cases} \mathbf{k}_1 = \mathbf{k} \\ \mathbf{k}_2 = -\mathbf{k} + \frac{1}{2}\mathbf{q}. \\ \boldsymbol{\rho} = \mathbf{k} - \frac{1}{4}\mathbf{q} \end{cases} \tag{A14}$$

Note the reassuring fact that Eq. (A13a) gives the same result if $\hat{k}$ is replaced by the relative momentum in the moving frame:

$$\begin{aligned}(R_A^{\pm\prime})^2 &= \frac{\big[P_\pm\cdot\big(\hat{k} - \frac{1}{2}P_\pm\big)\big]^2}{m_d^2} - \left(\hat{k} - \frac{1}{2}P_\pm\right)^2 \\ &= \frac{(P_\pm\cdot\hat{k})^2}{m_d^2} - (P_\pm\cdot\hat{k}) + \frac{m_d^2}{4} - m^2 + (P_\pm\cdot\hat{k}) - \frac{m_d^2}{4} \\ &= (R_A^\pm)^2.\end{aligned} \tag{A15}$$

The lesson from this discussion is that the effective rest frame momentum, $(R_A^\pm)^2$, is the same whether or not one starts in the moving frame from the four-momentum of particle 1, or the relative four-momentum of the two particles; this must be true, of course, since the two are indistinguishable in the rest system.

To better understand the results (A13b) and (A13c), it is useful to obtain the longitudinal and transverse components of $\mathbf{R}_A^\pm$ by directly transforming the components of $\hat{k} = \{E_k, k_\perp, k_z\}$ from the moving system to the rest system, using the relations

$$\begin{aligned}(R_A^\pm)_\perp &= k_\perp = k\sin\theta, \\ (R_A^\pm)_z &= \frac{D_0}{m_d}k\cos\theta \mp \frac{Q}{2m_d}E_k,\end{aligned} \tag{A16}$$

where it is easily shown that $(R_A^\pm)^2 = (R_A^\pm)_\perp^2 + (R_A^\pm)_z^2$. In Fig. 24, I show the related components

$$\begin{aligned} r_\perp &= \frac{(R_A^-)_\perp}{k} = \sin\theta, \\ r_z &= \frac{1}{k}\left[(R_A^-)_z - \frac{QE_k}{2m_d}\right] = \sqrt{1+\eta}\,\cos\theta \end{aligned} \tag{A17}$$

plotted in the $r_x = r_\perp$, r_z plane.

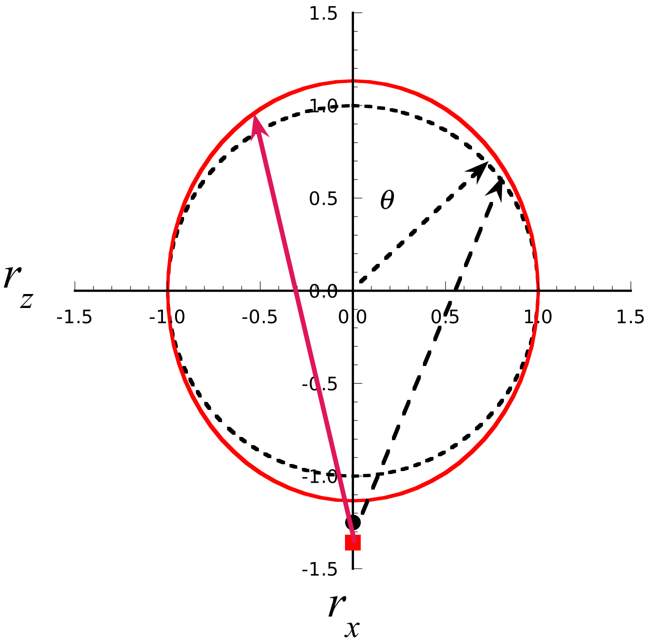

FIG. 24. Locus of the points r_z and $r_x = r_\perp$, Eq. (A17), as a function of θ. The two closed curves and the solid round and square reference points near $r_z \sim -1$ are discussed in the text. I chose $Q = 2$ GeV and $k = 400$ MeV when the curves or reference points depended on Q or k.

Two cases are shown in the figure. The first is the nonrelativistic limit of the boost (with $\eta = 0$). It is described by the dashed black circle which can be described as the locus of points swept out by the unit vector **r** (represented by the dashed arrow fixed to the origin) rotating through polar angle θ with the $\hat{z}$ axis. However, the *same* circle is also the locus of points swept out by $\mathbf{R}^-_\mathbf{A}/k$, represented by the longer black dashed vector, with one end fixed at the reference point (represented by the round black dot at $r_z^0 = -Q/(4k) = -1.25$ in the figure) and the other end following the locus of points swept out by dashed circle. This vector, which is the rest frame momentum in the nonrelativistic limit divided by k, must change length in order to track the dashed circle.

The second case shown is the solid red ellipse, which shows the behavior of the relativistic A-type rest-frame momentum. Because $\eta \neq 0$ ($\eta \simeq 0.02835$ for the parameters chosen), the curve changes from a circle to an ellipse and the reference point (represented by the solid red square) shifts to $r_z^0 = -QE_k/(2km_d) \simeq -1.359$. The vector that sweeps out the relativistic momentum $\mathbf{R}^-_\mathbf{A}/k$ is represented by the red arrow that connects the solid red square reference point to the ellipse. One can see clearly how the relativistic transformation changes the effective rest-frame momentum; the shift in the reference point is due to the role that the particle energy plays in the transformation, and change from a circle to an ellipse is due to the dilation factor in the transformation.

Figure 24 shows the relativistic ellipse *expanding* in the $\hat{z}$ direction, rather than contracting. This is because I am keeping k constant in the *moving frame*. To obtain this condition, I must start from an expanded ellipse in the rest frame, so that when it is contracted by the transformation to the moving system it will be compressed back into a circle. Hence, the transformation behaves as expected after all. This expansion explains qualitatively the behavior of the relativistic argument shift shown by the dashed blue line shown in Fig. 21.

b. Arguments for the B diagrams

For the B diagrams, when both particles can be off shell, the wave functions can depend on an additional variable, which was previously chosen to be the energy of particle 1 in the moving frame, k_0, which transformed to R_0 in the rest frame. The momenta are labeled in Fig. 3(B) and, following the discussion in Sec. III C, I make the substitution

$$\widetilde{k}_0^\pm = x_{10}^\pm \tilde{E}_\pm \tag{A18}$$

into the momenta given in Ref. II (with the change in notation $\tilde{R} \to R_B$):

$$\begin{aligned}
[R_B^\pm(\tilde{\mathbf{k}}, x_{10}^\pm)]^2 &= \frac{(P_\pm \cdot \widetilde{k}_\pm)^2}{m_d^2} - \widetilde{k}_\pm^2 = \tilde{k}_\perp^2 + \tilde{k}_{\pm z}^2 \\
&\quad \mp x_{10}^\pm\, \tilde{k}_{\pm z} Q \frac{D_0 \tilde{E}_\pm}{m_d^2} + \eta\big[(x_{10}^\pm\, \tilde{E}_\pm)^2 + \tilde{k}_{\pm z}^2\big] \\
&\to \tilde{k}_\perp^2 + \tilde{k}_{\pm z}^2 \mp \frac{1}{2} x_{10}^\pm \tilde{k}_{\pm z} Q + x_{10}^{\pm 2} \frac{Q^2}{16} \\
&= \left[\tilde{\mathbf{k}} \pm \frac{1}{4}(2 - x_{10}^\pm)\mathbf{q}\right]^2 \quad m, m_d \to \infty,
\end{aligned}$$

$$\begin{aligned}
R_0^\pm(\tilde{\mathbf{k}}, x_{10}^\pm) &= \frac{P_\pm \cdot \widetilde{k}_\pm}{m_d} = \frac{1}{2m_d}[2x_{10}^\pm D_0 \tilde{E}_\pm \mp \tilde{k}_{\pm z} Q] \\
&\to x_{10}^\pm m + \frac{x_{10}^\pm}{2m}\left[\tilde{k}_\perp^2 + \tilde{k}_{\pm z}^2 + \frac{1}{8}Q^2\right] \mp \frac{\tilde{k}_{\pm z} Q}{4m} \\
&= x_{10}^\pm m + \frac{1}{2m}\Bigg[x_{10}^\pm \tilde{k}^2 \pm \frac{1}{2}\tilde{k}_z Q(2x_{10}^\pm - 1) \\
&\quad + \frac{1}{16}(5x_{10}^\pm - 4)Q^2\Bigg] \quad m, m_d \to \infty,
\end{aligned} \tag{A19}$$

where [recalling that the momenta in Fig. 3(B) are labeled with a tilda to distinguish them from momenta in Fig. 3(A)]

$$\widetilde{k}_\pm = \{x_{10}^\pm \tilde{E}_\pm, \tilde{\mathbf{k}} \pm \tfrac{1}{2}\mathbf{q}\}, \quad \tilde{k}_{\pm z} = \tilde{k}_z \pm \tfrac{1}{2}Q. \tag{A20}$$

I prefer using the variable x_{10} instead of the unconstrained energy k_0 because when particle 1 is on- shell, $x_{10} = 1$, independent of momenta. Hence,

$$\begin{aligned}
[R_B^\pm(\tilde{\mathbf{k}}, 1)]^2 &= \tilde{k}_\perp^2 + \tilde{k}_{\pm z}^2 \mp \tilde{k}_{\pm z} Q \frac{D_0 \tilde{E}_\pm}{m_d^2} + \eta[\tilde{E}_\pm^2 + \tilde{k}_{\pm z}^2] \\
&\to \left(\tilde{\mathbf{k}} \pm \frac{1}{4}\mathbf{q}\right) \qquad m, m_d \to \infty, \\
R_0^\pm(\tilde{\mathbf{k}}, 1) &= \frac{1}{2m_d}[2D_0 \tilde{E}_\pm \mp \tilde{k}_{\pm z} Q], \\
&\to m + \frac{1}{2m}\left(\tilde{\mathbf{k}} \pm \frac{1}{4}\mathbf{q}\right)^2 \quad m, m_d \to \infty.
\end{aligned} \tag{A21}$$

It is easy to see that $R_0^\pm$ is constrained by the mass shell condition

$$R_0^\pm(\tilde{\mathbf{k}}, 1) = \sqrt{m^2 + [R_B^\pm(\tilde{\mathbf{k}}, 1)]^2}, \tag{A22}$$

as required by relativity. The condition $x_{10}^\pm = 1$ is now a simple, momentum-independent way to specify that particle 1 is on-shell.

In the calculation of the (B) diagram, only the values of $x_{10}^\pm$ given in Eq. (3.3) are needed. To order $1/m^2$, these are

$$x_{10}^\pm = \zeta^\pm \simeq 1 + \frac{\tilde{k}_\mp^2}{2m^2} - \frac{\tilde{k}_\pm^2}{2m^2} = 1 \mp \frac{\tilde{k}_z Q}{m^2}. \tag{A23}$$

When this is substituted into (A19), the result to order $1/m^2$ is

$$\begin{aligned}
R_0^\pm(\tilde{\mathbf{k}}, \zeta^\pm) &\simeq m\left(1 \mp \frac{\tilde{k}_z Q}{m^2}\right) + \frac{1}{2m}\left[\tilde{k}^2 \pm \frac{1}{2}\tilde{k}_z Q + \frac{Q^2}{16}\right] \\
&= m + \frac{1}{2m}\left[\tilde{k}^2 \mp \frac{1}{2}\tilde{k}_z Q + \frac{Q^2}{16}\right] \\
&\simeq \sqrt{m^2 + \left(\tilde{\mathbf{k}} \mp \frac{1}{4}\mathbf{q}\right)^2},
\end{aligned} \tag{A24}$$

showing that the mass shell condition holds to order $1/m^2$.

While $x_{10}^\pm$ is the appropriate quantity describing the off-shell behavior in the moving frame, the quantity that describes this in the rest frame of each state, denoted by $X_{10}^\pm(\tilde{\mathbf{k}}, x_{10}^\pm)$, is defined by the relations

$$R_0^\pm(\tilde{\mathbf{k}}, x_{10}^\pm) = X_{10}^\pm(\tilde{\mathbf{k}}, x_{10}^\pm)\sqrt{m^2 + [R_B^\pm(\tilde{\mathbf{k}}, x_{10}^\pm)]^2}. \tag{A25}$$

This can be derived directly by transforming $\tilde{k}_0^\pm$ and $\tilde{E}_\pm$ in Eq. (A18) to the *rest frame* and requiring the transformation of $x_{10}^\pm \to X_{10}^\pm$ to maintain the equation. Note that setting $x_{10}^\pm = 1$ in (A25) and using the relation (A22) gives the result $X_{10}^\pm(\tilde{\mathbf{k}}, 1) = 1$.

It is satisfying to observe that nonrelativistic limits of the momenta (A19) [or (A21)] correctly describe the process in which the photon is absorption on particle 1 instead of particle 2:

$$\text{before}\quad \begin{cases} \mathbf{k}_1 = \mathbf{k} - \frac{1}{2}\mathbf{q} \\ \mathbf{k}_2 = -\mathbf{k} \\ \boldsymbol{\rho} = \mathbf{k} - \frac{1}{4}\mathbf{q} \end{cases},$$

$$\text{after}\quad \begin{cases} \mathbf{k}_1 = \mathbf{k} + \frac{1}{2}\mathbf{q} \\ \mathbf{k}_2 = -\mathbf{k} \\ \boldsymbol{\rho} = \mathbf{k} + \frac{1}{4}\mathbf{q} \end{cases}. \qquad \text{(A26)}$$

This is a consequence of the fact that the nonrelativistic limit of $[R_B^\pm(\tilde{\mathbf{k}}, 1)]^2$ is *not equal* to $(R_A^\pm)^2$.

As I did in the previous subsection, it is useful to derive (A19) directly from the Lorentz boost. Starting from the off-shell four-momentum of particle 1 in the moving frame, $\tilde{k}_\pm = \{x_{10}^\pm \tilde{E}_\pm, \tilde{\mathbf{k}} \pm \frac{1}{2}Q\}$ (where $\tilde{k}_\pm$ pairs with momenta $P_\pm$), and transforming to the rest frame using $R_B^\pm = \Lambda_\mp \tilde{k}_\pm$, gives

$$(R_B^\pm)_\perp = \tilde{k}_\perp = \tilde{k}\sin\theta,$$

$$(R_B^\pm)_z = \frac{D_0}{m_d}\tilde{k}_{\pm z} \mp x_{10}^\pm \frac{Q\tilde{E}_\pm}{2m_d},$$

$$R_0^\pm = \mp\frac{Q\tilde{k}_{\pm z}}{2m_d} + x_{10}^\pm \frac{D_0\tilde{E}_\pm}{m_d}. \qquad \text{(A27)}$$

This result for $R_0^\pm$ agrees immediately with (A19), and it is also easy to show that $[R_B^\pm]^2 = (R_B^\pm)_\perp^2 + (R_B^\pm)_z^2$ as expected.

To represent the behavior of the spacial components when particle 1 is on shell, Fig. 25 shows the behavior of the two components that enter into the (B$_+$) diagram when $x_{10} = 1$:

$$r_\perp^b = \frac{1}{\tilde{k}}[R_B^+(1)]_\perp = \sin\theta,$$

$$r_z^b = \frac{1}{\tilde{k}}\left[[R_B^+(1)]_z - \frac{Q}{2m_d}(D_0 - E_0)\right]$$

$$= \sqrt{1+\eta}\,\cos\theta - \frac{Q}{2km_d}(E_+ - E_0). \qquad \text{(A28)}$$

In defining r_z^b, I introduced a new subtraction term depending on the energy E_0,

$$E_0 \equiv \sqrt{m^2 + k^2 + \frac{Q^2}{4}} = E_+(\cos\theta = 0), \qquad \text{(A29)}$$

chosen to be independent of θ and of the correct size to center the elliptical locus of the points $\{r_\perp^b, r_z^b\}$ at the origin.

The solid red ellipse shown in Fig. 25 is the locus of points swept out by the vector $\mathbf{R}_\mathbf{B}^+/\tilde{k}$, which reaches from the new reference point (the subtraction term) shown as a solid red diamond located on the $\hat{z}$ axis at -0.930 to the smaller of the red ellipses, and has a different length than the one for diagram (A). For comparison, the ellipse for the transformation of diagram (A) shown in Fig. 24 is the red dashed ellipse in Fig. 25. The Lorentz transformation of the (A) and (B) diagrams *have very different behaviors*, which can be traced to the different behavior of the energies of particle 1 in the two cases.

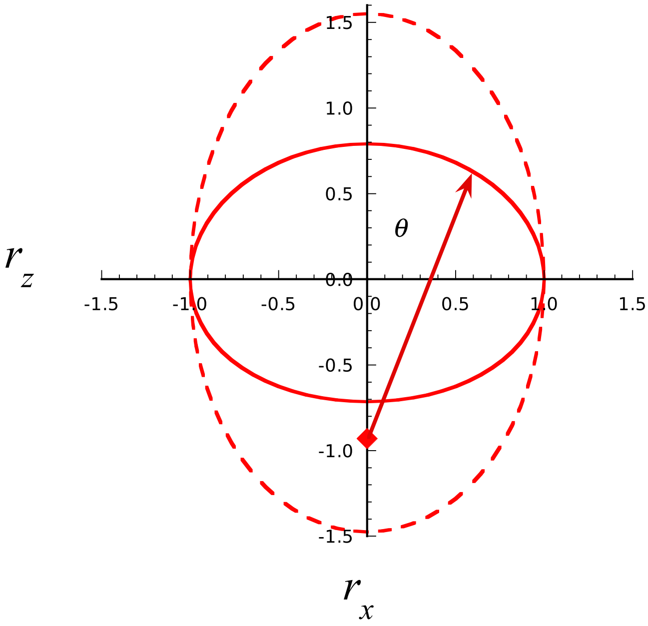

FIG. 25. Locus of the points $\{r_z^b, r_\perp^b\}$ of Eq. (A28) (the solid line ellipse) compared to $\{r_z, r_\perp\}$ of Eq. (A17) (the dashed-line ellipse, identical to the one shown in Fig. 24) as a function of θ. The diamond reference point near $r_z \sim -1$ is the point from which the magnitude of the transformed momentum is measured. I choose $Q = 2$ GeV and $k = 400$ MeV for this example.

I return now to the issue of how far off shell particle 1 is forced by the kinematics in the 3(B) diagrams. This was already addressed nonrelativistically in Sec. III C above. As I showed there, the relevant values of $x_{10}^\pm$, denoted $\zeta^\pm$, were given in Eq. (3.3). The correct quantity is therefore

$$X_{10}^\pm(\tilde{\mathbf{k}}, \zeta^\pm) = \frac{R_0^\pm(\tilde{\mathbf{k}}, \zeta^\pm)}{\sqrt{m^2 + [R_B^\pm(\tilde{\mathbf{k}}, \zeta^\pm)]^2}}$$

$$= \frac{2D_0\tilde{E}_\mp \mp \tilde{k}_{\pm z}Q}{\sqrt{(2D_0\tilde{E}_\mp \mp \tilde{k}_{\pm z}Q)^2 \pm 8m_d^2\tilde{k}_z Q}}. \qquad \text{(A30)}$$

The maximum of $X_{10}^\pm$ occurs when $\tilde{k}_z = \mp k$ (I drop the tilde at this point), giving

$$X_{10}^{\pm\max} = \frac{2D_0E_+(Q) + k_-Q}{\sqrt{(2D_0E_+(Q) + k_-Q)^2 - 8m_d^2 k\,Q}}, \qquad \text{(A31)}$$

where

$$E_\pm(Q) = \sqrt{m^2 + \left(k \pm \tfrac{1}{2}Q\right)^2}. \qquad \text{(A32)}$$

As for the nonboosted case, the minimum is found by changing $k \to -k$ (or $\theta = 0$ to π). Also, note that

$$\lim_{m_d\to\infty} X_{10}^{\pm\max} = \frac{E_+(Q)}{E_-(Q)}, \qquad \text{(A33)}$$

which, once $k_{\rm max}$ has been found, agrees with the result (3.4).

For each Q, this limiting function is has a maximum at a particular value of k (which is best found numerically) so the maximum and minimum for all k can be shown as a function of Q only. This limiting value was already shown in Fig. 16. The figure shows how far off shell the particle can be forced, even at modest values of Q.

4. Calculation of the off-shell invariant functions

The wave and vertex functions can be expanded into scalar functions. For a recent discussion of the decomposition of Ψ, see Appendix A of Ref. II and Sec. III of Ref. [15]. The wave function Ψ can be expressed in terms of four scalar functions: the two familiar nonrelativistic S- and D-state wave functions, u (S state), w (D state), and the two small P-state components of relativistic origin, v_t (spin triplet P state), and v_s (spin singlet P state), or alternatively in terms of the helicity amplitudes $z_\ell^{\rho_1\rho_2}$ (with $\rho_1=+$; see the discussion below). The momentum dependence of these wave functions was shown in Figs. 6 and 7 of Ref. [15].

In this subsection, I discuss a few technical details that I found helpful in carrying out the numerical calculations.

First, instead of using the amplitudes $z_\ell^{\rho_1\rho_2}$, where

$$
\begin{aligned}
z_0^{++}&=\frac{1}{\sqrt6}(u+\sqrt2 w),\quad z_1^{++}=\frac{1}{\sqrt6}(\sqrt2 u-w),\\
z_0^{+-}&=-\frac{1}{\sqrt2}v_s,\quad z_1^{+-}=-\frac{1}{\sqrt2}v_t,
\end{aligned}
\tag{A34}
$$

I use the related amplitudes

$$
y_\ell^{\rho_1\rho_2}(k,k_0)=\delta_{\rho_2}z_\ell^{\rho_1\rho_2}(k,k_0),
\tag{A35}
$$

where $\rho=\pm$ and δ_ρ is related to the inverse of the nucleon propagator G^ρ for positive- and negative-energy nucleon states. These propagators are

$$
\begin{aligned}
G^\rho&=\frac{\rho}{E_k+\rho(k_0-m_d)}\\
&=\frac{\rho}{E_k(1+\rho\,x_{10})-\rho\,m_d)}\equiv\frac{\rho}{\delta_\rho}.
\end{aligned}
\tag{A36}
$$

The reason for using the y's instead of the z's is that the propagator appears naturally when the z's are extended off shell. Since G^+ is singular at $\delta_+=0$, or at

$$
x_{10}=\frac{m_d-E_k}{E_k}\simeq 1-\frac{k^2}{m^2},
\tag{A37}
$$

the z's are singular at these points, and it is hard to compute them numerically around these singularities. The problem becomes critical because these singularities are very close to $x_{10}=1$ at small k^2. These singularities are canceled in the amplitudes y, which are very smooth near $x_{10}=1$ and provide a much better input for numerical solutions.

The eight invariant functions that define the Dirac-space form of the vertex function can be expressed in terms of the helicity amplitudes $y_\ell^{\rho_1\rho_2}$. The results in terms of the z's was given in Eq. (A27) of Ref. [2]. When expressed in terms of the y's, the relations become

$$
\begin{aligned}
\frac{F}{\mathcal{C}_0}&=(E_k+k_0)\Big[\delta_-y_1^{++}-\frac{m}{k}\delta_+y_1^{+-}\Big]\\
&\quad-(E_k-k_0)\Big[\delta_+y_1^{--}+\frac{m}{k}\delta_-y_1^{-+}\Big],\\
\frac{k^2G}{m\mathcal{C}_1}&=(E_k+k_0)\Big[\delta_-\Big(E_ky_0^{++}-\frac{my_1^{++}}{\sqrt2}\Big)-\frac{k\delta_+y_1^{+-}}{\sqrt2}\Big]\\
&\quad-(E_k-k_0)\Big[\delta_+\Big(E_ky_0^{--}-\frac{my_1^{--}}{\sqrt2}\Big)+\frac{k\delta_-y_1^{-+}}{\sqrt2}\Big],\\
\frac{k\,H}{mE_k\mathcal{C}_0}&=-(E_k+k_0)\,y_1^{+-}-(E_k-k_0)\,y_1^{-+},\\
\frac{k^2I}{m^2\mathcal{C}_1}&=(E_k+k_0)\Big[m\,y_0^{++}-\frac{E_k}{\sqrt2}y_1^{++}+k\,y_0^{+-}\Big]\\
&\quad-(E_k-k_0)\Big[m\,y_0^{--}-\frac{E_k}{\sqrt2}y_1^{--}-k\,y_0^{-+}\Big],\\
\frac{kK_1}{mE_k\mathcal{C}_0}&=-\delta_+y_1^{+-}-\delta_-y_1^{-+},\\
\frac{k^2K_2}{m^2\mathcal{C}_1}&=m\,\delta_-y_0^{++}-E_k\frac{\delta_-y_1^{++}}{\sqrt2}-k\delta_+y_0^{+-}\\
&\quad-m\,\delta_+y_0^{--}+E_k\frac{\delta_+y_1^{--}}{\sqrt2}-k\delta_-y_0^{-+},\\
\frac{kK_3}{m^2\mathcal{C}_0}&=-k\,y_1^{++}-m\,y_1^{-+}+k\,y_1^{--}-m\,y_1^{+-},\\
\frac{k^2K_4}{m^3\mathcal{C}_0}&=\sqrt2\,E_ky_0^{++}-my_1^{++}+ky_1^{-+}\\
&\quad-\sqrt2\,E_ky_0^{--}+my_1^{--}+ky_1^{+-},
\end{aligned}
\tag{A38}
$$

where

$$
\mathcal{C}_0=\frac{\sqrt3\,\mathcal{K}}{2E_km_d}\quad \mathcal{C}_1=\sqrt2\,\mathcal{C}_0
\tag{A39}
$$

with $\mathcal{K}=\pi\sqrt{2m_d}$.

It turns out that only the four amplitudes $y_\ell^{+\rho_2}$ need to be considered; the amplitudes $y_\ell^{-\rho_2}$ will never contribute to the final result. The argument is in two steps. First, when particle 1 is on shell, $k_0=E_k$, and the four invariant functions F, G, H, I do not depend on the amplitudes $y_\ell^{-\rho_2}$. Next, when both particles are off shell, only subtracted amplitudes $\hat H,\dots,\hat K_4$ contribute, and I have found that the *subtracted* amplitudes $\hat y_\ell^{-\rho_2}$ are numerically so small as to be nearly zero and can be discarded from the calculation. In this case, the subtracted $\hat K_i$ are not zero, but depend only on the amplitudes $\hat y_\ell^{+\rho_2}$. I have not looked for a proof of the relation $\hat y_\ell^{-\rho_2}=0$, which I believe to be true.

All of the invariants are regular as $k\to0$, yet the expressions for all but F show a possible singularity at $k=0$. To avoid this there, must be relations between the y's near $k=0$. To examine this, drop all of the $y_\ell^{-\rho_2}$ terms, substitute $k_0=x_{10}E_k$, and examine the $k\to0$ limits, dropping all terms proportional to k^2 or higher, since they are finite. Taking

$m_d \to 2m$, and using the expansions

$$\delta_+ \simeq m(x_{10}-1), \quad \delta_- \simeq m(3-x_{10}) \tag{A40}$$

gives

$$\begin{aligned}
\lim_{k\to 0} G &= \frac{G_0}{k^2}(1+x_{10})\bigg\{(3-x_{10})\bigg[y_0^{++}-\frac{y_1^{++}}{\sqrt{2}}\bigg] \\
&\quad -(x_{10}-1)\frac{k}{m}\frac{y_1^{+-}}{\sqrt{2}}\bigg\}, \\
\lim_{k\to 0} H &= \frac{H_0}{k}(1+x_{10})\,y_1^{+-}, \\
\lim_{k\to 0} I &= \frac{I_0}{k^2}(1+x_{10})\bigg(y_0^{++}-\frac{y_1^{++}}{\sqrt{2}}+\frac{k}{m}y_0^{+-}\bigg), \\
\lim_{k\to 0} K_1 &= \frac{K_{10}}{k}(x_{10}-1)\,y_1^{+-}, \\
\lim_{k\to 0} K_2 &= \frac{K_{20}}{k^2}\bigg\{(3-x_{10})\bigg[y_0^{++}-\frac{y_1^{++}}{\sqrt{2}}\bigg]-(x_{10}-1)\frac{k}{m}y_0^{+-}\bigg\}, \\
\lim_{k\to 0} K_3 &= \frac{K_{30}}{k}\bigg\{\frac{k}{m}y_1^{++}+y_1^{+-}\bigg\}, \\
\lim_{k\to 0} K_4 &= \frac{K_{40}}{k^2}\bigg\{\sqrt{2}\,y_0^{++}-y_1^{++}+\frac{k}{m}y_1^{+-}\bigg\}.
\end{aligned} \tag{A41}$$

Requiring that these seven invariants be regular at $k=0$ gives conditions on the four vertex functions. Near $k=0$, and independent of x_{10}, one requires

$$\begin{aligned}
&\lim_{k\to 0}(y_1^{++}-\sqrt{2}y_0^{++}) \to a_1k^2, \\
&\lim_{k\to 0} y_1^{+-} \to a_2k, \quad \lim_{k\to 0} y_0^{+-} \to a_3k.
\end{aligned} \tag{A42}$$

Note that these limits are satisfied by the usual behavior of the momentum space wave functions. Using the definitions [taken from (A34) multiplied by δ_{ρ_2}] gives

$$\begin{aligned}
y_1^{++}-\sqrt{2}y_0^{++} &= -\sqrt{\frac{3}{2}}w_v = -\sqrt{\frac{3}{2}}\delta_+ w, \\
y_0^{+-} &= -\frac{1}{\sqrt{2}}\delta_- v_s, \quad y_1^{+-} = -\frac{1}{\sqrt{2}}\delta_- v_t,
\end{aligned} \tag{A43}$$

which shows that the standard k^ℓ behavior of the P and D state wave functions will satisfy the necessary conditions.

APPENDIX B: NONRELATIVISTIC FORM FACTOR

While the formulas for nonrelativistic form factors in coordinate space are well known and widely used, I am unaware of similar results for the form factors in momentum space. As the CST gives the nonrelativistic limits in momentum space, I show here that the result obtained for G_C does indeed agree with the usual nonrelativistic limit. This is needed for the discussion in Sec. V C.

1. Wave functions in momentum space

To prepare for the discussion of the nonrelativistic form factor, I write the nonrelativistic wave functions in the form

$$Z_{\ell m}(\mathbf{r}) = \frac{i^\ell\, z_\ell(r)}{r}Y_{\ell m}(\hat{\mathbf{r}}), \quad Z_{\ell m}(\mathbf{k}) = z_\ell(k)Y_{\ell m}(\hat{\mathbf{k}}), \tag{B1}$$

where z_ℓ a generic name for the radial wave functions, $u(\ell=0)$ or $w(\ell=2)$, and $Y_{\ell m}$ is the spherical harmonic with relations

$$\begin{aligned}
&\int d\Omega_{\hat{\mathbf{r}}}\, Y_{\ell m}(\hat{\mathbf{r}})Y^*_{\ell' m'}(\hat{\mathbf{r}}) = \delta_{mm'}\delta_{\ell\ell'}, \\
&\frac{4\pi}{2\ell+1}\sum_{m=-\ell}^{\ell} Y_{\ell m}(\hat{\mathbf{r}})Y^*_{\ell m}(\hat{\mathbf{k}}) = P_\ell(\hat{\mathbf{k}}\cdot\hat{\mathbf{r}}), \\
&\frac{4\pi}{2\ell+1}\sum_{m=-\ell}^{\ell} Y_{\ell m}(\hat{\mathbf{r}})Y^*_{\ell m}(\hat{\mathbf{r}}) = 1.
\end{aligned} \tag{B2}$$

Following the usual conventions, the wave functions in coordinate space are *reduced* (divided by r), and I use the convention that the wave functions in coordinate and momentum spaces are distinguished only by their arguments (r for coordinate space and k for momentum space). For a discussion of the phase i^ℓ, see Eq. (3.36) and the last paragraph of Sec. III C in Ref. [15]. This phase, which comes from the familiar plane wave expansion, is need to keep the z_ℓ's real. The standard Fourier transform links the two spaces

$$\begin{aligned}
Z_{\ell m}(\mathbf{r}) &= \frac{1}{(2\pi)^{\frac{3}{2}}}\int d^3k\, \exp(i\mathbf{k}\cdot\mathbf{r})\, Z_{\ell m}(\mathbf{k}), \\
Z_{\ell m}(\mathbf{k}) &= \frac{1}{(2\pi)^{\frac{3}{2}}}\int d^3k\, \exp(-i\mathbf{k}\cdot\mathbf{r})\, Z_{\ell m}(\mathbf{r}).
\end{aligned} \tag{B3}$$

Using the familiar plane wave expansion

$$\begin{aligned}
\exp(i\mathbf{k}\cdot\mathbf{r}) &= \sum_{\ell=0}^{\infty}(2\ell+1)i^\ell j_\ell(kr)P_\ell(\hat{\mathbf{k}}\cdot\hat{\mathbf{r}}) \\
&= 4\pi\sum_{\ell=0}^{\infty} i^\ell j_\ell(kr)\sum_{m=-\ell}^{\ell} Y_{\ell m}(\hat{\mathbf{k}})Y^*_{\ell m}(\hat{\mathbf{r}}),
\end{aligned} \tag{B4}$$

where $j_\ell(kr)$ is the spherical Bessel function, I reduce the Eqs. (B3) to

$$\begin{aligned}
&\frac{1}{(2\pi)^{\frac{3}{2}}}\int d^3k\, \exp(i\mathbf{k}\cdot\mathbf{r})\, z_\ell(k)Y_{\ell m}(\hat{\mathbf{k}}) = Z_{\ell m}(\mathbf{r}) = \frac{i^\ell z_\ell(r)}{r}Y_{\ell m}(\hat{\mathbf{r}}) = i^\ell\sqrt{\frac{2}{\pi}}\int_0^\infty r^2\, dr\, j_\ell(kr)z_\ell(k)Y_{\ell m}(\hat{\mathbf{r}}), \\
&\frac{i^\ell}{(2\pi)^{\frac{3}{2}}}\int d^3r\, \exp(-i\mathbf{k}\cdot\mathbf{r})\frac{z_\ell(r)}{r}Y_{\ell m}(\hat{\mathbf{r}}) = Z_{\ell m}(\mathbf{r}) = z_\ell(k)Y_{\ell m}(\hat{\mathbf{k}}) = \sqrt{\frac{2}{\pi}}\int_0^\infty r^2\, dr\, j_\ell(kr)\frac{z_\ell(r)}{r}Y_{\ell m}(\hat{\mathbf{k}}).
\end{aligned} \tag{B5}$$

Dropping the common factors gives the relations [see Eq. (A32) of Ref. [2]]

$$\frac{z_\ell(r)}{r}=\sqrt{\frac{2}{\pi}}\int_0^\infty k^2dk\, j_\ell(kr)z_\ell(k),\qquad z_\ell(k)=\sqrt{\frac{2}{\pi}}\int_0^\infty r^2dr\, j_\ell(kr)\frac{z_\ell(r)}{r}. \tag{B6}$$

2. Derivation of the charge form factor in momentum space

The nonrelativistic charge form factor is

$$G_C^{\rm NR}=\int_0^\infty dr[u^2(r)+w^2(r)]j_0(\tau_0), \tag{B7}$$

where $\tau_0=\frac{1}{2}Qr$.

To transform each factor in Eq. (B7) to momentum space, begin by restoring the missing angular integrals:

$$\begin{aligned}
\int_0^\infty r^2dr\, j_0(\tau_0)\frac{z_\ell^2(r)}{r^2}&=\frac{1}{2\pi}\int_0^\infty r^2dr\int d\Omega_{\hat{\mathbf r}}\;\exp\left[\frac{i\mathbf{q}\cdot\mathbf{r}}{2}\right]\frac{z_\ell^2(r)}{r^2}=\frac{2}{2\ell+1}\int d^3r\;\exp\left[\frac{i\mathbf{q}\cdot\mathbf{r}}{2}\right]\frac{z_\ell^2(r)}{r^2}\sum_{m=-\ell}^{\ell}Y_{\ell m}(\hat{\mathbf r})Y_{\ell m}^*(\hat{\mathbf r})\\
&=\frac{2}{2\ell+1}\int d^3r\int d^3r'\;\delta(\mathbf{r}-\mathbf{r}')\;\exp\left[\frac{i\mathbf{q}\cdot\mathbf{r}}{2}\right]\frac{z_\ell(r)}{r}\frac{z_\ell(r')}{r'}\sum_{m=-\ell}^{\ell}Y_{\ell m}(\hat{\mathbf r})Y_{\ell m}^*(\hat{\mathbf r}')\\
&=\frac{2}{(2\ell{+}1)(2\pi)^3}\sum_{m=-\ell}^{\ell}\int d^3k\int d^3r\;\exp\left[i\left(\mathbf{k}{+}\frac{1}{2}\mathbf{q}\right)\cdot\mathbf{r}\right]\frac{z_\ell(r)}{r}Y_{\ell m}^*(\hat{\mathbf r})\int d^3r'\;\exp[-i\mathbf{k}\cdot\mathbf{r}']\frac{z_\ell(r')}{r'}Y_{\ell m}(\hat{\mathbf r}')\\
&=\frac{2}{(2\ell+1)(2\pi)^3}\sum_{m=-\ell}^{\ell}\int d^3k\int d^3k'\;\delta\left(\mathbf{k}'-\frac{1}{2}\mathbf{q}-\mathbf{k}\right)\int d^3r\;\exp[i\mathbf{k}'\cdot\mathbf{r}]\frac{z_\ell(r)}{r}Y_{\ell m}^*(\hat{\mathbf r})\\
&\quad\times\int d^3r'\;\exp[-i\mathbf{k}\cdot\mathbf{r}']\frac{z_\ell(r')}{r'}Y_{\ell m}(\hat{\mathbf r}')\\
&=\frac{2}{2\ell+1}\sum_{m=-\ell}^{\ell}\int d^3k\int d^3k'\;\delta\left(\mathbf{k}'-\frac{1}{2}\mathbf{q}-\mathbf{k}\right)z_\ell(k')Y_{\ell m}^*(\hat{\mathbf k}')z_\ell(k)Y_{\ell m}(\hat{\mathbf k})\\
&=\frac{2}{2\ell+1}\sum_{m=-\ell}^{\ell}\int d^3k\; z_\ell(k_{\frac12})z_\ell(k)Y_{\ell m}^*(\hat{\mathbf k}_{\frac12})Y_{\ell m}(\hat{\mathbf k})=\frac{1}{2\pi}\int d^3k P_\ell(\boldsymbol{k}_+\cdot\boldsymbol{k}_-)z_\ell(k_+)z_\ell(k_-),
\end{aligned} \tag{B8}$$

where $\mathbf{k}_{\frac12}=\mathbf{k}+\frac{1}{2}\mathbf{q}$ and $\mathbf{k}_\pm$ was already defined in Eq. (4.2). This final result was already given in Eq. (4.1).

APPENDIX C: EXTRACTION OF F_3 AND F_4 FROM DATA FOR G_M AND T_{20}

Here I present details of how the unknown off-shell form factors F_3 and F_4 are determined from a simultaneous fit to the Sick GA "data" for G_M and T_{20}. To this end, recall the expansion (1.19). Dropping explicit mention of the Q^2 arguments, this expansion is rewritten in a form that isolates the F_3 and F_4 contributions

$$G_X=G_{X,0}+\sum_{i=3}^{4}F_iD_{X,i}, \tag{C1}$$

where G_X is the value of form factor at each Sick GA point $G_X=G_X(Q_i^2)$. A similar expansion for the parameter y of Eq. (1.25) that fixes T_{20} can be written

$$3yG_C=2\eta\, G_Q\to\sum_{i=3}^{4}F_ia_i=a_0, \tag{C2}$$

where

$$\begin{aligned}
a_i&=3yD_{C,i}-2\eta\, D_{Q,i}\quad i=\{3,4\},\\
a_0&=2\eta\, G_{Q,0}-3yG_{C,0}.
\end{aligned} \tag{C3}$$

Solving Eqs. (C1) (with $X\to M$) and (C2) (for $i=\{3,4\}$ and $j=\{4,3\}\neq i$) gives

$$F_i=\frac{1}{D_{ij}}[a_0D_{M,j}+a_j(G_{M,0}-G_M)], \tag{C4}$$

where

$$D_{ij}=a_iD_{M,j}-a_jD_{M,i}=-D_{ji}. \tag{C5}$$

Note that when $y\to\pm\infty$, F_i becomes

$$F_i\to\frac{G_{C,0}D_{M,j}+D_{C,j}(G_M-G_{M,0})}{D_{M,i}D_{C,j}-D_{C,i}D_{M,j}}, \tag{C6}$$

independent of the sign of y, ensuring that the F_i are continuous at the point where $T_{20}=-1/\sqrt{2}$.

Assuming there are no errors other than the error δG_M in G_M and δy in the y parameter, the errors in F_3 and F_4 can be obtained by expanding Eqs. (C1) and (C2) to first order, giving

$$\begin{aligned}\sum_{i=3}^{4}\delta F_i\,D_{M,i} &= \delta G_M,\\ \sum_{i=3}^{4}\delta F_i\,a_i &= -3\delta y(G_{C,0}+F_3D_{C,3}+F_4D_{C,4})\\ &\equiv -3\delta y\,b_0,\end{aligned}\tag{C7}$$

with the solution

$$\begin{aligned}\delta F_i &= -\frac{1}{D_{ij}}(a_j\delta G_M+3\delta yD_{M,j}b_0)\\ &\to \left|\frac{1}{D_{ij}}\right|(|a_j\delta G_M|+|3\delta yK_{jM}b_0|],\end{aligned}\tag{C8}$$

where the second expression ensures that each error is treated as a positive contribution.

APPENDIX D: EXTRACTION OF G_{En} FROM DATA FOR A

While it is straightforward to extract the predicted values of G_{En} from the data for A, it is still useful to outline here the way in which this was done. I begin by isolating the G_{En} contribution from the expansion (1.19). Dropping the Q^2 arguments, the new expansion is

$$G_X = G_ED_{X,E}+G_MD_{X,M}+\sum_{i=3}^{4}F_iD_{X,i}\equiv G_EJ_{1X}+J_{0X},\tag{D1}$$

where $J_{1X}=D_{X,E}$, J_{0X} is defined by the expression, and, as before, all nucleon form factors contributing to the deuteron are *isoscalar*, so that here $G_E=G_{Es}=G_{Ep}+G_{En}$. (In this section, G_M denotes the *nucleon* magnetic form factor, and not the deuteron.) The first two on-shell nucleon form factors, F_1 and F_2 are related to the nucleon electric and magnetic form factors in the usual way

$$\begin{aligned}G_E(Q^2)&=F_1(Q^2)-\tau F_2(Q^2),\\ G_M(Q^2)&=F_1(Q^2)+F_2(Q^2),\end{aligned}\tag{D2}$$

where $\tau=Q^2/(4m^2)$. Hence,

$$\begin{aligned}D_{X,1}(Q^2)&=D_{X,E}(Q^2)+D_{X,M}(Q^2),\\ D_{X,2}(Q^2)&=D_{X,M}(Q^2)-\tau D_{X,E}(Q^2),\end{aligned}\tag{D3}$$

or, in terms of the calculated body form factors,

$$D_{X,E}=\frac{D_{X,1}-D_{X,2}}{1+\tau},\qquad D_{X,M}=\frac{\tau D_{X,1}+D_{X,2}}{1+\tau}.\tag{D4}$$

This defines all of the coefficients in the expansion (D1).

The quadratic dependence of A on G_E can now be expressed in a compact form

$$A=G_E^2C_2+G_EC_1+C_0.\tag{D5}$$

The coefficients C_i (all functions of Q^2) are

$$\begin{aligned}C_2&=J_{1C}^2+\tfrac{8}{9}\eta^2J_{1Q}^2+\tfrac{2}{3}\eta J_{1M}^2,\\ C_1&=2J_{1C}J_{0C}+\tfrac{16}{9}\eta^2J_{1Q}J_{0Q}+\tfrac{4}{3}\eta J_{1M}J_{0M},\\ C_0&=J_{0C}^2+\tfrac{8}{9}\eta^2J_{0Q}^2+\tfrac{2}{3}\eta J_{0M}^2.\end{aligned}\tag{D6}$$

The solution to (D5) is

$$G_E=\frac{1}{2C_2}\big(\sqrt{4C_2(A-C_0)+C_1^2}-C_1\big),\tag{D7}$$

where the sign of the square root was chosen to give a positive G_E when $G_M\to 0$.

The error in G_E comes from both the error in A and the errors in F_3 and F_4. Since F_3 and F_4 contribute only to J_{0X}, its contribution to the error is contained in the factors

$$\delta J_{0X}=\sum_{i=3}^{4}\delta F_iD_{X,i},\tag{D8}$$

which contribute the following errors to the C_i

$$\begin{aligned}\delta C_0&=2\big[J_{0C}\delta J_{0C}+\tfrac{8}{9}\eta^2J_{0Q}\delta J_{0Q}+\tfrac{2}{3}\eta J_{0M}\delta J_{0M}\big],\\ \delta C_1&=2\big[J_{1C}\delta J_{0C}+\tfrac{8}{9}\eta^2J_{1Q}\delta J_{0Q}+\tfrac{2}{3}\eta J_{1M}\delta J_{0M}\big],\end{aligned}\tag{D9}$$

combining these errors with the experimental error in A gives the following estimate for the error in G_E:

$$\delta G_E=\frac{\delta A-\delta C_0-\delta C_1G_E}{\sqrt{4C_2(A-C_0)+C_1^2}}.\tag{D10}$$

With these results in hand, I find the solution for G_{En} from the solution for G_E by subtracting G_{Ep}, which is also assumed to have no error. Hence, $\delta G_{En}=\delta G_E$ as given in (D10).

APPENDIX E: REDEFINITIONS OF THE $\mathcal{C}$ TRACES

In Refs. II and III, the arguments for the $\mathcal{B}$ and $\mathcal{C}$ traces were chosen differently. This is inconvenient for the numerical calculations performed in this paper and can be easily avoided by some redefinitions. In the case when the outgoing particle 1 is on shell, momenta used for the $\mathcal{B}$ were

$$\begin{aligned}&\tilde k_+^B=\big\{E_+,\mathbf{k}+\tfrac{1}{2}\mathbf{q}\big\},\quad \tilde k_-^B=\big\{E_+,\mathbf{k}-\tfrac{1}{2}\mathbf{q}\big\},\\ &\tilde p_-^B=\{D_0-E_+,-\mathbf{k}\},\end{aligned}\tag{E1}$$

while for the $\mathcal{C}$ traces I previously used

$$\begin{aligned}&k_+^C=\{E_k,\mathbf{k}_C\},\quad k_-^C=\{E_k,\mathbf{k}_C-\mathbf{q}\},\\ &p_+^B=\big\{D_0-E_k,-\mathbf{k}_C+\tfrac{1}{2}\mathbf{q}\big\},\end{aligned}\tag{E2}$$

where here, to avoid confusion, I labeled the **k** momenta used for the $\mathcal{C}$ diagrams by $\mathbf{k}_C$ and therefore in these expressions $E_k\equiv E_{k_C}$.

The $\mathcal{C}$ momenta can be transformed into the $\mathcal{B}$ momenta by the simple transformation

$$\mathbf{k}_C\to\mathbf{k}+\tfrac{1}{2}\mathbf{q}.\tag{E3}$$

In this Appendix, I show the effect of this transformation on the formulas for the $\mathcal{C}$ traces published in Ref. II.

First, consider the argument shifts for the $\mathcal{C}$ traces. In Ref. [2], the arguments of the K_i are shifted to

$$\begin{aligned}\hat R_-^2 &= \frac{1}{m_d^2}\left[D_0E_k+\frac{1}{2}(k_{Cz}-Q)\,Q\right]^2-(m^2+2k_{Cz}Q-Q^2)\\ &\to \frac{1}{m_d^2}\left[D_0E_++\frac{1}{2}\left(k_z-\frac{1}{2}Q\right)Q\right]^2-(m^2+2k_zQ),\end{aligned}$$

$$\begin{aligned}\hat{R}_0^- &= \frac{1}{2m_d}[2D_0E_k + (k_{Cz} - Q)\,Q] \\ &\to \frac{1}{2m_d}\left[2D_0E_+ + \left(k_z - \frac{1}{2}Q\right)Q\right],\end{aligned} \tag{E4}$$

while the argument of the outgoing generic on-shell Z_+ is

$$\begin{aligned}R_+^2 &= \frac{1}{m_d^2}\left[D_0E_k - \frac{1}{2}k_{Cz}Q\right]^2 - m^2 \\ &\to \frac{1}{m_d^2}\left[D_0E_+ - \frac{1}{2}\left(k_z + \frac{1}{2}Q\right)Q\right]^2 - m^2.\end{aligned} \tag{E5}$$

If the outgoing state in the $\mathcal{B}$ traces has particle 1 on shell, so that $k_0 = E_+$, these expressions are identical to the argument shifts given in Eq. (A19), showing that the transformation (E3) transforms the shifts for $\mathcal{C}$ into those for $\mathcal{B}$.

The expressions for the $\mathcal{C}$ traces depend on the coefficients defined in Table IX of Ref. [2] (some of which are defined in Tables VI and VII of that reference). The only coefficients that depend on $\mathbf{k}$ are the a's, with transformations summarized in Table XV, and the coefficients c_0', c_q, and the particle 1 momentum squared, p_+^2, all of which transform to

$$\begin{aligned}c_0' &= D_0E_k \to D_0E_+, \\ c_q &= -Qk_{Cz} \to -Q\left(k_z + \frac{1}{2}Q\right), \\ p_+^2 &= (P_+ - k)^2 = m_d^2 + m^2 - 2D_0E_k + Qk_{Cz} \\ &\to m_d^2 + m^2 - 2D_0E_+ + Q\left(k_z + \frac{1}{2}Q\right).\end{aligned} \tag{E6}$$

Finally, the volume integral transforms to

$$\int_k \equiv \int \frac{d^3k_C}{(2\pi)^3}\frac{m}{E_k} \to \int \frac{d^3k}{(2\pi)^3}\frac{m}{E_+} = \int_k \frac{E_k}{E_+}, \tag{E7}$$

where in the final expression, I return to the definition $E_k = \sqrt{m^2 + \mathbf{k}^2}$ used everywhere.

With these substitutions, the same four-vector $k_+ = \{E_+, \mathbf{k} + \frac{1}{2}\mathbf{q}\}$ is used for both the $\mathcal{C}$ and $\mathcal{B}_+$ traces.

APPENDIX F: CORRECTED TREATMENT OF THE ANGULAR INTEGRALS WHEN $x_{10} \neq 1$

Evaluation of the angular integrals was discussed in detail in Appendix B of Ref. [15], but the discussion there is not accurate for cases when $x_{10} \neq 1$. In that paper, we introduced the variable x_0 to scale for the off-shell energy dependence to the *relative* energy, where

$$p_0 = x_0\left(E_p - \tfrac{1}{2}W\right) \tag{F1}$$

(cf. Eq. (A16) of Ref. [15]). However, since the relative energy p_0 can be large when $p \to 0$, the quantity x_0 defined in this way can also become quite large, making numerical calculations using this quantity difficult to carry out accurately. In this paper, I have chosen to scale the off-shell energy of particle 1, using the relation

$$p_{10} = x_{10}E_p, \quad p_{20} = W - x_{10}E_p. \tag{F2}$$

It follows immediately that the relative energy expressed in terms of x_{10} is

$$p_0 = \tfrac{1}{2}(p_{10} - p_{20}) = x_{10}E_p - \tfrac{1}{2}W \tag{F3}$$

so that

$$x_0 = \frac{2x_{10}E_p - W}{2E_p - W}. \tag{F4}$$

This correspondence can be used quite successfully in many places, but for the discussion of the angular integrals it is best to work directly with x_{10}.

As an example, consider how the treatment of the direct terms must be modified when the *both* nucleons are off shell. Now the the momentum transfer depends on x_{10}

$$\begin{aligned}q^2(x_{10}) &= (x_{10}E_p - E_{p'})^2 - p^2 - p'^2 + 2pp'z \\ &= 2pp'(z_0 - z),\end{aligned} \tag{F5}$$

where I assume that the initial state (with momentum p') has particle 1 on shell. This momentum transfer is zero at the critical cosine

$$z_0 = \frac{p^2 + p'^2 - (x_{10}E_p - E_{p'})^2}{2pp'}. \tag{F6}$$

The angular integrals are strongly peaked at $z = z_0$. When $x_{10} = 1$, $z_0 \geqslant 1$ and approaches 1 only when $p \to p'$. This singularity can be handled by the methods used in Ref. [15]. However, for $x_{10} \neq 1$, z_0 can be less than 1 and the angular integrals can peak inside of the region of integration. This requires a mapping of the type used for the exchange terms, described in Appendix B3, Eq. (B9) of Ref. [15].

TABLE XV. These vector products used in the definitions of the $\mathcal{C}_{n,i}$ traces, originally defined in Table VI in Ref. [2], are redefined as a consequence of the transformation (E3).

a's	$n = 1\ (J^0_{00})$	$n = 2\ (J^0_{+-})$	$n = 3_+\ (J^+_{+0})$	$n = 3_-\ (J^-_{0-})$
a_+	$(E_kQ - 2k_{Cz}D_0)/(2m_d)$ $\to (E_+Q - (2k_z + Q)D_0)/(2m_d)$	$\frac{1}{\sqrt{2}}(k_x - ik_y)$	$\frac{1}{\sqrt{2}}(k_x - ik_y)$	$(E_kQ - 2k_{Cz}D_0)/(2m_d)$ $\to (E_+Q - (2k_z + Q)D_0)/(2m_d)$
a_-	$-(E_kQ + 2k_{Cz}D_0)/(2m_d)$ $\to -(E_+Q + (2k_z + Q)D_0)/(2m_d)$	$\frac{1}{\sqrt{2}}(k_x + ik_y)$	$-(E_kQ + 2k_{Cz}D_0)/(2m_d)$ $\to -(E_+Q + (2k_z + Q)D_0)/(2m_d)$	$\frac{1}{\sqrt{2}}(k_x + ik_y)$
a_0	$E_k \to E_+$	$E_k \to E_+$	$\frac{1}{\sqrt{2}}(k_x + ik_y)$	$-\frac{1}{\sqrt{2}}(k_x - ik_y)$

APPENDIX G: ERRATA IN REF. II

There are errors in the magnetic moment results reported in Ref. II [4]. As I did in Ref. II, here I present the difference between the expansion of the relativistic calculation and $\mu_s = 0.880 = 1+\kappa_s$ to obtain the "corrections" to the magnetic moment coming from the relativistic calculation. Multiplying the normalization condition by 0.880, written in the form (approximating $E_k - M_d \to -m$ and $M_d \to 2m$ in the $a(p^2)$ terms)

$$\begin{aligned}0.880 = (1+\kappa_s)\int_0^\infty k^2dk\big\{&u^2+w^2+v_t^2+v_s^2+4a(p^2)m\big[\delta_k(u^2+w^2)-2m(v_t^2+v_s^2)\big]\\&-u[\delta_+\hat u]_{k_0}-w[\delta_+\hat w]_{k_0}+v_t[\delta_-\hat v_t]_{k_0}+v_s[\delta_-\hat v_s]_{k_0}-uu^{(2)}-ww^{(2)}-v_tv_t^{(2)}-v_sv_s^{(2)}\big\}.\end{aligned}\tag{G1}$$

and subtracting this from the predictions of the (A) + (A$^{(2)}$) + (B) diagrams (multiplied by 1/2) gives the following corrections to the magnetic moment:

$$\Delta\mu_d = \sum_{X=A,B}\int_0^\infty k^2dk\frac{1}{2}\big\{\delta\mu^X_{\rm NR}+\delta\mu^X_{R_c}+\delta\mu^X_{h'}+\delta\mu^A_{V_2}+\delta\mu^B_{V_1}+\delta\mu^A_{\rm int}+\delta\mu^X_{P}\big\},\tag{G2}$$

where the expression reflects the fact that the only nonzero contributions to $\delta\mu_{V_1}(\delta\mu_{V_2})$ come from the (B) [(A)$^{(2)}$)] diagrams and $\delta\mu^B_{\rm int}$, while not zero, is of lower order and can be dropped. The nonzero contributions are therefore

$$\begin{aligned}\delta\mu^A_{\rm NR}&=\delta\mu^B_{\rm NR}=-\frac{3}{4}(1+2\kappa_s)w^2,\\ \delta\mu^A_{R_c}&=-\left[\frac{E_k-m}{6E_k}\right][2(1+\kappa_s)u^2+\sqrt{2}(1-2\kappa_s)uw-(2-\kappa_s)w^2],\\ \delta\mu^B_{R_c}&=-\kappa_s\left[\frac{E_k-m}{6E_k}\right](2u^2+w^2-2\sqrt{2}uw),\\ \delta\mu^A_{h'}&=-a(p^2)m\big\{(1+2\kappa_s)\big(3\delta_kw^2-4m\,v_s^2\big)-4\kappa_smv_t^2+6\sqrt{2}m\,v_tv_s\big\},\\ \delta\mu^B_{h'}&=-a(p^2)m\big\{(1+2\kappa_s)\big[3\delta_kw^2-2m\big(v_t^2+2v_s^2\big)\big]-8m\sqrt{2}(1+\kappa_s)v_tv_s\big\},\\ \delta\mu^A_{V_2}&=\frac{3}{2}(1+2\kappa_s)ww^{(2)}+\frac{1}{2}(5+6\kappa_s)v_tv_t^{(2)}+(3+2\kappa_s)v_sv_s^{(2)}+\sqrt{2}\kappa_s\big(v_tv_s^{(2)}+v_sv_t^{(2)}\big)\\ &\quad-\frac{m}{\sqrt{6}}\bigg\{u^{(2)}(v_t'-\sqrt{2}v_s')+w^{(2)}(\sqrt{2}v_t'+v_s')-v_t^{(2)}(u'+\sqrt{2}w')+v_s^{(2)}(\sqrt{2}u'-w')\\ &\quad+\frac{1}{k}\big[2u^{(2)}(v_t-\sqrt{2}v_s)-w^{(2)}(\sqrt{2}v_t+v_s)-3w\big(\sqrt{2}v_t^{(2)}+v_s^{(2)}\big)\big]\bigg\},\\ \delta\mu^B_{V_1}&=(1+\kappa_s)\big[3w[\delta_+w]_{k_0}-v_t[\delta_-v_t]_{k_0}-2v_s[\delta_-v_s]_{k_0}-\sqrt{2}(v_t[\delta_-v_s]_{k_0}+v_s[\delta_-v_t]_{k_0})\big],\\ \delta\mu^A_{\rm int}&=-\frac{m}{\sqrt{6}}\Big[u'(v_t-\sqrt{2}v_s)+w'(\sqrt{2}v_t+v_s)+\frac{3}{k}w(\sqrt{2}v_t+v_s)\Big],\\ \delta\mu^A_P&=-\frac{1}{4}(5+6\kappa_s)v_t^2-\frac{1}{2}(3+2\kappa_s)v_s^2-\sqrt{2}\kappa_sv_tv_s,\\ \delta\mu^B_P&=\frac{1}{4}\big[-(3+2\kappa_s)\big(v_t^2+2v_s^2\big)+2\sqrt{2}(1-2\kappa_s)v_tv_s\big].\end{aligned}\tag{G3}$$

Combining these terms allows us to compare then with Eq. (5.6) of Ref. II. The sums (divided by 2) are

$$\begin{aligned}\mu_{R_c}&=\int_0^\infty k^2dk\left[\frac{E_k-m}{E_k}\right]\left\{-\frac{1}{3}\mu_s\left(u^2-\sqrt{2}uw+\frac{1}{2}w^2\right)+\frac{1}{6}u^2-\frac{5}{6\sqrt{2}}uw+\frac{1}{3}w^2\right\},\\ \mu_{h'}&=\int_0^\infty k^2dk\,a(p^2)m\left\{2\mu_s\big[-3\delta_kw^2+2m\big(v_t^2+\sqrt{2}v_tv_s+2v_s^2\big)\big]+3\delta_kw^2-3m\left(v_t^2+\sqrt{2}v_tv_s+\frac{4}{3}v_s^2\right)\right\},\\ \mu_{V_2}&=\int_0^\infty\frac{k^2dk}{2}\left\{(2\mu_s-1)\frac{3}{2}ww^{(2)}+\mu_s\big(3v_tv_t^{(2)}+2v_sv_s^{(2)}\big)+(\mu_s-1)\sqrt{2}\big(v_tv_s^{(2)}+v_sv_t^{(2)}\big)-\frac{1}{2}v_tv_t^{(2)}+v_sv_s^{(2)}-m'^{(2)}\right\},\\ \mu_{V_1}&=\int_0^\infty k^2dk\;\mu_s\left\{\frac{3}{2}w[\delta_+w]_{k_0}-\frac{1}{2}v_t[\delta_-v_t]_{k_0}-v_s[\delta_-v_s]_{k_0}-\frac{1}{\sqrt{2}}(v_t[\delta_-v_s]_{k_0}+v_s[\delta_-v_t]_{k_0})\right\},\end{aligned}$$

$$\mu_{\rm int} = -\frac{m}{2\sqrt{6}}\int_0^\infty k^2dk\left\{u'(v_t-\sqrt{2}v_s) - w(\sqrt{2}v_t+v_s)' + \frac{1}{k}w(\sqrt{2}v_t+v_s)\right\},$$
$$\mu_P = \int_0^\infty k^2dk\left\{-\mu_s\left(\frac{9}{8}v_t^2+\sqrt{2}v_tv_s+\frac{5}{4}v_s^2\right)+\frac{1}{4}v_t(v_t+5\sqrt{2}v_s)\right\}. \tag{G4}$$

Note that $\mu_{\rm NR}$, μ_{V_2}, and $\mu_{\rm int}$ agree with Ref. II, but the others do not. The μ_χ terms have been found to be negligible and were not recalculated.

In the process of computing the form factors, the following errata were discovered in the equations reported in Ref. II:

(1) Eq. (C3) should read $\widetilde{Z}_\pm = \widetilde{Z} - (E_k - k_0)\widetilde{Z}_{k_0}$.
(2) In Eq. (B1),
    (i) the coefficient of the D_+D_- term should be divided by an additional factor of 2 and
    (ii) the coefficient of the C_+C_- term should be divided by an additional factor of $2m^2$.
(3) In Eq. (B2),
    (i) in the coefficient of C_+A_-, the term $-2b_0a_+b_+$ should be replaced by $-2b_0a_-b_+$,
    (ii) a closing parenthesis,), is missing from the coefficient of the C_+D_- term; it belongs just before $-z_+$, so that the coefficient of b_0 includes the b_+ and a_+ terms but not the z_+ term,
    (iii) a similar closing parenthesis,), is missing from the coefficient of the D_+C_- term; it belongs just before $-z_-$,
    (iv) in the coefficient of C_+C_-, the coefficient of $(4m^2+m_d^2)$ is $(b_+z_-+b_-z_+)$, and not $(b_+z_-+b_-c_+)$.
(4) In Eq. (B.7),
    (i) the HI terms are divided by m^4 (*not* m^2) and
    (ii) in the coefficient of the $\widetilde{F}_+\widetilde{F}_-$ term replace $(2X_4 - X_5)$ by $(X_4 - X_5)$ and in the coefficient of the $\widetilde{H}_+\widetilde{H}_-$ term replace X_1X_5 by $X_1(X_5+X_4)$.
(5) In Eq. (B10),
    (i) the GK_2 terms should be divided by m^2 and
    (ii) divide the entire trace by an extra factor of $2m$ (so the coefficient in front is $\zeta_B/(4m^2)$, *not* $\zeta_B/(2m)$.

These errors arose when the original MATHEMATICA formulas were transcribed into text. Fortunately, the results of Refs. II and III were derived directly from the correct MATHEMATICA formula and are therefore unaffected by these errors.

[1] F. Gross, Phys. Rev. C **89**, 064001 (2014), referred to as Ref. I.
[2] F. Gross, Phys. Rev. C **89**, 064002 (2014), referred to as Ref. II. See also Erratum in Ref. [4].
[3] F. Gross, Phys. Rev. C **91**, 014005 (2015), referred to as Ref. III.
[4] F. Gross, Phys. Rev. C **101**, 029901 (2020).
[5] F. Gross, Phys. Rev. **186**, 1448 (1969).
[6] F. Gross, Phys. Rev. D **10**, 223 (1974).
[7] F. Gross, Phys. Rev. C **26**, 2203 (1982).
[8] J. W. Van Orden, N. Devine, and F. Gross, Phys. Rev. Lett. **75**, 4369 (1995).
[9] F. Gross, J. W. Van Orden, and K. Holinde, Phys. Rev. C **45**, 2094 (1992).
[10] M. Garcon and J. W. Van Orden, Adv. Nucl. Phys. **26**, 293 (2001).
[11] R. A. Gilman and F. Gross, J. Phys. G **28**, R37 (2002).
[12] L. E. Marcucci, F. Gross, T. M. Pena, M. Piarulli, R. Schiavilla, I. Sick, A. Stadler, J. W. Van Orden, and M. Viviani, J. Phys. G **43**, 023002 (2016).
[13] M. T. Pena, F. Gross, and Y. Surya, Phys. Rev. C **54**, 2235 (1996).
[14] F. Gross and A. Stadler, Phys. Rev. C **78**, 014005 (2008).
[15] F. Gross and A. Stadler, Phys. Rev. C **82**, 034004 (2010).
[16] A. Stadler and F. Gross, Phys. Rev. Lett. **78**, 26 (1997).
[17] F. Gross and D. O. Riska, Phys. Rev. C **36**, 1928 (1987).
[18] I. Sick, Prog. Part. Nucl. Phys. **47**, 245 (2001), and private communication.
[19] E. L. Lomon, Phys. Rev. C **66**, 045501 (2002).
[20] F. Cardarelli, I. L. Grach, I. Narodetsky, G. Salme, and S. Simula, Phys. Lett. B **359**, 1 (1995).
[21] C. D. Buchanan and M. R. Yearian, Phys. Rev. Lett. **15**, 303 (1965).
[22] G. G. Simon, C. Schmitt, and V. H. Walther, Nucl. Phys. A **364**, 285 (1981).
[23] S. Auffret *et al.*, Phys. Rev. Lett. **54**, 649 (1985).
[24] R. Cramer *et al.*, Z. Phys. C **29**, 513 (1985).
[25] R. G. Arnold *et al.*, Phys. Rev. Lett. **58**, 1723 (1987).
[26] P. E. Bosted *et al.*, Phys. Rev. C **42**, 38 (1990).
[27] R. Suleiman, Measurements of the electric and magnetic elastic structure functions of the deuteron at large momentum transfers, Ph.D. thesis, Kent State University, OH, 1999, https://www.kent.edu/sites/default/files/file/RSuleiman.pdf.
[28] G. G. Petratos, Nucl. Phys. A **663**, 357c (2000).
[29] M. E. Schulze *et al.*, Phys. Rev. Lett. **52**, 597 (1984).
[30] V. F. Dmitriev *et al.*, Phys. Lett. B **157**, 143 (1985).
[31] B. B. Wojtsekhowski *et al.*, JETP Lett. **43**, 733 (1986).
[32] R. A. Gilman *et al.*, Phys. Rev. Lett. **65**, 1733 (1990).
[33] B. Boden *et al.*, Z. Phys. C **49**, 175 (1991).
[34] I. The *et al.*, Phys. Rev. Lett. **67**, 173 (1991).
[35] M. Garcon *et al.*, Phys. Rev. C **49**, 2516 (1994).
[36] M. Ferro-Luzzi *et al.*, Phys. Rev. Lett. **77**, 2630 (1996).
[37] M. Bouwhuis *et al.*, Phys. Rev. Lett. **82**, 3755 (1999).
[38] D. Abbott *et al.* (JLAB t(20) Collaboration), Phys. Rev. Lett. **84**, 5053 (2000).
[39] D. M. Nikolenko *et al.*, Nucl. Phys. A **684**, 525 (2001).
[40] C. Zhang *et al.*, Phys. Rev. Lett. **107**, 252501 (2011).
[41] D. Benaksas, D. Drickey, and D. Frerejacque, Phys. Rev. **148**, 1327 (1966).

[42] J. E. Elias, J. I. Friedman, G. C. Hartmann, H. W. Kendall, P. N. Kirk, M. R. Sogard, L. P. Van Speybroeck, and J. K. De Pagter, Phys. Rev. **177**, 2075 (1969).

[43] S. Galster, H. Klein, J. Moritz, K. H. Schmidt, D. Wegener, and J. Bleckwenn, Nucl. Phys. B **32**, 221 (1971).

[44] R. G. Arnold *et al.*, Phys. Rev. Lett. **35**, 776 (1975).

[45] S. Platchkov *et al.*, Nucl. Phys. A **510**, 740 (1990).

[46] L. C. Alexa *et al.* (Jefferson Laboratory Hall A Collaboration), Phys. Rev. Lett. **82**, 1374 (1999).

[47] D. Abbott *et al.* (Jefferson Laboratory t(20) Collaboration), Phys. Rev. Lett. **82**, 1379 (1999).

[48] T. Eden *et al.*, Phys. Rev. C **50**, R1749 (1994).

[49] C. Herberg *et al.*, Eur. Phys. J. A **5**, 131 (1999).

[50] M. Ostrick *et al.*, Phys. Rev. Lett. **83**, 276 (1999).

[51] D. I. Glazier *et al.*, Eur. Phys. J. A **24**, 101 (2005).

[52] R. Madey *et al.* (E93-038 Collaboration), Phys. Rev. Lett. **91**, 122002 (2003).

[53] B. Plaster *et al.* (Jefferson Laboratory E93-038 Collaboration), Phys. Rev. C **73**, 025205 (2006).

[54] I. Passchier *et al.*, Phys. Rev. Lett. **82**, 4988 (1999).

[55] H. Zhu *et al.* (E93026 Collaboration), Phys. Rev. Lett. **87**, 081801 (2001).

[56] G. Warren *et al.* (Jefferson Laboratory E93-026 Collaboration), Phys. Rev. Lett. **92**, 042301 (2004).

[57] C. F. Perdrisat, V. Punjabi, and M. Vanderhaeghen, Prog. Part. Nucl. Phys. **59**, 694 (2007).

[58] F. Gross, Phys. Rev. C **26**, 2226 (1982).

[59] A. Stadler and F. Gross, AIP Conf. Proc. **334**, 867 (1995).

[60] A. Stadler, F. Gross, and M. Frank, Phys. Rev. C **56**, 2396 (1997).

[61] S. A. Pinto, A. Stadler, and F. Gross, Phys. Rev. C **79**, 054006 (2009).

[62] S. A. Pinto, A. Stadler, and F. Gross, Phys. Rev. C **81**, 014007 (2010).

[63] B. M. Casper and F. Gross, Phys. Rev. **155**, 1607 (1967).

[64] I. Sick and D. Trautmann, Nucl. Phys. A **637**, 559 (1998).

[65] J. Adam Jr., F. Gross, S. Jeschonnek, P. Ulmer, and J. W. Van Orden, Phys. Rev. C **66**, 044003 (2002).